Modeling the transition to turbulence in plane Couette flow

Maher Lagha

École Polytechnique
Laboratoire d'Hydrodynamique

Thèse présentée pour obtenir le grade de

DOCTEUR DE L'ÉCOLE POLYTECHNIQUE

Spécialité : Mécanique

par

Maher LAGHA

Modeling the transition to turbulence in plane Couette flow

soutenue le 8 décembre 2006 devant le jury composé de :

M.	Patrice LE GAL	Examinateur	IRPHE, Marseille
M.	Dwight BARKLEY	Rapporteur	Warwick University, Grande-Bretagne
M.	François DAVIAUD	Examinateur	SPEC-CEA, Saclay
M.	Bruno ECKHARDT	Rapporteur	Philipps-Universitat, Marburg, Allemagne
M.	Paul MANNEVEILLE	Directeur de thèse	LadHyX, Ecole Polytechnique
M.	Peter SCHMIDT	Examinateur	LadHyX, Ecole Polytechnique

Foreword

The transition to turbulence in shear flows still leaves open several problems of great practical importance. This thesis is the continuation of the work of the Saclay group in this field. Their main focus was the investigation of the growth of a finite amplitude perturbation introduced in the laminar plane Couette flow (pCf), a shear flow between two parallel plates. When the control parameter exceeds a certain threshold, this perturbation is self-sustained and gives rise to a turbulent region, called a spot. Their study raised many questions and in this thesis we focus on few of them: How do this turbulent region sustains itself? What is the mechanism that spreads this turbulent region into laminar domain? The turbulent domain looks separated from the laminar domain by a sharp boundary, but is the flow outside this spot laminar? Once all the domain has become turbulent, how is the distribution of the durations needed to relax towards laminar state when the control parameter is decreased below the threshold?

To bring some elements of answer to these questions, we have derived a model of pCf in terms of partial differential equations (PDEs) using the Galerkin method. In this derivation, we used an assumption based on the experimental observation of the Saclay group, which is the coherence of the observed structures between the two plates, which permits us to consider few cross-stream modes. This simplification makes the identification of involved physical mechanisms easier than using simulations of the full dynamic equations. This kind of model allow us to approach the problem of spot propagation that requires explicit space dependence (spatiotemporal chaos), by contrast with models in terms of ordinary differential equations, obtained by frozen this spatial dependence (temporal chaos).

The outline of the manuscript is as follows. In chapter I, we review some experiments and results from the literature related to the questions under scrutiny: The first part of this chapter concerns the recent studies of the distributions of the transient lifetimes. The second part is dedicated to the spot spreading mechanisms and more generally to the coexistence between turbulent/laminar state. The last part concerns the self-sustainment of the turbulent state.

Then, in chapter II, the derivation of the model is detailed. The numerical method and some results are presented in chapter III. We show that this model reproduces the globally sub-criticality of pCf and that the global stability

threshold (R_g) using this model is found to be a factor 2 less than the one in the experiences. The extensivity of the turbulent state is also addressed. Then, the study of the distributions of the transient lifetimes shows the same behavior as in the experiments of the Saclay group: exponential decay of the duration of the transients and a divergence of the mean value of these duration in $1/(R_g - R)$, where R is the Reynolds number.

In chapter IV, we are interested by the self-sustainment of the turbulence inside a growing turbulent spot as well as in a fully turbulent domain. A brief survey of the work in the literature shows that the key question is about the generation of streamwise vortices. After analyzing the different terms in the streamwise vorticity equation, we find that the tilting term of the wall-normal vorticity into streamwise direction is the dominant term, in accordance with the other studies. However the tilting term of spanwise vorticity into streamwise direction is not negligible. By analyzing each term contributing to the generation of streamwise vorticity in physical space and tracking the evolution of this vorticity into streamwise vortices in time, we discovered a simple process for streamwise vortices generation where the flow field (U_0, W_0) related to the streaks (represented by the velocity component U_0 in our model and where $\partial_x U_0 + \partial_z W_0 = 0$) plays a crucial role. This process can be summarized as follows: a spanwise vortex is deformed by this flow and gives a crescent vortex where its legs are two counter-rotating vortices. They regenerate the streaks by the lift-up effect. We find that the streamwise vortices are generated in regions where a positive streak encounters a negative streak and results in a stagnation-like point, i.e., where $\partial_x U_0 \leq 0$ and $U_0 \approx 0$. Then, we derive a 1D-model in terms of four PDEs, showing the generation of streamwise vortices from spanwise vortices. The last part of this chapter is concerned with the generation of spanwise vortices. Under the action of the flow field (U_0, W_0), a localized region of streamwise velocity correction, represented in the model by $U_1 \leq 0$, is stretched in the spanwise direction, under the action of W_0 (where $\partial_z W_0 = -\partial_x U_0 \geq 0$). To this z-elongated region, a vertical velocity is generated by the pressure to ensure the continuity equation. This vertical velocity and the z-elongated region of U_1 form the spanwise vortex. Finally, by piecing together the mechanisms described in this chapter, a self-sustained process for wall-turbulence is proposed.

In chapter V, we focus on the spot spreading mechanism. First we analyse the coherent structures on the border between the laminar and turbulent regions. This reveals us the existence of many vortices with cross-stream axis extending all over the gap. The streamwise velocity component of these vortices is the streak (U_0). The vortices move parallel to the plates and we show that the origin of this motion is essentially due to the action of each vortex on the other. During their motions, these dipoles carry the other perturbation components such as the streamwise and spanwise vortices. This is the spreading mechanism. A simple 1D-model in terms of 8-PDEs is derived to corroborate it.

In chapter VI, we are interested by the outskirts of a turbulent spot. Outside

a spot, our numerical results show the development of large scale flow, extending over the whole gap, characterized by streamwise inflow and spanwise outflow, giving it a quadrupolar shape. The spot is associated to a region where the streamwise velocity correction (U_1) is dominantly opposed to the base flow, as seen by filtering out small-scale fluctuations. The origin of the quadrupole-like flow is traced back to the shearing of this negative correction by the base flow, whereas the correction itself is generated by the appropriate component of the local average of the small-scale Reynolds stresses (streaks and streamwise vortices).

Chapter VII is our concluding chapter. We summarize the work of this thesis and we present some questions that we intend to examine by going beyond the case of pCf and considering other wall flows experiencing a similar transition to turbulence, such as plane Poiseuille flow and Taylor-Couette flow in narrow gap.

Contents

Chapter 1

Introduction

The transition to turbulence in shear flows close to a solid wall still leaves open several problems of great practical importance. This situation arises because linear stability analysis is less fruitful for stable systems in which transient algebraic energy growth may become relevant than when exponentially growing modes are present. As a matter of fact, things are easier to understand in the case of supercritical instabilities —especially in closed-flow configurations, *e.g.* Rayleigh–Bénard convection and the Taylor–Couette instability— for which the classical tools of weakly nonlinear analysis are available. The situation is indeed delicate to handle in the case of a discontinuous transition marked by a competition between solutions arising from linear instability modes and other nonlinear solutions, *i.e.* in the *globally subcritical* case (Dauchot & Manneville (1997) (21)). A classical example is the plane Poiseuille flow —the flow between two parallel plates driven by a pressure gradient— which is linearly unstable only beyond some high Reynolds number R_c (Orszag (1971) (74)) while *turbulent spots*, *i.e.* patches of turbulent flow scattered amidst laminar flow and separated from it by well defined fronts, can develop in the flow for R as low as about $R_c/4$ (Carlson *et. al.*(1982) (16)).

The situation is even worse for the plane Couette flow (pCf in the following) — the simple shear flow driven by two plates moving parallel to each other, Fig. 1.1— which is stable for all R, hence $R_c = \infty$ (Romanov (1973) (84)), but experiences a direct transition to turbulence at moderate values of R ((61; 98; 22)). Standard modal and non-modal *linear* theory, as reviewed *e.g.* in Schmid & Henningson (2001) (88), is of little help to understand the main problem alluded to above, namely the *nonlinear* coexistence in physical space of these different solutions testified by the existence of turbulent spots.

A detailed understanding of this transition *to* turbulence (globally subcritical) via turbulent spots nucleation and growth, relies on (i) an understanding of microscopic processes such as the self-sustainment of turbulence and (ii) the mechanism by which it propagates into the laminar domain. In the other hand, some studies have been devoted to the transition from turbulent *to* laminar flow.

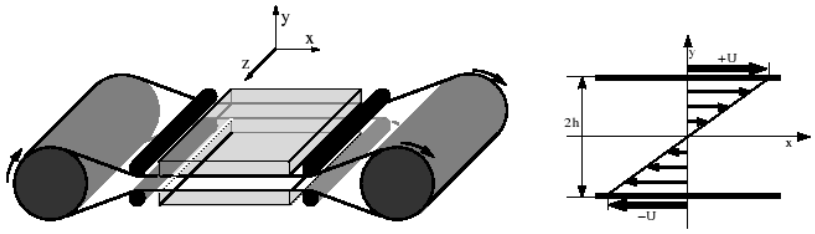

Figure 1.1: Left: Experimental set-up for plane Couette flow, used by the Saclay Group. Right: Laminar regime with linear velocity profile. Adapted from Manneville (2004) (64).

They were motivated by the determination of the stability threshold (usually noted R_{g}) and also to investigate the behavior of the transient lifetimes near this threshold.

We present some related works in §1.1. The development and growth of the spot is presented in §1.2. Some studies concerning the spreading mechanisms are summarized in §1.3. The process related to the self-sustainment of turbulence (inside the spot) is discussed in §1.4. Throughout this chapter, we use a common coordinate system with x in the streamwise direction, y along the normal to the wall and z in the spanwise direction. The base flow is U and the fluctuations are u, v, w. Most of the studies that we have found in the literature and which we present in this chapter, are related to the turbulent boundary layer flow. Few are concerned with the plane Couette or Poiseuille flow. The relevance of those studies in understanding transitional flow especially pCf is justified by the fact that turbulent flows in pipes, channels and boundary layers have some common features, investigated below.

1.1 Transient lifetimes

1.1.1 Introduction

As it seems to be strange, the study of the transition *from* turbulent *to* laminar state might bring some valuable elements to understand the transition *to* turbulence itself. For example, this approach permits one to determine, with a reasonable accuracy, the stability threshold (R_{g}).

Determining the distribution of the durations needed to relax from turbulent state towards laminar state when the control parameter is decreased below the threshold, was the aim of some studies. We summarize here some of them and outline a few hints for our own study.

1.1.2 Numerical and experimental studies

In phase space, we can consider that the laminar state is a fixed point. Since the plane Couette flow is linearly stable, all points in the neighborhood of this fixed point evolve towards it. The ensemble of these points form the basin of attraction of the laminar state. Far from this basin, there is the turbulent state with its complicated structure:an initial condition can remain turbulent while another one very close to it can relaminarize. Such a structure is known, in dynamical systems theory, as a chaotic saddle.

Some insight in this saddle can be obtained by studying the distribution of lifetimes of turbulent transients. Many researchers went this way, using both experimental and numerical methods, to collect a large number of lifetimes, for pipe flow and plane Couette flow. We will not describe the methods used in analyzing the transition and determining the lifetimes (usually based on the determination of the point in time where the energy drops below a threshold). For a fixed Reynolds number below the threshold R_{g}, the probability to stay turbulent for a duration of $t = \delta t_1$ is less than the probability to stay turbulent for $\delta t_2 \leq \delta t_1$. Theory of dynamical systems predicts a probability $\Pi \propto \exp -t/\tau(R)$, where τ is a characteristic decay time (also the lifetime). This exponential behavior was obtained, among others, by Darbyshire & Mullin (1995) (20) for pipe flow as in pCf experiments by Bottin & Chaté (1998)(11). The natural question that arises is how τ depends on R.

For pCf, lifetimes have been measured experimentally by Bottin & Chaté (1998) (11) in a large box with streamwise and spanwise lengths $L_x = 190$ and $L_z = 35$. They observed that τ increased continuously with R, suggesting a divergence at some finite value of R. By fitting their data, they concluded that the best fit for τ is $\tau \propto (R_{\mathrm{g}} - R)^{-1}$, where $R_{\mathrm{g}} = 323 \pm 2$ is the global stability threshold.

Peixinho & Mullin (2006) (78) run experiments in pipe flow and have obtained an exponential distribution of lifetimes. They have shown that $\tau \propto (R_{\mathrm{c}} - R)^{-1\pm0.02}$, where $R_{\mathrm{c}} = 1750 \pm 10$ is the critical Reynolds number. They pointed out that in dynamical systems theory, this behavior of τ is a generic feature associated with transient behavior where an attractor loses stability at a crisis.

Hof *et. al.* (2006) (45) presented new experimental data showing that the lifetime does not diverge but rather increases exponentially with R. This has been achieved by increasing the observations times (up to two order of magnitude) for turbulent transient in a long pipe flow (30 m). They showed that τ can be best approximated by $\tau^{-1} = \exp(a + bR)$ where a and b are two constants determined from the fit. By means of numerical simulations, they confirm the exponential fitting for τ (observations time around 3000 and the shorter extend of the numerical pipe). They proposed that reanalyzing some distributions found in the literature by subtracting a time t_0 to t in the expression of the probability

Π can substitute the exponential behavior of τ^{-1} by its linear scaling.

As a conclusion, determining the behavior of the transient lifetimes remains a controversial issue.

1.2 Turbulent spots

1.2.1 Introduction

Turbulent spot is commonly used to describe a turbulent region sitting in a laminar flow. During the transition process from laminar to turbulent flow, small turbulent spots develop. They can be considered as the "building block" of a space-time chaos. In a natural transition (as opposed to triggered), the first appearance of turbulent spots determines the start of transition location and the subsequent growth of the spots leads to the turbulent flow. The main characteristic of the transition is the coexistence of the two states turbulent and laminar.

Emmons (1951) (31) first recognized the intermittent nature of transitional flow and the role of the turbulent spots in the transition process. Pomeau (1986)(81) studied this transition and conjectured that it could be represented by a contamination process model, i.e., a model in which a laminar site becomes turbulent with some probability: the growth of the turbulent region results purely from a stochastic process (see §1.3 below).

Such a transition to turbulence has been studied recently. Many new techniques, as high-resolved direct numerical simulations (DNS) or stereo particle image velocimetry (PIV), have been employed to track the growth and movement of the spots. New phenomena have been observed and would lead to better understanding of spots dynamics. In the next section, some of these phenomena are presented.

1.2.2 Characteristics of turbulent spots

Attempts to investigate the interior structure of a turbulent spot and, in particular, the mechanisms involved in its development, have been undertaken recently by many researches.Only some studies are presented here.

Lundbladh & Johansson (1991) (61) studied the development of turbulent spots in pCf by means of direct numerical simulations (DNS). At that time, in 1991, due to the absence of experiments for this kind of study, their results represented a prediction of the physical situation. They found that spots were sustained for Reynolds numbers above approximately $R_g \sim 375$ and that their shape was elliptical with a streamwise elongation that was more accentuated for high Reynolds numbers. For $R = 300 < R_g$, the energy of the disturbed region decayed. The u-disturbance decayed more slowly, but at large times the remaining u-disturbance consisted merely of long longitudinal streaks of alternating low and

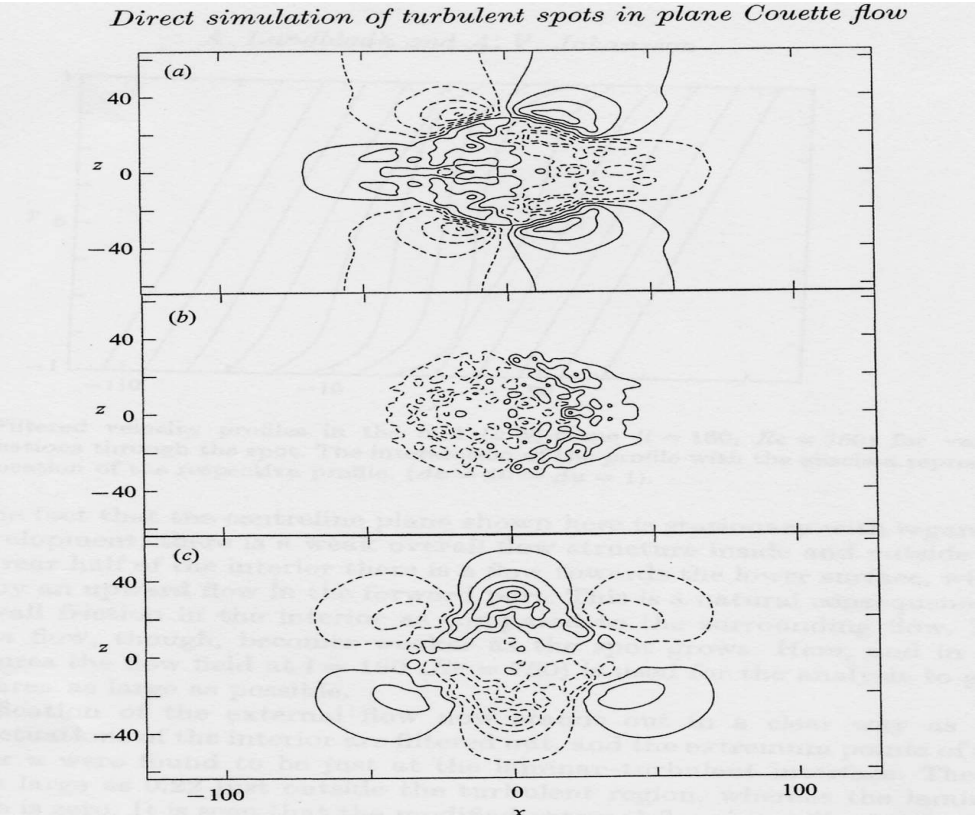

Figure 1.2: From (61). The isocontours of (a)-u,(b)-v,(c)-w velocity in the (x, z)-plane for $y = 0$. The solid contours represent positive value and the dashed contours represent negative values. There is an inflow toward the spot in the streamwise direction (represented by u) and an outflow from the spot in the spanwise direction (represented by w). The remaining distribution of v in this figure highlight a positive region at the leading edge of the spot and a negative region in its tail. Both regions are elongated in the spanwise direction.

high velocity, dominated by one specific spanwise wavelength. At $R = 375$ the turbulence was seen to be self-sustained as the region grew. From an analysis of the data, they found that the velocity field outside the spot was essentially two-dimensional in that it lacked a significant vertical component. Spatially filtered mean values were obtained by use of a Gaussian low-pass filter in wavenumber space. Various values of the filter length-scale were tested. The results were found to be rather insensitive to the choice of this length-scale. Figure 1.2 shows the averaged u, v, and w fields at the mid-plane $y = 0$. The modification of the external flow standed out in a clear way as the turbulent fluctuations of the interior were filtered out. They have seen that the modified external flow is totally dominated by the horizontal components and that there is a motion out from the

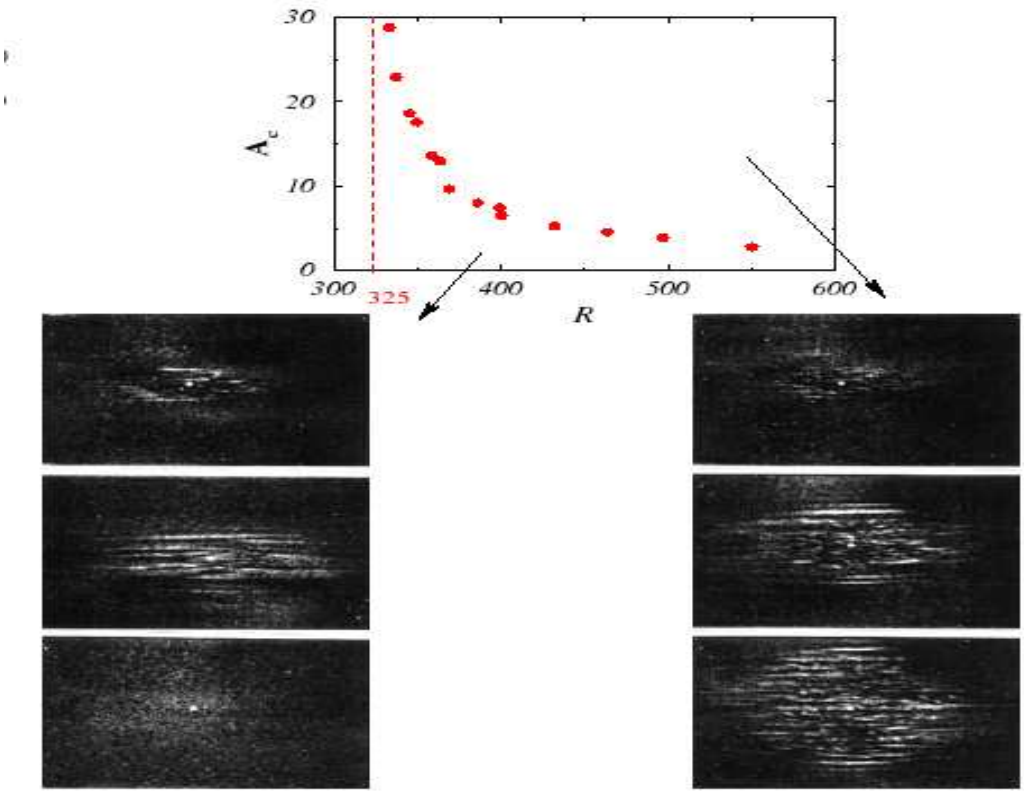

Figure 1.3: Experiments on turbulent spots by the Saclay group (1998). If the amplitude of the initial perturbation is sufficiently high, it gives rise to a growing turbulent spot, otherwise, it decays.

spot near the midpoint $x = 0$, contrasted with motion towards the spot at the leading and trailing parts (as we have found with our models). Notice that this motion shows a quadrupolar pattern outside the spot, which was not mentioned explicitly in the paper of (61). Finally, they found that spanwise growth increased with increasing R for low values, but leveled off to a constant rate at high R. As we will see later on, the investigations of Schumacher & Eckhardt (2001)(91) have shown the existence of the quadrupolar flow.

Dauchot & Daviaud(1994) (22) reported a detailed study of the transition to turbulence in pCf. Externally applied perturbations that trigger turbulent spots were made by injecting turbulent jets into the laminar flow. As shown in Fig. 1.3, they found that if the amplitude of the initial perturbation is sufficiently high, it gives rise to a growing turbulent spot, otherwise, it decays. All perturbations are observed to decay below $R = R_{\mathrm{u}} \approx 310$ so that the flow rapidly returns to the base state (the Reynolds number is defined as $R = U_{\mathrm{p}}h/\nu$, where U_{p} is the

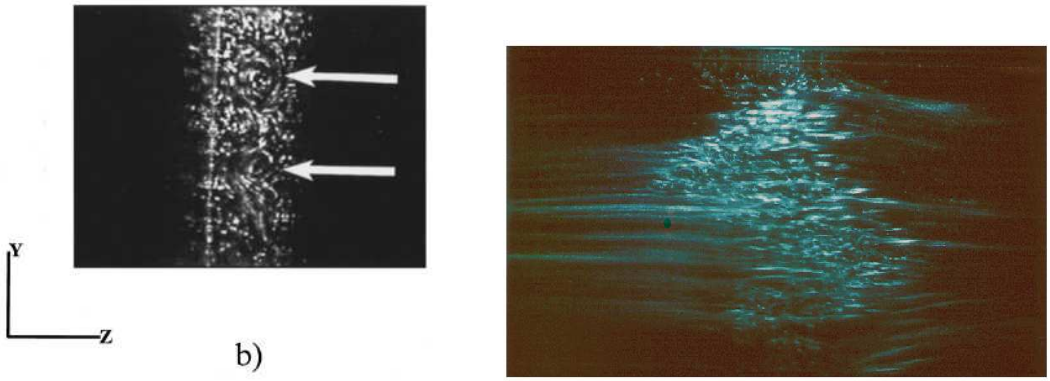

Figure 1.4: Some results of the Saclay group (1998). Left: Photograph of the gap in the (y, z)-plane using Pyroceram particles. It shows the cross section of vortical structures in the (y, z) plane at $R = 380$ as indicated by the arrows. This is a cross section of the streamwise vortices that have been observed to pervade the spot (right panel). The presence of these structures correlates well with the streaks in the (x, y) plane visualizations using Iriodin particles and shows that the streaks and streamwise vortices are correlated.

plate velocity, h is the half-gap between the plates and ν the kinematic viscosity of the fluid). Between R_{u} and $R_{\mathrm{g}} \approx 325$, localized finite-amplitude perturbations generate turbulent spots with finite lifetimes. These lifetimes increase as R_{g} is approached from below, while beyond this value, most of the spots no longer decay but on the contrary invade the system. A regime of uniform featureless turbulence is eventually obtained beyond $R_{\mathrm{t}} = 415$.

In the other hand, turbulent spots may form a variety of temporal shapes which can be distinguished easily because of a sharp laminar/turbulent interface. As these spots evolve, they grow, split and merge. The streakiness of the spot was visible, as clearly shown in Fig. 1.4.

Hegseth (1996) (38) carried out and experimental study of the coexistence of laminar flow and turbulent spots in pCf. He observed vortical structures in the (z, y) plane as shown in Fig. 1.4. The circular structures in the figure could be interpreted as cross sections of streamwise vortices that pervaded these spots. Their temporal behavior was quite complex and included events such as vortex creation, destruction and motion. These vortices almost filled the entire gap.

1.3 Spreading mechanisms

Roughly speaking, a complex spatiotemporal behavior that involves two phases (a simple one, that describes a so-called laminar state and a complex one, that

has been called turbulent state) is called spatiotemporal intermittency. It denotes a complex dynamical behavior which is observed in spatially extended physical systems.

The two states are separated by a front and the laminar state disappears through the propagation of this front. Two types of front have been defined in the literature: pulled and pushed.

In a complete review by Van Saarloos (2003)(105), the name pulled front comes from the fact that such a front is being "pulled along" by the leading edge of the front, the region where the dynamics of the front is governed by the equations obtained by linearizing about the unstable state. In this way of thinking, a pushed front is being pushed from behind by the nonlinear region.

From the theoretical side, little is known about the question of coexistence between laminar flow and turbulence and the possible mechanisms of (pulled/pushed) front propagation leading to the spreading of turbulent spot.

This question was discussed by Pomeau (1986)(81) from a fully abstract point of view as a nucleation problem in terms of first-order phase transition. He argued that when one of the competing states was chaotic, the competition could be understood in terms of a stochastic contamination process in the same class as directed percolation. In fact, directed percolation (DP) is the common name for spreading processes with active ("live") sites and an absorbing ("dead") state. Note that DP is a purely statistical process with no a priori dynamics; at each time step, a site can become alive with probability p, if and only if at least one of its neighbors was alive at the previous time step. For $p \approx 0$ the process rapidly terminates whereas for $p \approx 1$, the live sites spread without limit. The concrete connection between DP and subcritical transition to spatio-temporal intermittency in hydrodynamic context, is still an open question.

Based on experiments in boundary layers flows, Gad-El-Hak *et. al.* (1981)(33) proposed a mechanism called "growth by destabilization". If the mean transport velocity of the spot is lower than the mean velocity of the surrounding flow, the spot acts as a blockage and the laminar flow field outside the spot is accelerated. The linear stability of the profile maybe be lost and the growth of infinitesimal perturbations occur.

Dauchot & Daviaud (1994)(22) discussed this mechanism in an experimental study. They found velocity profiles indicating that the flow is accelerated outside the spot. They also envisioned another mechanism related to the transient growth of perturbations. But a direct demonstration of both mechanisms has not yet appeared.

Spanwise spreading of the turbulent spot was investigated by Schumacher & Eckhardt (2001) (91). They performed direct numerical simulations of Navier-Stokes equations for plane Couette flow with free-slip boundary conditions and added a bulk force to drive the flow. They found that the front advances at a rather well-defined speed in the spanwise direction and that the presence of the turbulent spot gives rise to a large-scale spanwise outflow.

They defined v_f, the velocity of the turbulent spanwise-advancing front. They showed that this velocity v_f was different from the large-scale spanwise outflow velocity but they conjectured that this outflow had profound consequences for the spreading of the spot. They also analyzed the linear spreading velocity $v^\star$ by linearizing the flow equations about a laminar state viewed as a sum of the base flow and this large-scale outflow, using an Orr-Sommerfeld equation. The measured front speeds in the numerical simulations were about a factor 10 larger that the value of $v^\star$ obtained this way, leaving no doubt that the spanwise spreading of the turbulent spot is not governed by a linear mechanism.

The question of which mechanism is involved in spot spreading (in shear flows in general) is to a large extent open. We were motivated to study the spot spreading within our model.

1.4 Self-sustainment of wall-turbulence

In this section, some studies related to the self-sustainment of wall-turbulence are presented. Most of the investigations in this field were concerned with boundary layer, few with pCf or Poiseuille plane flow. We have decided to present some of them, since they can give us valuable hints to our study.

1.4.1 Definition of coherent structures

It is natural that in the aim to understand the wall turbulence, we use flow patterns as building blocks. The purpose of this section is to define and describe these elements in a simple way. These elements are called coherent structures, noted as "CS". Townsend in 1959 gave one of the first definition to coherent structures: "a flow pattern which is of finite size, mechanically coherent and resistant to disintegration". One of the first CS was proposed by Theodorsen in 1951. He imagined that a vortical element, with its spatial structure looks like a horseshoe (Fig. 1.5), arose from the wall to transport fluid ($v \neq 0$). This horseshoe vortex has two legs located near the wall, forming two counter-rotating streamwise vortices, another important CS in wall-turbulence. He introduced this concept, from a phenomenological point of view, to explain and to link all the observed turbulent flow events (defined later on).

Streaks were also among the first and most important elements identified in the early experiments. They were observed near the wall. In a review article, Corrsin (1955)(17) discussed some experiments concerning the behavior of dyed fluid being replaced by clear fluid in a tube flow. He stated:"The significant property seems to be the strong orientation into streamwise filaments of the residual dye. Presumably this indicates a predominance of axial vorticity near the wall, sweeping the dyed wall fluid into these long narrow stripes." The existence of many streamwise vortices near the wall, lifting up near-wall fluid, is a possible

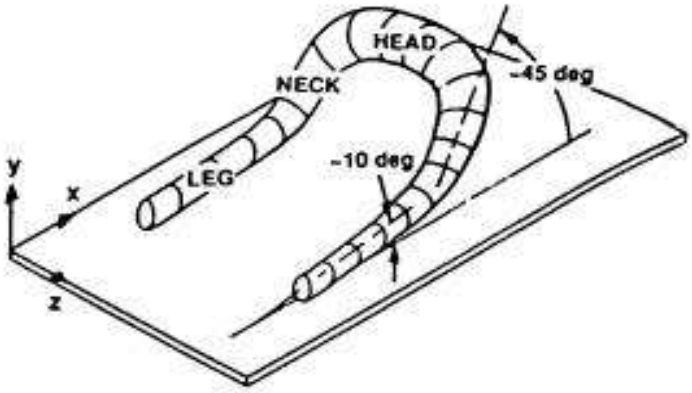

Figure 1.5: Different parts of a hairpin vortex (Theodorsen, 1951). A vortical element, with its spatial structure looks like a horseshoe, arose from the wall to transport fluid ($v \neq 0$) and produces Reynolds stress ($-uv \neq 0$).

explanation. Since the near-wall fluid has a low speed, the term "low-speed streak" is often used. On the other side of the vortex, fluid from a higher speed region is brought closer to the wall. The high-speed regions are devoid of dye because the fluid comes from region far from the wall.

The term "streak" originated from the behavior of flow visualization markers. Nowadays, we use *streaky* flow to describe a $U(y, z)$ velocity profile that has an oscillation in the z-direction. As we will see later on, this streaky profile is used in stability considerations.

1.4.2 Kinetic energy production

It is of interest to look at the spatial region where turbulent kinetic energy is produced. The Reynolds-Orr equation gives turbulence production $P = -\langle uv \rangle \partial_y U$ where $-\langle uv \rangle$ is one component of the (averaged) Reynolds stress. We are interested in the processes that make essential contributions to P, i.e., why there is, somewhere in space, a correlation between u and v such that $-uv$ is positive (since $\partial_y U > 0$) rather than negative.

When flow is ejected from the wall, by a vertical velocity $v > 0$, it creates low speed streaks, $u < 0$, since the streamwise velocity at this location is now $0 < U(y) + u < U(y)$. Hence, this ejection event makes a positive $-uv$ contribution to the Reynolds stress and is defined as Q_2 event. Similarly, any coherent event producing a Q_4 contribution is frequently called a "sweep". A high speed streamwise-flow comes close to the wall by negative vertical velocity v. It generates positive streaks since near the wall, the streamwise velocity is now $U(y) + u > U(y)$, i.e. $u > 0$. Hence, this sweep event makes also a positive $-uv$

contribution to the Reynolds stress. A general concept is that the Q_2 and Q_4 events occur on each side of a streamwise vortex and hence those regions make a significant contribution to the energy production. For this reason, elucidating the dynamics of the streamwise vortices is crucial in understanding the production of turbulence.

1.5 Characteristics of self-sustaining mechanisms

To summarize the previous sections, we state that where Reynolds stress $-uv$ is positive, kinetic energy is produced. Since the key structure involved in such production are the streamwise vortices, which appear and disappear, we may understand that there is a cycle governing the generation of such vortices. The occurrence of this cycle guarantees the self-sustainment of turbulence. The cycle can be envisioned as follows: many different structures constitute the skeleton of this cycle and they are linked together by some mechanisms. The main effort to provide is to establish the cause-and-effect relationship between these structures and the mechanisms behind their generations. Many studies are concerned with identifying the structures, based on experimental or DNS data. A few others focus on the mechanisms leading from one structure to another (actually there are very few mechanisms, the well known is the lift-up, by which, the streamwise vortices generate the streaks).

A self-sustaining cycle has several characteristics. The first might be the time scale of the repetition of events. The time interval between the coherent structures should be the same, or at least comparable between the cycles. Another important characteristic is the spatial features of the coherent structures. It is not clear that the generated streaks have the same amplitude (or strength) and the same spanwise width as the previous streaks. Same question holds for the streamwise vortices, especially if they are or not strong enough to restart the cycle.

Another characteristic concerns the nature of the process. Some of them include an instability, whereas in others, a vortex can generate another vortex. Hence, in discussing self-sustaining mechanisms, we will use two main classes (for a complete review, see Panton (1997) (76) and Panton (2001)(77)). The "parent offspring" class is defined by having a flow structure that develops in time to replicate itself without involving an instability. The second class has, during part of the cycle, a velocity profile that is unstable to small disturbances.

1.6 Self-replicating mechanisms

Let us first summarize generally accepted ideas ((77)). First, there are the streaks. It is almost universally agreed that the streamwise vortices near the wall sweep low speed fluid into the low-speed streaks (lift-up mechanism). On the other side of this vortex, high-speed streaks are generated. This produces a characteristic streak velocity profile (u) with spanwise variation. Together with the vertical motion v of the streamwise vortices, Reynolds stress are produced.

Many people view the streamwise vortices as the legs of hairpin vortices (see Fig. 1.5). From this viewpoint, the self-sustaining mechanism centers on how hairpin vortices are produced given the initial situation as a fully developed turbulent state. Here we focus on how a hairpin vortex is generated, or *springs* from another hairpin vortex.

Brooke & Hanratty (1993)(15) performed computation of a channel flow and examined vorticity patterns in (y, z) planes. Viewing (y, z) planes enables one to see streamwise vortices, even if the vortex axis is not exactly in the (y, z) plane. They found that a new vortex is born at the downstream end of the parent on the down-wash side. This end is lifted from the wall and they refer to it as the detachment point. They remarked that the vorticity in the child vortex is of the opposite sign to that of the parent and that the regeneration is not influenced by outer flow events. Thus, they envisioned a regeneration process that is entirely within the inner region.

An interesting contribution is given by Heist *et. al.* (2000)(43). They identified a new process that forms about 30 percent of the streamwise vortices. This was accomplished by examining the changes, with time, of the turbulent field obtained from a direct numerical simulation of turbulent flow in a channel. Streamwise vortices create a shear layer by pumping low momentum fluid from the wall. One or more small spanwise vortices are formed at the top of this layer. They grow in size and rotate in the direction of flow. The main focus of Heist's paper is not on how they form but on what happens after they form. Figure 1.6 is a plan view of their DNS results. Vortex A is followed as a parent that produces vortex B. Vortex B grows in the spanwise direction and then elongates in the streamwise direction and intensifies.

Previous investigators have suggested that spanwise vortices could have a direct role in the formation of streamwise vortices. A number of investigators have argued that spanwise vortices play a key role in sustaining turbulence. Different proposals have been made to explain how this occurs. A *common assumption* is that spanwise vortices evolve into hairpin vortices, but the details of this process are not given (see e.g. (77)).

A common picture (among many others) about the hairpin vortex generation is presented in (76). A streamwise vortex collects fluid from near the wall and creates a low-speed streak. Next, the low-speed streak region forms an obstacle for the faster moving stream. This event takes place as long as the stream-

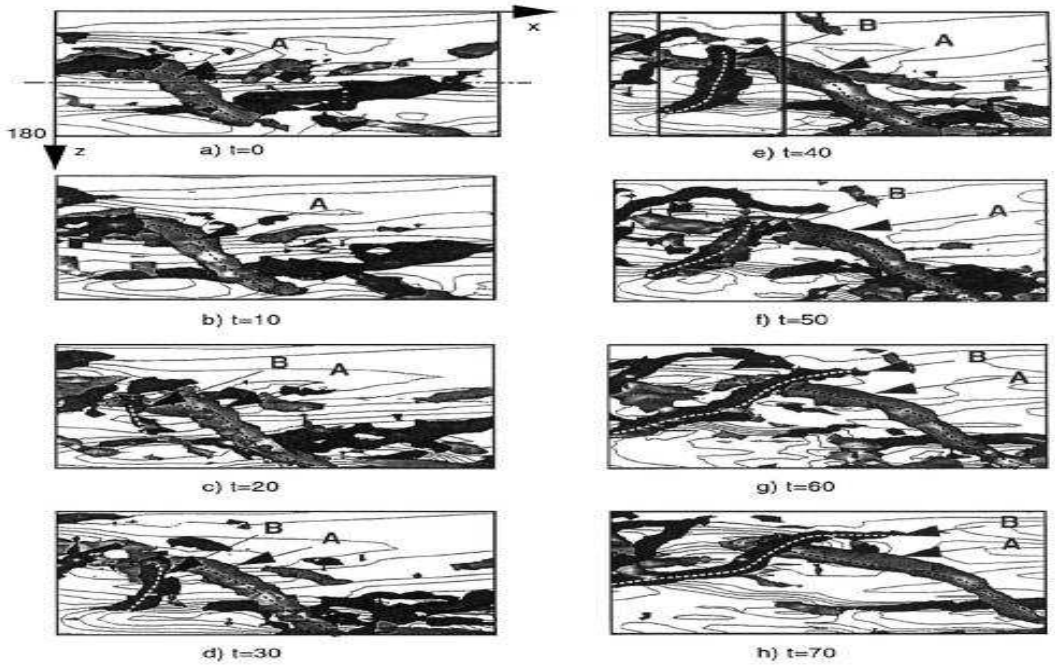

Figure 1.6: Birth of vortex B and its growth and elongation. From (43).

wise vortices exist and pump more fluid into the streak area. Hence, this lifted area produces a streamwise shear, due to the impingement of the faster moving stream on it. This lifted region produces a stronger $U(y)$ shear layer which rolls up, much like a Kelvin-Helmholtz cat's eye, into a vortex arch or head. The vortex lines in the head extend down. As the head is convected downstream, the legs are stretched and the swirling thereby intensified. Thus, the hairpin formation process consists of streak lift-up, shear layer intensification, and hairpin re-formation.

1.7 Instability-based mechanisms

The class of self-sustaining processes involving instability mechanisms is now discussed. During part of the cycle, a velocity profile is unstable to infinitesimal perturbations and a linear theory is developed. The velocity profile, which must exist for sufficient time for the instability to develop, can be the base flow. A perturbation is added to it and the question is, does this disturbance grow or not. More specifically, what kinds of perturbations grow and how fast do they grow. In order to form a complete cycle, the instability should ultimately lead back to produce the initial velocity profile.

A disturbance and a velocity profile are the only common elements of a sta-

bility analysis. The next choice concerns the equations that are used to follow the development of the disturbance. Typical laminar flow stability analysis uses linearized equations under the assumption that they govern the initial development of infinitesimal disturbances. Furthermore, linear equations have many mathematical properties. They allow an analysis by normal modes, i.e., the eigenfunction and eigenvalues of the system. The fastest exponentially growing normal mode determines the characteristics of the most-unstable infinitesimal disturbance.

In some cases as pCf, this approach fails. However, the linearized Navier–Stokes equations are non-normal and their eigenfunction are not orthogonal. This allows certain disturbances that are composed of several normal modes to grow to large amplitudes. Factors of 1000 or more have been found. At large times the disturbance approaches the behavior of the last decaying eigenfunction. This transient growth is algebraic and for that reason this phenomenon is also called algebraic growth (as we see later on, Schoppa & Hussain used this transient growth to show that normal modes growth is not sufficient to trigger nonlinearity).

Trefethen & Trefethen (1993) (100) make an analogy with vectors. Consider two almost oppositely directed basis vectors that have large amplitudes. These are normal mode components. Their resultant, the perturbation, has only a small magnitude. Then, one basis vector magnitude decreases with time while the other is unchanged. This causes the resultant perturbation to increase in amplitude. Ultimately, the behavior of the resultant perturbation follows the dominant eigenvector and decreases (stable case).

Transient growth was ignored for many years. Recently, it was realized that it could lead to profiles that, because of their large amplitude, are subject to secondary instability and or nonlinear effects. Transient growth has a history of development and a nice introductory review is in (100).

Hence, in the instability mechanism class there are many questions. They concerns the nature of the perturbations (finite or infinitesimal), the equations to be used and the approach (normal mode or transient growth). Note finally that what happens when nonlinear effects become important is another (difficult) issue.

1.7.1 Inflectional profiles

In the first flow visualization experiments, Kline & Reynolds (1967)(54) noted an oscillation in the dye streak and proposed that an instability existed. The conjecture was that the lifted low-speed streak produced an instantaneous $U(y)$ profile that had an inflection point. Many authors made an analogy with linear stability of plane two-dimensional profiles. Such $2D$ profiles with an inflection point could be unstable (Rayleigh's criterion). The inflection point is a necessary, but not a sufficient condition. Rayleigh's criterion has been superseded by Fjørtøft theorem, not developed here (see (88)).

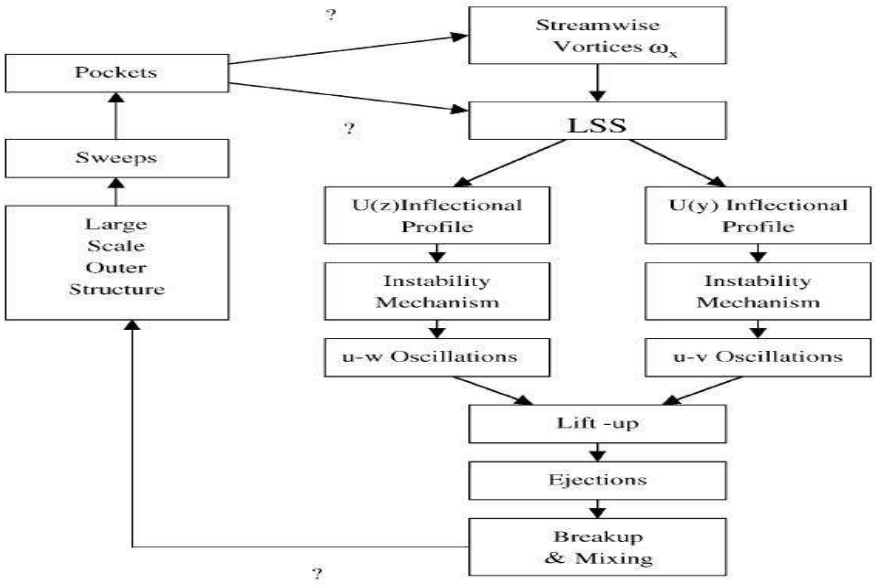

Figure 1.7: Schematic of self-sustaining mechanism with inflectional instabilities. Adopted from (7) (in (77)).

Blackwelder (1998) (7) noted that $U(y, z)$ profile of a streak also has inflections in the z-direction. Figure 1.7 illustrates the self-sustaining relationships envisioned by (7). The figure shows instability mechanisms in both $U(y)$ and $U(z)$. A question mark indicates uncertain interactions and obscure mechanisms.

On the other hand, the study of Brandt *et al.* (2003) (14) was motivated by the conjecture that the streak instability, being essentially wake-like in the spanwise direction, could give rise to an absolute instability, as in classical wakes, and then turbulence. Their conclusions do not confirm this conjecture; the streak instability is produced sufficiently high above the wall, in regions where local streamwise velocities are large so that perturbations are "advected away". Concerning the transition to turbulence, it is important to note that the relation of the modal secondary instability to streak breakdown has not been definitely proved (see also the premise of streaks-instability in general, later on).

1.7.2 Minimal flow unit

The minimal flow unit is a concept introduced by Jimenez & Moin(1991)(49). They used the DNS code developed by Kim *et al.* (1987)(50) for a turbulent channel and reduced the size of the channel width. The idea is to isolate a basic process of wall turbulence. When the spanwise box width is large enough, turbulence can be maintained on only one wall. The flow has only one streak and a streamwise vortex. Calculations confirmed that the cycle is regenerative,

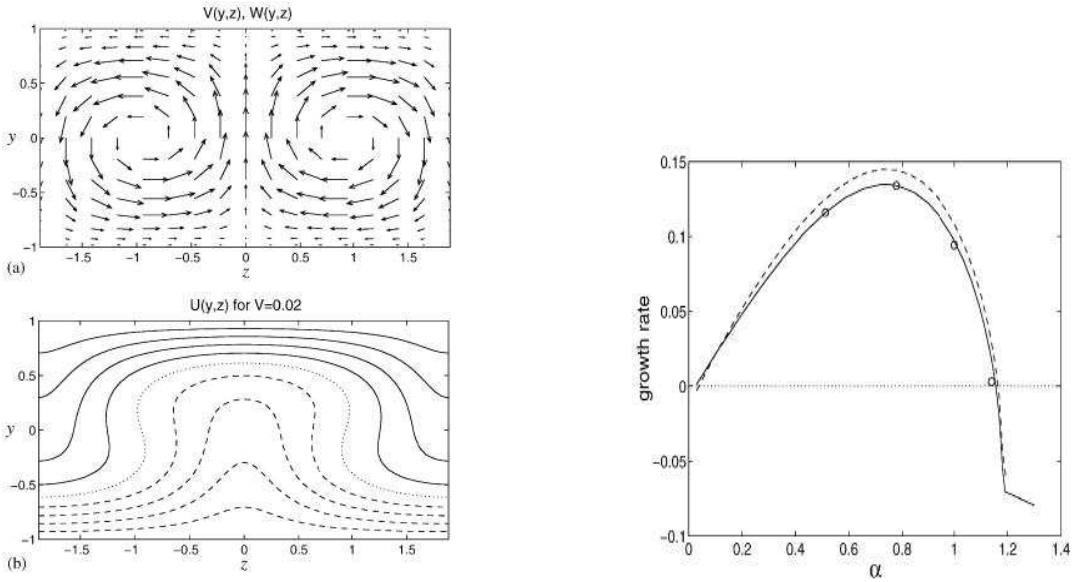

Figure 1.8: Left: (a) Streamwise vortices $(0, V(y,z), W(y,z))$ in Couette flow. (b) Contour plot of the initial streak profile $U(y,z)$ produced by the vortices. $V = 0.02$ is the strength parameter. Right: Growth rate vs. α. From Waleffe (1997).

however, it had an unrealistically long time scale, perhaps because of strong viscous effects. Jimenez & Pinelli (1999) (48) continued along this approach. A noteworthy difference was that the channel was wider, wide enough for two or three streak profiles in the spanwise direction and the flow could also contain some large-scale outer structures. By various artificial modifications to the calculations, they tested the viability of the streak instability mechanism and the parent-offspring mechanism. They concluded that a streak instability cycle is possible and entirely exists in the near wall region. This self-sustaining cycle needs no interaction with the outer region. On the other hand, the parent-offspring cycle did not appear viable under these severely viscous conditions. As the authors noted, these conclusions might be modified at higher Reynolds number and/or for larger domains. However, they believed that the streak instability mechanism is the dominant self-sustaining mechanism.

1.7.3 Streaky velocity profiles

We discuss here the "instability" study of the streak profile $U(y,z)$. Waleffe & Kim (1998)(102) and Waleffe(1997) (103) investigated the stability and regeneration of streak profiles in pCf. The streaky velocity profile is produced as follows. Starting with the linear laminar profile, they impose streamwise vortices

structures that extend across the whole channel. After about a quarter of a revolution the vortices redistribute the flow to produce the streaky profile $U(y,z)$ as given in figure 1.8 (a,b). Then, the streaky profile is analyzed using linear viscous equations. They impose a perturbation of a form that is sinuous in the x-direction,

$$v = exp(\lambda t)exp(i\alpha x)\sum v_n(y)\sin(n\gamma z).$$

Results for the most unstable fundamental sinuous mode are shown in figure 1.8. The maximum growth rate for a spanwise mode with $\gamma = 5/3$ is 0.135 for a wavenumber $\alpha = 0.74$. Within this streak instability, the self-sustaining process proposed by Waleffe (1997) (103) has the following three events:

- 1- Streamwise rolls redistribute the mean flow to form streak profiles.
- 2- A sinuous streamwise disturbance leads to an instability of the streak profiles.
- 3- Nonlinear feedback of the unstable mode injects energy to reform the rolls.

Process (1) is well known. Process (2) is observed in the Gortler flows, but is so sensitive to the used streaky velocity profile and one needs to establish that it occurs in pCf. Process (3) is an essentially new and obscure sequence.

Furthermore, we may wonder if there is a relation between the perturbation spanning all the gap as in Waleffe calculation and the near wall region in turbulent boundary layer. In fact, the Couette flow where these events occur does not have two turbulent wall layers, one on either wall, but a turbulent process within the *entire* channel. However, in (103), the distance between the walls is $40y^+$ units (This is roughly equivalent to the "buffer region", in boundary layer terminology). The entire flow might be considered as a wall region with a moving wall on it. Nevertheless, as with the minimal channel calculations, the main supposition is that the major characteristics of the process are similar to those in a traditional wall layer. In other words, the mechanisms underlying the generation of the streamwise vortices spanning all the gap of pCf would be the same in the near wall region of a traditional turbulent boundary layer. This assumption is certainly correct for some range of Reynolds number and it would be interesting to guess whether this Reynolds number is very large or just moderate.

Schoppa & Hussain (2002)(90) examined the turbulent flow that develops in a channel driven by a pressure gradient. They use a minimal channel of $L_x^+ = 300, L_z^+ = 100$. In this channel flow a mean $U(y)$ is constructed so that the upper wall is laminar-like and the lower wall turbulent-like. Their first calculation was a linear stability analysis. It identified a sinuous, linear, inviscid instability that only occurs if the streak-profile strength is sufficient. In this analysis the base-flow streak profile is taken as:

$$U(y,z) = U(y) + \frac{\Delta u}{2}\cos(\beta z)yexp(-\eta y), \quad V = W = 0.$$

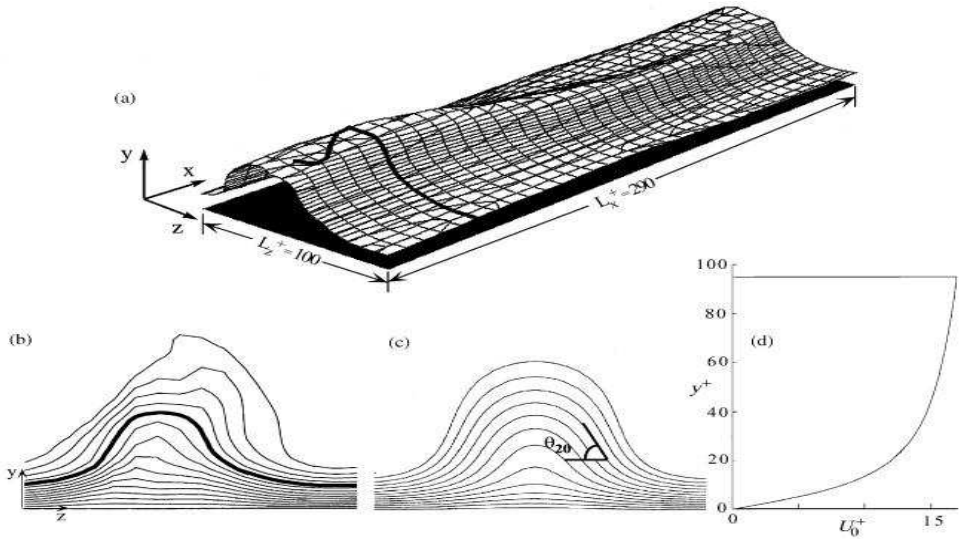

Figure 1.9: Low-speed streak. (a) Realization from DNS of minimal channel. Isosurface where $U = 0.55U_0$: (b) Typical velocity contours in (y, z) plane. Bold line is same in (a) and (b). (c) Similar contours for profiles used in stability calculations. Streak strength parameter $\theta_{20} = 56$ is shown. (d) Mean velocity profile for half-channel. Adapted from (90).

Here β is chosen to give a streak spacing of 100 and η chosen to give a plateau in y-vorticity at $y^+ = 10 - 30$. Instead of using $\frac{\Delta u}{2}$ to indicate the strength of the streak profile, a more physical concept was introduced. The streak profile strength is denoted by θ_{y+}, the maximum inclination of a base-flow vortex line at $y+$. This occurs on the flank of the streak. Figure 1.9 shows the base-flow profile and the (y, z) plane velocity contours with $\theta_{20} = 56$ indicated. Results of the stability analysis (the growth rate vs. the streamwise wavenumber) show that only streaks with $\theta_{20} \geq 48$ are unstable. Schoppa & Hussain did not believe that linear instability is a dominant mechanism in the self-sustaining process. They used the database of [Kim *et al.* (1987)(50) and found that the unstable streaks were only a small fraction of the streak population. Thus, the occurrence of a normal mode mechanism was small. In addition, they noted that the time scale for viscous diffusion to destroy the streak profile was short. For example, a streak profile with intensity $\theta_{20} = 56$ decayed to $\theta_{20} = 50$ in $t^+ = 30$. The third reason was that normal mode growth rates were very small. For example the most unstable mode for $\theta_{20} = 56$ grew by a factor of two when diffusion of the base flow was included.

As described earlier, researchers became *aware* of non-normality and they started to appreciate that a normal mode stability analysis is only a partial answer. The non-self adjoint nature of the Navier-Stokes equations means that

the unstable normal modes are not the only mechanism of perturbation growth. Perturbations grow algebraically to large levels and then die off exponentially or become an unstable normal mode. The important point is that when the disturbance is at a large level, it is essentially a new flow pattern that can initiate other events. Schoppa & Hussain (2002) (90) chose a perturbation in the form:

$$w = W \sin(\alpha x) y exp(-\eta y)$$

i.e. not a normal mode (but belongs to the eigen subspace if η is degenerate). They compared the energy of a normal mode and a transient perturbation, denoted as streak transient growth STG, as a function of time. The transient perturbation grew by a factor of 20 compared to the normal mode's growth of a factor of two. According to the author's minimal channel calculations, the perturbation continued to grow to a level where nonlinear equations had to be used. The DNS calculation yielded a regeneration of the streamwise vortex. Here starts the second part of the work of (90). They found that the stretching of the streamwise vorticity ω_x by the streak waviness $\partial_x u$, i.e. the term $\omega_x \partial_x u$, caused formation of a streamwise vortex, x-elongated region of ω_x. Presumably the cycle was then completed by formation of a new streak profile by this vortex. In this thesis, our findings are compared to the results of (90) (chapter 5).

1.7.4 Conclusions on instabilities

The idea that streamwise vortices are created by the breakdown of the lifted streak due to its inflectional point in the (x, y) plane is legitimate but arguing that, in turbulent pCf, the streamwise vortices result from an inflectional instability would be unwarranted. As noted by Schoppa & Hussain (2002) (90) themselves, the occurrence of such instability in turbulent flow has to be proved. Its nature and its origin have to be explained too.

1.8 Conclusions of the chapter

Transition to turbulence in pCf is marked by a competition between patches of turbulent flow scattered amidst laminar flow. Hence, a detailed understanding of this transition to turbulence (globally subcritical) via turbulent spots nucleation and growth, relies on (i) an understanding of microscopic processes such as the self-sustainment of turbulence and (ii) the mechanism by which it propagates into the laminar domain. Unfortunately, elements of answer to these problems are expected perhaps no longer from the detailed study of output of direct numerical simulations or experiments, as shown in this chapter, but rather from modeling that might provide heuristic explanations to be further tested in experiments either in the laboratory or in the computer. Most rational modeling

approaches are developed through truncations of appropriate Galerkin expansions of the primitive equations. Such approach is the kernel of the next chapter.

Chapter 2

Modeling plane Couette flow

2.1 Introduction

Plane Couette flow which is stable for all R, experiences a discontinuous transition marked by a competition between *turbulent spots*, *i.e.,* patches of turbulent flow scattered amidst laminar flow and separated from it by well defined fronts. A detailed understanding of this transition to turbulence via turbulent spots nucleation and growth, relies on an understanding of microscopic processes such as the self-sustainment of turbulence and the mechanism by which it propagates into the laminar domain.

Direct numerical simulations of the Navier–Stokes equations (DNS) have been heavily used to identify elementary processes involved in the sustainment of turbulence within the spots. However they produce massive data sets requiring a lot of post-treatment before giving useful hints.

The alternative approach is the development of models at different levels of abstraction depending on the question under scrutinity ((67)). From the observation of near-wall turbulent flow, and its reduction to a so-called *minimal flow unit*, Waleffe was able to derive a differential model involving the amplitude of a few modes associated to coherent structures ((103)), a Galerkin-like approach that was made more systematic by Eckhardt and co-workers (e.g., (28)). Such models indeed enlighten some of the mechanisms involved in the sustainment of turbulence and the competition between laminar and turbulent states at the fractal border of the basin of attraction of laminar flow according to the abstract phase space viewpoint underlying the concept of *temporal* chaos. However, their low-dimensional nature does not allow one to approach such problems as spot propagation that require the explicit reference to physical space. When similar questions were posed for convection, *i.e.* pattern formation, it was found particularly valuable to pass from ordinary differential systems that can only deal with the time behavior, such as the Lorenz model, to partial differential equations (PDE) that also account for space dependence, *e.g.* the Swift–Hohenberg model

((97)) and its numerous variants, in order to diagnose *spatio-temporal* chaos.

This chapter is concerned with the derivation of a closed set of PDEs appropriate to the plane Couette flow. This case is particularly interesting since, by contrast with other wall-bounded flows such as the Poiseuille flow or the laminar boundary layer (Blasius) flow, it completely lacks linear instability and the absence of downstream advection makes it practical to observe the long term dynamics of spots, a crucial element of the subcritical transition to turbulence.

The space-time dependent models to be developed below are mostly intended to attack the two main problems: how the spots get sustained at moderate R, and how they contaminate the laminar flow.

Contrasting with the regime of developed turbulence taking place at large R, which requires a refined space-time resolution able to account for the cascade toward "small" scales, the transitional regime around R_g involves structures that appear to be "large," *i.e.* to occupy the full gap between the plates, and "coherent." In turn, a model in terms of a few well-chosen modes with low wall-normal resolution should be sufficient for describing spots and understanding their dynamics. The amplitude of these modes will then be taken as functions of the in-plane coordinates. This is the reason why we speak of *2.5-dimensional models*. In this terminology, the number 2 stands for the full in-plane dependence (x, z) and the suffix .5 suggestively expresses that the dependence on the third, cross-stream, coordinate y is only partly taken into account through low order truncation. In the next section §2.2, we present the primitive set of equations and we derive our no-slip model using the Galerkin method. In §2.3, we give a glimpse on the derivation of models with stress-free boundary conditions.

2.2 No-slip model

The Navier-Stokes equation and continuity condition for an incompressible flow read:

$$\partial_t \mathbf{v} + \boldsymbol{\omega}.\mathbf{v} + 1/2\boldsymbol{\nabla}\mathbf{v}^2 = -\boldsymbol{\nabla}p + \nu\boldsymbol{\nabla}^2\mathbf{v}, \tag{2.1}$$

$$\boldsymbol{\nabla}\cdot\mathbf{v} = 0\,, \tag{2.2}$$

where $\mathbf{v} \equiv (u, v, w)$, p is the pressure and ν is the kinematic viscosity. Further, $\boldsymbol{\nabla}^2$ denotes the three-dimensional Laplacian. We have rewritten the nonlinearity using the identity $\mathbf{v}.\boldsymbol{\nabla}\mathbf{v} = 1/2\boldsymbol{\nabla}\mathbf{v}^2 + \boldsymbol{\omega}.\mathbf{v}$, with $\boldsymbol{\omega} = \boldsymbol{\nabla}^t\mathbf{v} - \boldsymbol{\nabla}\mathbf{v}$.

In the following we use dimensionless quantities. Lengths are systematically scaled with h, and U_p stands for the velocity scale, hence a basic velocity profile $U(y) = U_b y$ for $y \in [-1, 1]$ in the no-slip case ($U_b = 1$). The equations are further developed for the perturbation (u', v', w', p') to the laminar basic flow:

$u = U(y) + u'$, $v = v'$, $w = w'$, $p = p'$, so that (2.1,2.2) accordingly read:

$$\begin{aligned}
&\partial_t u' + (\partial_y u' - \partial_x v')v' + (\partial_z u' - \partial_x w')w' + \partial_x E'_{loc} \\
&\quad = -\partial_x p' - U\partial_x u' - v'\partial_y U + R^{-1}\boldsymbol{\nabla}^2 u' \,, \qquad (2.3)\\
&\partial_t v' + (\partial_x v' - \partial_y u')u' + (\partial_z v' - \partial_y w')w' + \partial_y E'_{loc} \\
&\quad = -\partial_y p' - U\partial_x v' + R^{-1}\boldsymbol{\nabla}^2 v' \,, \qquad (2.4)\\
&\partial_t w' + (\partial_x w' - \partial_z u')u' + (\partial_y w' - \partial_z v')v' + \partial_z E'_{loc} \\
&\quad = -\partial_z p' - U\partial_x w' + R^{-1}\boldsymbol{\nabla}^2 w' \,. \qquad (2.5)\\
&0 = \partial_x u' + \partial_y v' + \partial_z w' \,, \qquad (2.6)
\end{aligned}$$

where $E'_{loc} = \frac{1}{2}(u'^2 + v'^2 + w'^2)$.

The Galerkin method is a special case of a *weighted residual method* ((32)). It consists here in forcing the separation of in-plane and wall-normal coordinates by expanding the perturbations (u', v', w', p') onto a complete basis of y-dependent functions *satisfying the BCs* with *amplitudes* dependent on (x, z, t). The equations of motion are then projected onto the *same* functional basis, using the canonical scalar product. The main modeling step is then performed when truncating these expansions at a low order and keeping the corresponding number of residuals in order to get a consistent and closed system governing the retained amplitudes. The no-slip boundary conditions for the vertical velocity component are:

$$v'(y = \pm 1) = \partial_y v'(y = \pm 1) = 0 \qquad (2.7)$$

obtained by combining the continuity equation (2.6) to the conditions

$$u'(y = \pm 1) = w'(y = \pm 1) = 0 \,. \qquad (2.8)$$

To satisfy these conditions, we take a basis made of polynomials in the wall-normal coordinate y, which also forms a family of functions closed for multiplication and differentiation. We do not use Chebyshev polynomials fully adapted to highly resolved DNS ((6)) because, in spite of their good orthogonality properties, they do not permit a straightforward account of the BCs at the low truncation orders we are interested in. By contrast, we can easily construct individual basis functions all satisfying the BCs arising from the no-slip conditions (2.7,2.8) and develop a strict Galerkin approach ((34)). Projections are performed by taking the canonical scalar product $\langle ., . \rangle$ defined by:

$$\langle f, g \rangle = \int_{-1}^{+1} f(y)g(y)\,\mathrm{d}y \,.$$

It turns out that things are simple only when restricting consistently to the lowest possible order, *i.e.* keeping only functions associated to U_0, W_0, U_1, V_1, and W_1, due to the parity properties of the functions involved that automatically guarantee the orthogonality of the different contributions to the velocity field.

Boundary conditions (2.7) suggest one to take ((34; 66)):

$$v' = V_1 A(1-y^2)^2\,, \tag{2.9}$$

and accordingly (2.8):

$$\{u', w'\} = \{U_0, W_0\}B(1-y^2) + \{U_1, W_1\}Cy(1-y^2)\,. \tag{2.10}$$

The pressure is expanded like $\{u', w'\}$, with two corresponding coefficients P_0 and P_1 that can be interpreted as the Lagrange multipliers introduced to fulfill the even and odd lowest order projections of (2.6). The normalization constants are given by: $A^2 = J_{0,4}^{-1} = 315/256$, $B^2 = J_{0,2}^{-1} = 15/16$, and $C^2 = J_{2,2}^{-1} = 105/16$. Amplitudes introduced in (2.9,2.10) are all functions of x, z, and t. The drift-flow component (U_0, W_0) has a plane Poiseuille profile, in close correspondence with what happens in the Rayleigh-Bénard case, as noticed first by (93) and subsequently exploited to derive the generalized Swift–Hohenberg model described in (66).

According to the Galerkin method prescriptions, we insert the assumed expansions (2.9,2.10) in the continuity equation (2.6), then we multiply it by $B(1-y^2)$ and integrate over the gap, which extracts its even part:

$$\partial_x U_0 + \partial_z W_0 = 0\,.$$

In the same way, multiplying (2.6) by $Cy(1-y^2)$, and integrating it extracts the odd part that reads:

$$\partial_x U_1 + \partial_z W_1 = \beta V_1\,,$$

with $\beta = \sqrt{3}$. Doing the appropriate manipulations for (2.3) and (2.5), we straightforwardly obtain the even parts as

$$\begin{aligned}
\partial_t U_0 + N_{U_0} &= -\partial_x P_0 - a_1 U_\mathrm{b}\partial_x U_1 - a_2 U_\mathrm{b} V_1 \\
&\quad + R^{-1}\left(\Delta_2 - \gamma_0\right) U_0\,, \qquad (2.11)\\
\partial_t W_0 + N_{W_0} &= -\partial_z P_0 - a_1 U_\mathrm{b}\partial_x W_1 \\
&\quad + R^{-1}(\Delta_2 - \gamma_0) W_0\,, \qquad (2.12)
\end{aligned}$$

with $\gamma_0 = \frac{5}{2}$, $a_1 = 1/\sqrt{7}$, $a_2 = 3\sqrt{3}/2\sqrt{7}$, $U_\mathrm{b} = 1$ and

$$\begin{aligned}
N_{U_0} &= \alpha_2\beta' U_1 V_1 - \alpha_3 V_1\partial_x V_1 + \alpha_1 W_0(\partial_z U_0 - \partial_x W_0) \\
&+ \alpha_2 W_1(\partial_z U_1 - \partial_x W_1) + \partial_x E_a,\\
N_{W_0} &= \alpha_2\beta' V_1 W_1 - \alpha_3 V_1\partial_z V_1 + \alpha_1 U_0(\partial_x W_0 - \partial_z U_0) \\
&+ \alpha_2 U_1(\partial_x W_1 - \partial_z U_1) + \partial_z E_a,
\end{aligned}$$

with $\alpha_1 = 3\sqrt{15}/14$, $\alpha_2 = \sqrt{15}/6$, and $\alpha_3 = 5\sqrt{15}/22$, $\beta' = 3\beta/2$ and $E_a = \frac{1}{2}(\alpha_1(U_0^2 + W_0^2) + \alpha_2(U_1^2 + W_1^2) + \alpha_3 V_1^2)$. In the same way, the odd part of (2.3)

and (2.5) read:

$$\begin{aligned} \partial_t U_1 + N_{U_1} &= -\partial_x P_1 - a_1 U_\mathrm{b} \partial_x U_0 \\ &\quad + R^{-1}(\Delta_2 - \gamma_1) U_1 \,, \qquad (2.13) \\ \partial_t W_1 + N_{W_1} &= -\partial_z P_1 - a_1 U_\mathrm{b} \partial_x W_0 \\ &\quad + R^{-1} \left(\Delta_2 - \gamma_1\right) W_1 \,, \qquad (2.14) \end{aligned}$$

with

$$\begin{aligned} N_{U_1} &= -\alpha_2 \beta'' U_0 V_1 + \alpha_2 W_1 (\partial_z U_0 - \partial_x W_0) + \alpha_2 W_0 (\partial_z U_1 - \partial_x W_1) + \partial_x E_b, \\ N_{W_1} &= -\alpha_2 \beta'' V_1 W_0 + \alpha_2 U_1 (\partial_x W_0 - \partial_z U_0) + \alpha_2 U_0 (\partial_x W_1 - \partial_z U_1) + \partial_z E_b, \end{aligned}$$

with $\gamma_1 = \frac{21}{2}$, $\beta'' = \beta/2$ and $E_b = \alpha_2(U_0 U_1 + W_0 W_1)$. Finally, the projection over V_1 gives us:

$$\partial_t V_1 + N_{V_1} = -\beta P_1 + R^{-1}(\Delta_2 - \beta^2) V_1, \qquad (2.15)$$

with:

$$N_{V_1} = \alpha_3 (W_0 \partial_z V_1 + U_0 \partial_x V_1) - (\alpha_2 \beta)(U_0 U_1 + W_0 W_1) + \beta E_b,$$

and $\alpha_2 \beta = \sqrt{5}/2$.

To eliminate the pressure P_0 and P_1 in Eq. (2.11-2.12) and Eq. (2.13-2.15), we introduce stream functions $(\Psi_0(x,z,t), \Psi_1(x,z,t))$ and velocity potential $\Phi_1(x,z,t)$ that satisfy the two continuity equations:

$$U_0 = -\partial_z \Psi_0, \quad W_0 = \partial_x \Psi_0, \qquad (2.16)$$

$$U_1 = \partial_x \Phi_1 - \partial_z \Psi_1, \quad W_1 = \partial_z \Phi_1 + \partial_x \Psi_1 \qquad (2.17)$$

$$\text{and } \beta V_1 = \Delta_2 \Phi_1. \qquad (2.18)$$

The velocity U_1 has two components, $U_1^p = \partial_x \Phi_1$ and $U_1^r = -\partial_z \Psi_1$, where "p"' ("r") denotes potential ("rotational") component (as well as W_1). By contrast, the velocity U_0 has only one rotational component (as well as W_0).

The equations governing Ψ_0 (Ψ_1) are obviously obtained by cross-differentiating and subtracting the equations for the velocity components (2.11-2.12) ((2.13-2.14)) (the rotational part). Taking the divergence of the equations (2.13-2.14) yields an equation for the pressure which is next used with (2.15) to determine the potential part of the velocity field accounted for by the field Φ_1. These equations are:

$$\begin{aligned} &(\partial_t - R^{-1}(\Delta_2 - \gamma_0))\Delta_2 \Psi_0 = (\partial_z N_{U_0} - \partial_x N_{W_0}) \\ &+ a_1 (\tfrac{3}{2} U_\mathrm{b} \partial_z \Delta_2 \Phi_1 - U_\mathrm{b} \partial_x \Delta_2 \Psi_1) \,, \qquad (2.19) \\ &(\partial_t - R^{-1}(\Delta_2 - \gamma_1))\Delta_2 \Psi_1 = (\partial_z N_{U_1} - \partial_x N_{W_1}) - a_1 U_\mathrm{b} \partial_x \Delta_2 \Psi_0 \,, \qquad (2.20) \\ &(\partial_t - R^{-1}(\Delta_2 - \beta^2))(\Delta_2 - \beta^2)\Delta_2 \Phi_1 = \beta^2 (\partial_x N_{U_1} + \partial_z N_{W_1}) \\ &+ \tfrac{45}{2} R^{-1} \Delta_2 \Phi_1 - \beta \Delta_2 N_{V_1}. \qquad (2.21) \end{aligned}$$

The linear term $-a_1 U_\mathrm{b} \partial_x \Delta_2 \Psi_0$ in Eq. 4.6 comes by cross-differentiating the two linear terms $-a_1 U_\mathrm{b} \partial_x U_0$ and $-a_1 U_\mathrm{b} \partial_x W_0$ in Eq. 2.13 and Eq. 2.14. In the same manner, the linear term $a_1(\frac{3}{2} U_\mathrm{b} \partial_z \Delta_2 \Phi_1 - U_\mathrm{b} \partial_x \Delta_2 \Psi_1)$ in Eq. 4.5 comes from $-a_1 U_\mathrm{b} \partial_x U_1 - a_2 U_\mathrm{b} V_1$ and $-a_1 U_\mathrm{b} \partial_x W_1$ in Eq. 2.11 and Eq. 2.12.

Note finally that the nonlinear terms can be written by developing the quantity E_a and E_b:

$$
\begin{aligned}
N_{U_0} &= \alpha_1(U_0 \partial_x U_0 + W_0 \partial_z U_0) + \alpha_2(U_1 \partial_x U_1 + W_1 \partial_z U_1 + \beta' V_1 U_1)\,, && (2.22)\\
N_{W_0} &= \alpha_1(U_0 \partial_x W_0 + W_0 \partial_z W_0) + \alpha_2(U_1 \partial_x W_1 + W_1 \partial_z W_1 + \beta' V_1 W_1) && (2.23)\\
N_{U_1} &= \alpha_2(U_0 \partial_x U_1 + U_1 \partial_x U_0 + W_0 \partial_z U_1 + W_1 \partial_z U_0 - \beta'' V_1 U_0)\,, && (2.24)\\
N_{W_1} &= \alpha_2(U_0 \partial_x W_1 + U_1 \partial_x W_0 + W_0 \partial_z W_1 + W_1 \partial_z W_0 - \beta'' V_1 W_0)\,, && (2.25)\\
N_{V_1} &= \alpha_3(U_0 \partial_x V_1 + W_0 \partial_z V_1)\,. && (2.26)
\end{aligned}
$$

The benefit of using the first formulation for the nonlinear terms is now clear: The number of FFTs to be performed is roughly divided by two, since only the cross-derivatives of the velocity are computed ($\partial_z U_0$, $\partial_x W_1$, etc...).

On the other hand, the equation governing the mean value of the streamwise velocity component U_1, denoted by $\overline{U_1} = \int_D U_1 \, ds/D$ is easily obtained by averaging Eq. 2.13 over the periodic domain and using the continuity equations and reads:

$$\frac{d}{dt}\overline{U_1} = \alpha_2(\beta + \beta'')\overline{U_0 V_1} - \gamma_1 R^{-1}\overline{U_1}. \tag{2.27}$$

For the spanwise velocity component W_1, we have:

$$\frac{d}{dt}\overline{W_1} = \alpha_2(\beta + \beta'')\overline{W_0 V_1} - \gamma_1 R^{-1}\overline{W_1}. \tag{2.28}$$

The mean value of V_1 is governed by:

$$\frac{d}{dt}\overline{V_1} = -\beta\overline{P_1} - R^{-1}(\Delta_2 - \beta^2)\overline{V_1}. \tag{2.29}$$

The mean value of P_1 is chosen zero $\overline{P_1} = 0$ and hence $\overline{V_1}$ obviously cancels. Finally, the mean values of U_0 and W_0 are governed by the equations:

$$\frac{d}{dt}\overline{U_0} = \alpha_2(\beta - \beta')\overline{U_1 V_1} - \gamma_0 R^{-1}\overline{U_0}, \tag{2.30}$$

$$\frac{d}{dt}\overline{W_0} = \alpha_2(\beta - \beta')\overline{W_1 V_1} - \gamma_0 R^{-1}\overline{W_0}. \tag{2.31}$$

The average velocity components ($\overline{U_0}$, $\overline{U_1}$,...) have to receive a special treatment. They are computed in parallel by integrating Eq. 2.27-Eq. 2.31. This is further explained in the next chapter. In the following, we recall the models derived for the stress-free boundary condition and some related results (§2.3.3).

2.2.1 Reynolds stress $-U_0V_1$

The evolution equation for the disturbance kinetic energy is the Reynolds-Orr equation: $\frac{dE}{dt} = P - D$, where $E(t) = \frac{1}{2}\int_V (u'^2 + v'^2 + w'^2)\, dV$ and the two terms on the right-hand side represent the exchange of energy with the base flow $U = U_b y$ i.e. the production $P = -\int_V u'v'\partial_y U\, dv$ and energy dissipation D due to viscous effects. The velocity components (u', v', w') are the perturbations to the basic flow U, given by (Eq. 2.9-Eq. 2.10). After integrating over y, we have $P = -\int_{D_{x,z}} \chi U_0 V_1\, ds$, where χ is a positive constant.

One reason this equation is interesting is that the occurrence of the two events (U_0 negative, V_1 positive) or (U_0 positive, V_1 negative) produce positive Reynolds stress $-U_0V_1$ and hence are very significant events in the production of turbulence (in the literature, they are called Q_2 and Q_4 events, as seen in §1.4.2) .

The linear deformation of the base flow by a vertical velocity is the well known lift-up mechanism (or "effect") (see e.g.(88)). The generated streamwise velocity by this mechanism is called a streak. In our model, this mechanism is represented by the linear term $-a_2U_bV_1$ in the equation (2.11) and U_0 represents the streak.

It is clear that when the lift-up feeds energy into the system (i.e., V_1 generates U_0), we have positive Reynolds stress, $-U_0V_1 > 0$. The origin of this lift-up are the streamwise vortices, which justifies their dominant role in turbulence production. The central issue addressed in the chapter IV concerns the generation of the streamwise vortices.

2.3 Free-slip model

2.3.1 Derivation

Models for the stress-free boundary condition have been introduced and used in (60) and in (64). We recall here the main steps of their derivation, just in order to compare the structure of the model, obtained by the lowest order truncation, to that of the no-slip model, both qualitatively (nature of the terms) and quantitatively (value of coefficients).

Stress-free conditions on the cross-stream velocity (v') read: $v'(y = \pm 1) = \partial_{yy}v'(y = \pm 1) = 0$, which directly leads one to take:

$$v' = \sum_{k\geq 1} V_{2k-1}\cos((2k-1)\beta y) + V_{2k}\sin(2k\beta y)\,, \tag{2.32}$$

with $\beta = \pi/2$. For the in-plane components (u', w'), from the continuity equation (2.6) one obtains $\partial_y u'(y = \pm 1) = \partial_y w'(y = \pm 1) = 0$, so that the corresponding

expansion reads:

$$\begin{aligned}\{u', w'\} &= \tfrac{1}{\sqrt{2}}\{U_0, W_0\} \\ &\quad + \sum_{k\geq 1}\{U_{2k-1}, W_{2k-1}\}\sin((2k-1)\beta y) \\ &\quad + \{U_{2k}, W_{2k}\}\cos(2k\beta y),\end{aligned} \tag{2.33}$$

As for the no-slip model, the pressure perturbation expands in the same way as the in-plane velocity perturbations. All the expansion coefficients remain functions of the space coordinates (x, z) and time (t). These expansions are compatible with a bulk force taken in the form $\mathbf{f} = F\sin(\beta y/h)\hat{\mathbf{x}}$ added to the right hand side of Eq. 2.1 and generating a basic profile $U(y) = U_\mathrm{p}\sin(\beta y/h)$, provided that $F = U_\mathrm{p}\nu\beta^2/h^2$. As before, the Reynolds number is taken as $R = U_\mathrm{p}h/\nu$ but, in contrast with the no-slip case, there remains some arbitrary in its definition. If we stick to our definition of U_p as the speed at $y = 1$, given ν, R is numerically equal to $1/\nu$ but other conventions exist, *e.g.* take the reference velocity as $U(y = 1/2)$ or define R from the root-mean-square shear rate of the sine profile as in (103).

It is clear that the trigonometric basis is closed for multiplications and differentiation with respect to y, which makes the Galerkin projection particularly straightforward. It suffices to substitute expansions (2.32,2.33) in equations (2.3–2.6), to compute the derivatives, expand the products, and isolate the different harmonics, one after the other. In (60) this modeling approach has been shown to preserve both the conservation of the perturbation energy by advection terms, a feature of Navier–Stokes equations, and the linear stability of the basic flow for all Reynolds numbers, a property of pCf (as already shown by Tollmien, the sine profile lacks inertial instability in spite of the presence of an inflection point, see *e.g.* (26).)

From the continuity equation (2.6), one immediately gets:

$$\partial_x U_k + \partial_z W_k + k\beta(-1)^k V_k = 0, \quad \forall k \geq 1. \tag{2.34}$$

which, for $k = 0$ and $k = 1$ yields:

$$\partial_x U_0 + \partial_z W_0 = 0, \quad \partial_x U_1 + \partial_z W_1 = \beta V_1. \tag{2.35}$$

The lowest order truncation (beyond $k_\mathrm{max} = 1$) gives the free-slip model with the three fields Ψ_0, Ψ_1 and Φ_1 and is called $3\mathcal{F}$ model ($\mathcal{F}$ for field) . Its structure is similar to the no-slip model (§2.2). Hence, for the sake of simplicity, only the values of the coefficients for this model are given here in Table. 2.1. Only the full expression of the next case $k_\mathrm{max} = 2$ ($5\mathcal{F}$ model) is given, but models with k_max up to 4 have been explicitly derived and used in numerical simulations ($9\mathcal{F}$ model).

We give now the equations governing the amplitudes (U_0, W_0), (U_1, V_1, W_1), and (U_2, V_2, W_2) of the $5\mathcal{F}$ model. From the projection of the continuity equation

(2.34) we have:

$$\partial_x U_0 + \partial_z W_0 = 0, \quad \partial_x U_1 + \partial_z W_1 = \beta V_1, \quad \partial_x U_2 + \partial_z W_2 = -2\beta V_2.$$

Then, the projection of the perturbation equations gives for U_0 and W_0:

$$\begin{aligned} \partial_t U_0 + N_{U_0} &= -\partial_x P_0 - \tfrac{1}{\sqrt{2}} U_\mathrm{b} \partial_x U_1 - \tfrac{1}{\sqrt{2}} \beta U_\mathrm{b} V_1 + R^{-1} \Delta_2 U_0 \,, \\ \partial_t W_0 + N_{W_0} &= -\partial_z P_0 - \tfrac{1}{\sqrt{2}} U_\mathrm{b} \partial_x W_1 + R^{-1} \Delta_2 W_0 \,, \end{aligned}$$

where the nonlinear terms are:

$$\begin{aligned} N_{U_0} &= \tfrac{1}{\sqrt{2}} \big(U_0 \partial_x U_0 + W_0 \partial_z U_0 + U_1 \partial_x U_1 + \beta V_1 U_1 + W_1 \partial_z U_1 \\ &\quad + U_2 \partial_x U_2 - 2\beta V_2 U_2 + W_2 \partial_z U_2 \big) \,, \\ N_{W_0} &= \tfrac{1}{\sqrt{2}} \big(U_0 \partial_x W_0 + W_0 \partial_z W_0 + U_1 \partial_x W_1 + \beta V_1 W_1 + W_1 \partial_z W_1 \\ &\quad + U_2 \partial_x W_2 - 2\beta V_2 W_2 + W_2 \partial_z W_2 \big) \,. \end{aligned}$$

Next, for U_1, W_1 and V_1 we have:

$$\begin{aligned} \partial_t U_1 + N_{U_1} &= -\partial_x P_1 - \tfrac{1}{\sqrt{2}} U_\mathrm{b} \partial_x U_0 + \tfrac{1}{2} U_\mathrm{b} \partial_x U_2 - \tfrac{1}{2} \beta U_\mathrm{b} V_2 + R^{-1} (\Delta_2 - \beta^2) U_1 \,, \\ \partial_t W_1 + N_{W_1} &= -\partial_z P_1 - \tfrac{1}{\sqrt{2}} U_\mathrm{b} \partial_x W_0 + \tfrac{1}{2} U_\mathrm{b} \partial_x W_2 + R^{-1} (\Delta_2 - \beta^2) W_1 \,, \\ \partial_t V_1 + N_{V_1} &= -\beta P_1 - \tfrac{1}{2} U_\mathrm{b} \partial_x V_2 + R^{-1} (\Delta_2 - \beta^2) V_1 \,, \end{aligned}$$

with:

$$\begin{aligned} N_{U_1} &= \tfrac{1}{\sqrt{2}} (U_0 \partial_x U_1 + W_0 \partial_z U_1 + U_1 \partial_x U_0 + W_1 \partial_z U_0) - \tfrac{1}{2} (U_1 \partial_x U_2 + 2\beta V_1 U_2 + W_1 \partial_z U_2) \\ &\quad - \tfrac{1}{2} (U_2 \partial_x U_1 - \beta V_2 U_1 + W_2 \partial_z U_1) \,, \\ N_{W_1} &= \tfrac{1}{\sqrt{2}} (U_0 \partial_x W_1 + W_0 \partial_z W_1 + U_1 \partial_x W_0 + W_1 \partial_z W_0) - \tfrac{1}{2} (U_1 \partial_x W_2 + 2\beta V_1 W_2 + W_1 \partial_z W_2) \\ &\quad - \tfrac{1}{2} (U_2 \partial_x W_1 - \beta V_2 W_1 + W_2 \partial_z W_1) \,, \\ N_{V_1} &= \tfrac{1}{\sqrt{2}} (U_0 \partial_x V_1 + W_0 \partial_z V_1) + \tfrac{1}{2} \big(U_1 \partial_x V_2 + U_2 \partial_x V_1 + \beta V_1 V_2 + W_1 \partial_z V_2 + W_2 \partial_z V_1 \big) \,. \end{aligned}$$

Finally, for the velocity components U_2, W_2 and V_2, we have:

$$\begin{aligned} \partial_t U_2 + N_{U_2} &= -\partial_x P_2 + \tfrac{1}{2} U_\mathrm{b} \partial_x U_1 - \tfrac{1}{2} \beta U_\mathrm{b} V_1 + R^{-1} (\Delta_2 - 4\beta^2) U_2 \,, \quad (2.36) \\ \partial_t W_2 + N_{W_2} &= -\partial_z P_2 + \tfrac{1}{2} U_\mathrm{b} \partial_x W_1 + R^{-1} (\Delta_2 - 4\beta^2) W_2 \,, \\ \partial_t V_2 + N_{V_2} &= 2\beta P_2 - \tfrac{1}{2} U_\mathrm{b} \partial_x V_1 + R^{-1} (\Delta_2 - 4\beta^2) V_2 \,, \end{aligned}$$

where the nonlinear terms are:

$$\begin{aligned} N_{U_2} &= \tfrac{1}{\sqrt{2}} (U_0 \partial_x U_2 + W_0 \partial_z U_2 + U_2 \partial_x U_0 + W_2 \partial_z U_0) - \tfrac{1}{2} (U_1 \partial_x U_1 - \beta V_1 U_1 + W_1 \partial_z U_1) \,, \\ N_{W_2} &= \tfrac{1}{\sqrt{2}} (U_0 \partial_x W_2 + W_0 \partial_z W_2 + U_2 \partial_x W_0 + W_2 \partial_z W_0) - \tfrac{1}{2} (U_1 \partial_x W_1 - \beta V_1 W_1 + W_1 \partial_z W_1) \,, \\ N_{V_2} &= \tfrac{1}{\sqrt{2}} (U_0 \partial_x V_2 + W_0 \partial_z V_2) + \tfrac{1}{2} (U_1 \partial_x V_1 - \beta V_1 V_1 + W_1 \partial_z V_1) \,. \end{aligned}$$

As usually, the pressure amplitudes (P_0, P_1, P_2) are eliminated by introducing the five fields Ψ_0, (Ψ_1, Φ_1) and (Ψ_2, Φ_2).

Table 2.1: The coefficients for the no-slip and $3\mathcal{F}$ free-slip models.

Coef.	β'	β''	a_1	a_2	α_1	α_2	α_3	γ_0	γ_1
free-slip	$\pi/2$	0	$1/\sqrt{2}$	$\pi/(2\sqrt{2})$	$1/\sqrt{2}$	$1/\sqrt{2}$	$1/\sqrt{2}$	0	$\pi^2/4$
no-slip	$3\sqrt{3}/2$	$\sqrt{3}/2$	$1/\sqrt{7}$	$3\sqrt{3}/(2\sqrt{7})$	$3\sqrt{15}/\sqrt{14}$	$\sqrt{15}/6$	$5\sqrt{15}/22$	5/2	21/2

2.3.2 Formal comparison of the models

Since the no-slip and $3\mathcal{F}$ free-slip models have remarkably similar structures, with comparable coefficients (Table 2.1), it is interesting to point out more quantitatively similarities and differences. As far as non-normal effects and nonlinear interactions are concerned, one may think that the two models are close to each other and that the dynamics they generate will be robust (the role of the differences can however be studied in detail to elucidate specific points).

First of all, it is clear that the quantity $\sqrt{3}$ in (2.35), which measures the typical order of magnitude of gradients in the wall-normal direction, plays exactly the same role as β in the second equation of (2.35) and has a comparable order of magnitude, since $\sqrt{3} \approx 1.732$ is not so different from $\pi/2 \approx 1.571$.

The most important difference between the two models is then observed when considering the viscous terms. Whereas in the stress-free model, the drift velocity component $\{U_0, W_0\}$ can relax only through in-plane modulations *via* the terms involving Δ_2 in (2.11,2.12) since ($\gamma_0 = 0$), an additional damping is observed in the no-slip case with coefficient $\gamma_0 = 5/2$ independent of the in-plane dependence of that flow component. In the same way the damping of components $\{U_1, W_1\}$ is much stronger in the no-slip case, coefficient $\gamma_1 = 21/2$ in (2.13,2.14), than in the stress-free case, coefficient $\beta^2 \approx 2.41$. These features show that one goes in the right direction (from stress-free to no-slip) since the stress-free model is known to underestimate thresholds by a large factor ((64)).

Another important feature of the no-slip model is that an (x, z)-independent component of U_1 can be created as the flow evolves, so that the model already contains a mean flow correction to the base profile $U(y) = U_{\rm b}y$ even when truncated at lowest order, whereas a similar correction formally appears only beyond $k = 3$ for the stress-free model, as stressed in (70).

2.3.3 Main results for the free-slip models

Both $3\mathcal{F}$ and $5\mathcal{F}$ free-slip models have been observed to display a globally subcritical transition to turbulence qualitatively similar to what is observed in laboratory experiments, though at unrealistic low Reynolds numbers, found to be around $R_{\rm g} \approx 38$. This anomalously low value (when compared to experimental results) is at least partly attributed to the unrealistic stress-free boundary conditions that artificially decrease the gradients and the associated dissipation, thus lowering

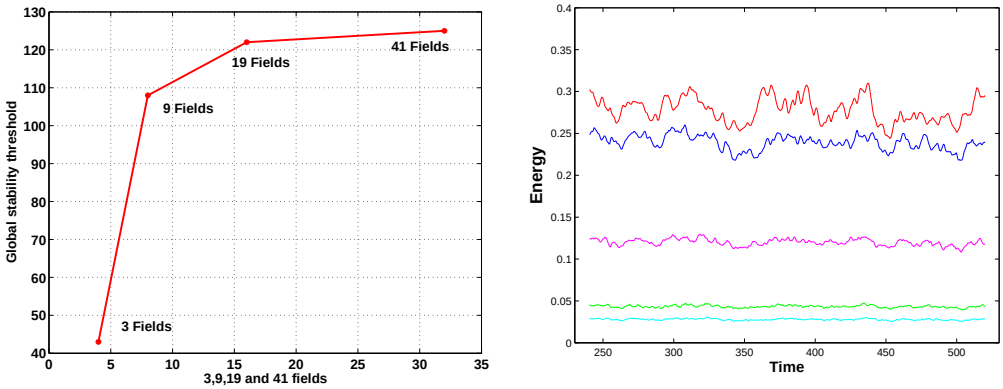

Figure 2.1: Left: The global stability threshold vs. number of modes ($k_{\max}$). Right: time evolution of the energies $\langle E_0\rangle$, $\langle E_1\rangle$, $\langle E_2\rangle$, $\langle E_3\rangle$ and $\langle E_4\rangle$ with the $9\mathcal{F}$ model for $R = 120$ and $L_x \times L_z = 64 \times 64$. Note that $\langle E_0\rangle \geq \langle E_1\rangle \geq \langle E_2\rangle \geq \langle E_3\rangle \geq \langle E_4\rangle$.

the thresholds, in exactly the same way as is convection. Also, the discrepancy in R is attributed to the low order of truncation since adding more functions in the expansion allows for a transfer of energy towards smaller cross-stream scales where it can be dissipated. Increasing the order of truncation by enhancing the y-resolution for the free-slip model is simple to do. But increasing the truncation order becomes rapidly tedious with our approach (i.e with fields equations). We used instead the full pseudo-spectral scheme developed by J. Schumacher (Phillipps Universität, Marburg) with the same stress-free boundary conditions and external forcing. The lowest truncation gives the same results as with our model, while the threshold saturates around $R_{\rm g} \approx 125$ as the number of fields is increased, Fig. 2.1. In the other hand, we have observed that the energy contained in the mode k, $E_{\rm k} = \frac{1}{2}(U_k^2 + V_1^k + W_1^k)$ is greater than that contained in the mode $k+1$, as illustrated with the $9\mathcal{F}$ model ($k_{max} = 4$) in Fig. 2.1.

2.4 Conclusions

Modeling transitional pCf might provide heuristic explanations to be further tested in experiments either in the laboratory or in the computer. Most rational modeling approaches are developed through truncations of appropriate Galerkin expansions of the primitive equations. Such an approach was presented in this chapter for both no-slip and free-slip boundary conditions.

For the sake of conciseness, not all our simulation results for the stress-free models have been presented here. In fact, interesting things (e.g. growth of turbulent spots, etc...) happen in the models at unrealistically low values of R

whereas $R_g \sim 325$ in the laboratory experiments. As we have seen, this feature is not drastically changed by adding more fields to describe the cross stream dependence though an embryo of cascading transfer from modes k towards $k+1$, for which dissipation is more intense. This shows that the stress-free assumption plays the dominant role in the lowering of thresholds. This assumption is raised by turning to realistic no-slip boundary conditions, as we have done in §2.2. All the presented results in the forthcoming chapters, are obtained with the no-slip model.

Chapter 3

Numerical results

3.1 Introduction

In order to check the ability of our no-slip model to capture the essential features of the globally subcritical nature of the transition to turbulence of the plane Couette flow, numerical simulations have been performed. The study of the no-slip model in view of elucidating specific processes such as the propagation of turbulent domains is left to forthcoming chapters. In §3.2, we outline the numerical method used throughout all this manuscript. Some simulation results obtained with the no-slip model are then presented in section 3.3, illustrating the globally subcritical character of the spatio-temporal unfreezing of coherent structures assumed in previous low dimensional modeling approaches.

3.2 Numerical implementation

First of all, we recall the set of equations of the no-slip model to be solved:

$$(\partial_t - R^{-1}(\Delta_2 - \gamma_0))\Delta_2\Psi_0 = (\partial_z N_{U_0} - \partial_x N_{W_0}) \\ +a_1(\tfrac{3}{2}U_{\rm b}\partial_z\Delta_2\Phi_1 - U_{\rm b}\partial_x\Delta_2\Psi_1)\,, \tag{3.1}$$

$$(\partial_t - R^{-1}(\Delta_2 - \gamma_1))\Delta_2\Psi_1 = (\partial_z N_{U_1} - \partial_x N_{W_1}) - a_1 U_{\rm b}\partial_x\Delta_2\Psi_0\,, \tag{3.2}$$

$$(\partial_t - R^{-1}(\Delta_2 - \beta^2))(\Delta_2 - \beta^2)\Delta_2\Phi_1 = \beta^2(\partial_x N_{U_1} + \partial_z N_{W_1}) \\ +\tfrac{45}{2}R^{-1}\Delta_2\Phi_1 - \beta\Delta_2 N_{V_1}. \tag{3.3}$$

where the nonlinear terms are given in the previous chapter. The two equations (3.1,3.2) govern the in-plane fluid motion (the velocity components U_0, W_0 and the rotational components of U_1 and W_1). The third equation (3.3), governs the vertical velocity V_1 and the potential components of U_1 and W_1. The relations

between the velocity components and the three fields are:

$$U_0 = \widetilde{U}_0 - \partial_z \Psi_0, \quad W_0 = \widetilde{W}_0 + \partial_x \Psi_0, \tag{3.4}$$

$$U_1 = \widetilde{U}_1 + \partial_x \Phi_1 - \partial_z \Psi_1, \quad W_1 = \widetilde{W}_1 + \partial_z \Phi_1 + \partial_x \Psi_1, \tag{3.5}$$

$$\text{and } \beta V_1 = \Delta_2 \Phi_1. \tag{3.6}$$

Though not necessary on general grounds, the introduction of the additional quantities $\widetilde{U}_1, ...$ is forced by our choice of in-plane periodic boundary conditions for the fields Ψ_0, Ψ_1 and Φ_1. This is because these uniform components are generated by contributions to the correponding stream-function and potential that would vary linearly with x and z, a space dependence that is precluded by their representations as truncated Fourier series expansions inherent in our computational approach that we present now.

3.2.1 Numerical scheme

The governing equations of Ψ_0, Ψ_1 and Φ_1 can be taken in the form:

$$\partial_t v = \mathcal{L} v + \mathcal{N}(v)\,, \tag{3.7}$$

where $\mathcal{L}$ is a linear part that can be integrated exactly and $\mathcal{N}$ some nonlinear part. Then, we rewrite (3.7) as

$$\partial_t \left[\exp(-\mathcal{L}t)v\right] = \exp(-i\mathcal{L}t)\left[\partial_t v - \mathcal{L}v\right] = \exp(-i\mathcal{L}t)\mathcal{N}(v)\,. \tag{3.8}$$

or setting $u = \exp(-\mathcal{L}t)v$ and $\mathcal{M}(v) = \exp(-\mathcal{L}t)\mathcal{N}(v)$:

$$\partial_t u = \mathcal{M}(v)\,. \tag{3.9}$$

This is integrated by a standard second order Adams–Bashforth scheme, which yields

$$u_{n+1} = u_n + \tau\left[\tfrac{3}{2}\mathcal{M}_n - \tfrac{1}{2}\mathcal{M}_{n-1}\right] \tag{3.10}$$

or returning to v and $\mathcal{N}$, after appropriate simplification which, reads:

$$v_{n+1} = \exp(\mathcal{L}\tau)v_n + \tau\exp(\mathcal{L}\tau)\left[\tfrac{3}{2}\mathcal{N}_n - \tfrac{1}{2}\exp(\mathcal{L}\tau)\mathcal{N}_{n-1}\right]\,. \tag{3.11}$$

With this expression truncation errors are of order τ^3 and it is essential to include the weighting factors $\exp(\mathcal{L}\tau)$, since otherwise for small τ one gets $\exp(\mathcal{L}\tau) = 1 + \mathcal{L}\tau + \mathcal{O}(\tau^2)$ and when using $\frac{3}{2}\mathcal{N}_n - \frac{1}{2}\mathcal{N}_{n-1}$ instead of expression on the r.h.s. of (3.11), one makes an error which is of order $\mathcal{O}(\tau^2)$, i.e. the accuracy of the computation is one order lower than believed (the difference is $\left[\frac{3}{2}\mathcal{N}_n - \mathcal{N}_{n-1}\right]\tau^2 \approx \frac{1}{2}N_n\tau^2$ since $\mathcal{N}_n = \mathcal{N}_{n-1} + \mathcal{O}(\tau)$. The first step is computed by a backward Euler scheme.

The space integration was done using standard Fourier pseudo-spectral method with periodic boundary conditions in the streamwise and spanwise direction. This allows us to develop a standard Fourier pseudo-spectral numerical scheme solving the diagonal viscous terms in spectral space and integrating them exactly. The nonlinear terms and the linear non-normal terms are evaluated in physical space and integrated in time using a second order Adams–Bashford scheme. Fast Fourier transforms (FFTs) are used to pass from spectral to physical space and *vice versa*. In the next section, we present our numerical code.

3.2.2 The algorithm and numerical validations

Here is the algorithm:

- Input: Initial condition (Ψ_0, Ψ_1, Φ_1) and mean values of the velocities $(\widetilde{U}_1...)$.
- Iteration: To compute the velocities at t_{n+1}:
  - Compute the velocities from Ψ_0, Ψ_1, Φ_1 and correcting the mean value using the quantities $(\widetilde{U}_1...)$ at t_n (i.e., using Eq. (3.4-3.6))
  - Compute the nonlinearities and all the r.h.s of the fields equations (3.1-3.3) with those velocities.
  - Advancing in time (Adams-Basford) using the r.h.s at t_n and t_{n-1} $\rightsquigarrow$ we get the three fields at t_{n+1}.
  - Compute the r.h.s of the mean equation (Eq. 2.27-2.31) at t_n.
  - Advancing in time (Adams-Basford) using the r.h.s at t_n and at t_{n-1}. $\rightsquigarrow$ we get the mean values of the velocity components at t_{n+1}.
  - r.h.s at $t_{n-1} \leftarrow$ r.h.s at t_n.
- Ouput: The three fields (Ψ_0, Ψ_1, Φ_1) and the velocity components.

The code was tested and verified in four ways: (i) In Figure 3.1, we verified the order of the numerical scheme by computing the L_∞ norm for the error, i.e., $max_\infty|E_{\text{tot}} - E_{\text{tot}}^{\text{exact}}|$ for different time steps, where $E_{\text{tot}}^{\text{exact}}$ is the energy obtained with the smallest time step ($dt = dt^0/2^6$ with $dt^0 = 0.01$) and considered, without loss of generality, as the "exact" solution (except for accumulation of round-off errors but negligible when using double precision). The quantity E_{tot} denotes energy obtained with larger time step. For a temporal scheme of order k, dividing the time step by 2 will divide the error by 2^k. Hence, by plotting the logarithm of L_∞ norm of the energy, i.e., $max_\infty|E_{\text{tot}} - E_{\text{tot}}^{\text{exact}}|$ versus the different time steps, we can determine the order of the scheme, i.e. $k = 2$ as indicated in Fig. 3.1. (ii) Then we confirmed energy conservation in the Eulerian case, where there is

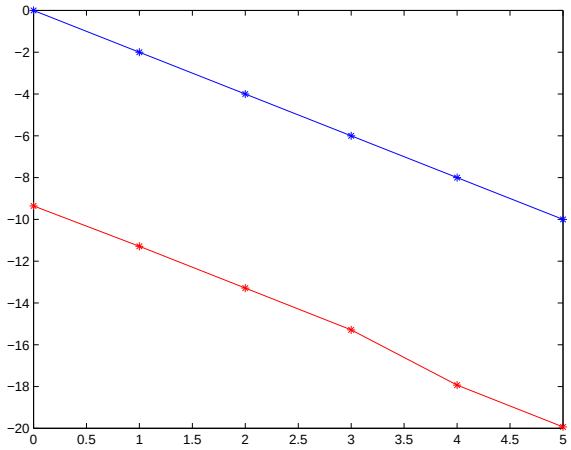

Figure 3.1: The temporal order of the scheme. The value of $max_\infty|E_{\text{tot}} - E_{\text{tot}}^{\text{exact}}|$ versus the different time steps in red line: the first point corresponds to $dt = dt^0 = 0.01$, the next point to $dt = dt^0/2^n$, $n = 1..5$ and $E_{\text{tot}}^{\text{exact}}$ is obtained with $dt = dt^0/2^6$. We plot in blue a curve with slope -2. The order of the scheme is hence $k = 2$ as expected.

no dissipation and no input of energy by the base flow. The fluctuation in the temporal mean value of the energy is less than 0.01% for $\Delta t = 200$, confirming that our numerical scheme conserves the energy. (iii) Next, we simulated the full system (i.e. with non-normal term and dissipative term). For a period of about $\Delta t = 10000$ and with different time steps δt from $\delta t \equiv \delta t^0 = 0.01$ to $\delta t = \delta t^0/1000$, the more important aspects of the dynamics as temporal mean value of the energy and the mean value of the base flow correction $\widetilde{U}_1$ did not change, even when using an Adams-Bashford method of third order. Therefore, all the simulations presented here were done with $\delta t = 0.01$ (and $\delta x = \delta z = 0.25$). For $2h = 0.7cm$, the viscosity of water $\nu = 0.01cm^2/s$ and a Reynolds number of $R = 200$, the time unit is $\tau = h/U_0 = h^2/(\nu R) = 0.5s$ and for $\Delta t = 10000$, this corresponds approximately to 10 min. (iv) Concerning the dynamics of the coherent structures (streaks, streamwise vortices...), we have to be sure that we obtain the same structures for different time and space steps. First, we simulated the growth of a turbulent spot with two different space steps, namely $\delta x = \delta z = 0.25$ and $\delta x = \delta z = 0.125$ with the same time step. In the second time, we simulated the evolution of a turbulent spot with two different time steps $\delta t = 0.01$ and $\delta t = 0.001$ and with the same space step. All those simulations give us the same coherent structures, which are investigated in the following chapters.

Finally, concerning the aliasing errors, we have found that for the Reynolds numbers that we are concerned with ($R \in [160, 200]$) and the space steps used here, all the aspects of the dynamics are unchanged when we apply the 3/2 rule to remove these errors. Hence, all the presented results are obtained with no-unaliased simulations. These simulations were performed in boxes with sizes ranging from $L_x \times L_z = 16 \times 16$ up to $L_x \times L_z = 256 \times 256$. With $\delta x = \delta z = 0.25$ and $L_x = L_z = 128$, we need 512 Fourier modes in each direction. The numerical integration over a time interval of 200 time units needs on the NEC-SX 5 supercomputer at the IDRIS 900 sec-CPU time and about one day on a PC station. Using a smaller box, i.e., $L_x = 128$ and $L_z = 64$, which corresponds to 256 Fourier modes in the spanwise direction, this integration takes about 450 sec-CPU time.

3.3 Results

3.3.1 Global sub-criticality

Global sub-criticality of the model is depicted in Fig. 3.2 which displays the behavior of the average turbulent energy per unit surface as a function of the Reynolds number R. For $R > R_g \approx 173$, spontaneous collapse of the uniformly turbulent state is never observed, even when pursuing the simulation for durations so long that, for all practical purposes, one can safely claim that turbulence is sustained. On the other hand, below ≈ 172, the laminar state is always obtained but at the end of turbulent transients of variable durations. A series of such transients is illustrated in Fig. 3.2 for $R = 170$. It can be seen that they end quite abruptly so that it makes sense to define a conditional average turbulent energy restricted to the plateau value, before final decay. Such conditional averages are indicated by stars in Fig. 3.2 while squares denote averages corresponding to sustained turbulent regimes. The amplitude of the fluctuations of the turbulent energy per unit surface in the sustained regime is indicated by an arrow-headed bar at $R = 200$. This amplitude is comparatively large only because the size of the domain has been chosen not so large.

3.3.2 Extensivity of the sustained turbulent regime

It has been argued by (67) that the low-dimensional modeling in terms of ordinary differential equations that stems from the MFU hypothesis may give valuable hints only about the mechanisms of turbulence sustainment well beyond the transitional regime but not necessarily about the transitional regime itself where space-time behavior is involved. Indeed the MFU hypothesis freezes the space dependence of the perturbations and introduces phase-space resonances at the origin of the fractal properties of chaotic transients involved in the decay of tur-

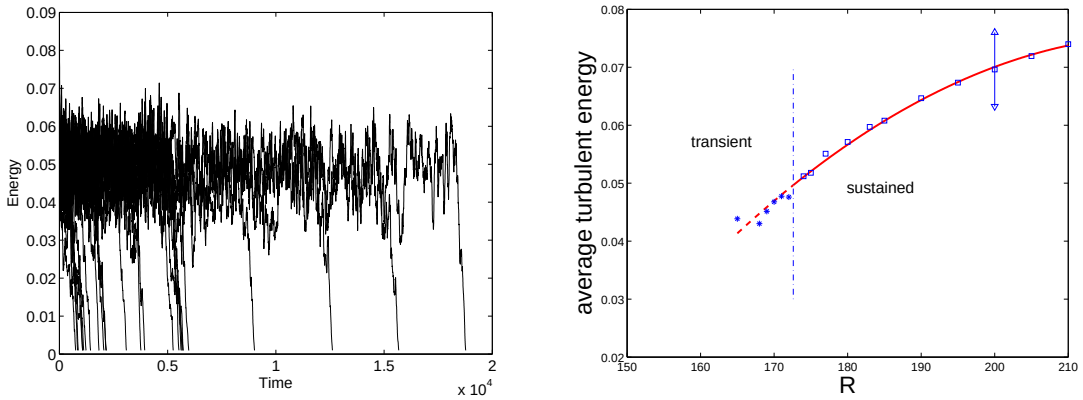

Figure 3.2: Left: Total perturbation energy E_{tot} as a function of time in a series of transients from a turbulent flow prepared at $R_{\mathrm{i}} = 200$ suddenly quenched at $R_{\mathrm{f}} = 170$. Right: Variation of the average turbulent energy with R. Evidence of a global stability threshold $R_{\mathrm{g}} \approx 173$. Values corresponding to squares $R > R_g$ correspond to sustained regimes, those corresponding to transients are marked with asterisks. The double-arrowed bar at $R = 200$ indicates the order of magnitude of the fluctuation of the turbulent energy around its means. The computational domain is $L_x \times L_z = 32 \times 32$.

bulence, but all that remains extremely sensitive to the physical size of the MFU. By nature, the hypothesis is thus unable to deal with growth or decay of turbulence through the coexistence of laminar and turbulent domains that fluctuate in space and time. Considering this specific problem, it seems legitimate to require that, to be appropriate, a model should display some kind of statistical robustness when the size of the simulation domain is varied. This point was stressed by (82), shown to hold for the Kuramoto-Sivasinsky model of space-time chaos ((65)), and judged important in the ergodic theory of chaotic extended systems ((30)). As an indication that our model behaves appropriately is obtained by considering the total perturbation energy per unit surface and its fluctuations as the surface of the simulation domain is increased. Table 3.1 displays our results. A series of experiments over domain was performed, with domain surfaces starting from 16×8 to 128×128 and for $R = 200$.

For smallest system, turbulence was only transient for that value of R. Sustained turbulence was obtained but at much larger values. This is not surprising since much dissipation is associated with the in-plane space dependence forced by periodic boundary conditions, raising the thresholds for complex behavior accordingly. That behavior is however better understood as temporal chaos since the domain can only fit a very small number of structures, and the transient possibly better analyzed in terms of chaotic saddles (29).

Our results for values of $L_x \times L_z$ beyond 16×16 clearly shows that the turbulent

Table 3.1: Total perturbation energy: time average and fluctuations for $R = 200$.

$L_x \times L_z$	16×8	16×16	32×16	32×32	64×32	64×64	128×64	128×128
$E_{\rm tot}$	0.06501	0.0690	0.0691	0.0696	0.0700	0.0697	0.06959	0.06948
$\sigma_{E_{\rm tot}}$	0.01510	0.0105	0.0078	0.0055	0.0038	0.0026	0.00175	0.00118

regime is extensive. Evidence of it is obtained from (i) the time average of $E_{\rm tot}$ which is independent of the size and (ii) the fluctuations around this average value which decrease roughly as the inverse square root of the size.

3.3.3 Transient lifetimes

The global stability threshold $R_{\rm g}$ is best defined as the value of the control parameter beyond which the non trivial state, here the turbulent regime, is unstable and thus cannot be sustained in the long term. Accordingly, the trivial state here, the laminar flow, is the only possible equilibrium solution, whatever the initial configuration. For globally sub-critical extended systems such as the pCf, many studies have been devoted to the transition from laminar to turbulent flow, either under the effect of natural fluctuations, upon triggering specific localized perturbations, or upon modifying the base flow in a well-controlled way (see the review in (63)). Theses studies do not allow the determination of $R_{\rm g}$ in a straightforward way since, in such experiments, the turbulent state is reached with finite probability only due to the local stability of the base flow, thus explaining the dispersion of results in early studies and some sensitivity to the triggering process. By contrast, from the very definition of $R_{\rm g}$, observing relaxation from a typical turbulent state prepared at some initial $R = R_{\rm i} > R_{\rm g}$ down to lower $R_{\rm f} < R_{\rm g}$ yields $R_{\rm g}$ without ambiguity. Such quench experiments have produced the value $R_g \approx 323$ mentioned earlier for pCf in the laboratory. The cumulative distribution of duration's of turbulent transients was studied and could be fitted against exponential laws in the form $\Pi(\tau_{\rm tr}) \propto exp(-\tau/\langle\tau_{\rm tr}\rangle)$, where $\Pi(\tau_{\rm tr} > \tau)$ is the probability to observe a transient with duration $\tau_{\rm tr}$ larger than some given τ. In this expression $\langle\tau_{\rm tr}\rangle$ defined as the mean transient duration, is the characteristic decay time of the distribution, provided it is effectively exponential. In (11) and (12), that quantity was shown to diverge to infinity as $R_{\rm f}$ approached $R_{\rm g}$ from below as $\langle\tau_{\rm tr}\rangle \approx (R_{\rm g} - R_{\rm f})^{-1}$. This behavior was recently questioned by (45) and the proposition was made of an indefinitely exponentially increasing decay time instead of a critical behavior of the decay time at some finite value $R_{\rm g}$. This reservation was made on the basis of specific observations for Poiseuille pipe flow. As we show below, quench experiments using our no-slip model can be seen to behave according to $\langle\tau_{\rm tr}\rangle \approx (R_{\rm g} - R_{\rm f})^{-1}$ with the same degree of confidence.

Experiments were performed by quenching the system from some initial turbulent state at $R = R_{\rm i} = 200$. The Reynolds number was next suddenly decreased

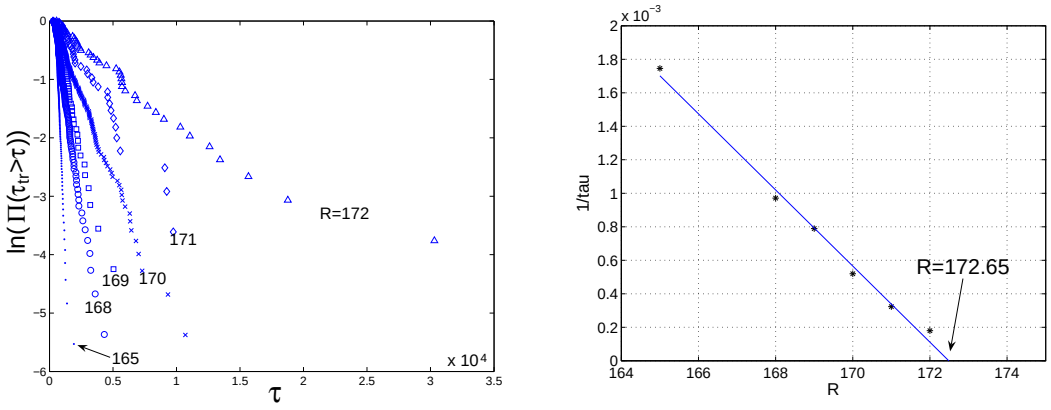

Figure 3.3: Left: Distribution of transient durations in quench experiments with $R_\mathrm{i} = 200$ and different R_f in semi-log plot. Right: Inverse of the mean transient duration as a function of a quench value $R = R_\mathrm{f} < R_\mathrm{g} \approx 172.65$ as found by extrapolation.

to a final value $R = R_\mathrm{f}$. The size was reduced as much as possible in order to be able to perform statistics over a large number of independent trials. It was however kept sufficiently large to remain well within the range where extensivity is expected. In practice we took $L_x = L_z = 32$.

The durations of individual transients were determined as the time needed to reach some cut-off value of the total specific perturbation energy below which the system immediately and irreversibly decays to the laminar state. Fig. 3.3 displays a typical set of experiments to be analyzed. The statistics were checked to be insensitive to the precise value chosen for the cut-off.

Below $R = 173$, transients of different durations began to appear and well-defined distributions of durations were seen to develop, while relaxation could be considered as "immediate" below $R = R_\mathrm{u} \approx 164$ (notation introduced in (11)). Focusing rather on the approach of $R_\mathrm{g} \approx 173$ from below, using lin-log scales Figure 3.3 shows that the statistics of turbulent transients' durations are indeed exponentially decreasing and that the slope decreases as R_f increases. For each Reynolds number, we have gathered about 200 transients. The decay rate characterizing the distribution Π can be determined from the inverse of the average of the durations measured at given R_f since the exponential behavior apparently extends down to the shortest durations. Otherwise it could be estimated by fitting the tails of the cumulated distributions functions against exponentials. Expecting that the mean decay time $\langle \tau_\mathrm{tr} \rangle$ diverges as $(R_\mathrm{g} - R)^\xi$ as R_f approaches R_g from below, we have plotted $1/\langle \tau_\mathrm{tr} \rangle^{1/\xi}$ against $R = R_\mathrm{f}$ for different values of ξ. As seen in Fig. 3.3, trial and error nicely supports the value of $\xi = 1$ that corresponds to experimental observations (11). The mean decay rate extrapolates to zero at $R_\mathrm{g} \approx 172.65$, which us thus the global stability threshold for our model.

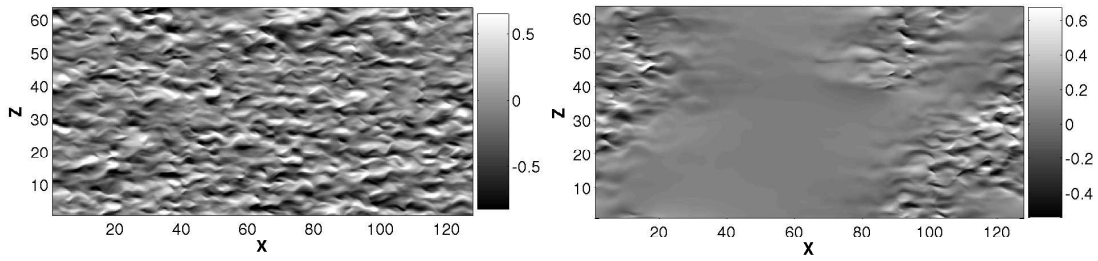

Figure 3.4: During the transient decay, pockets of laminar flow nucleate and widen, until all the domain become laminar. Left, the spatial distribution of U_0 at $t = t_0 + 50$ and right at $t = t_0 + 2000$. At $t = t_0$, the Reynolds number is decreased from $R_\mathrm{i} = 200$ to $R_\mathrm{f} = 168$.

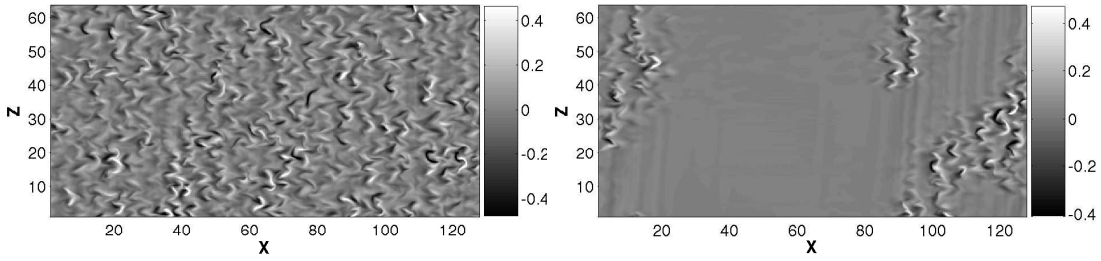

Figure 3.5: Tracking the transient decay with another velocity component. The spatial distribution of V_1 at $t = t_0 + 50$ (left) and at $t = t_0 + 2000$ (right). This distribution shows many structures which are analyzed in the coming chapters.

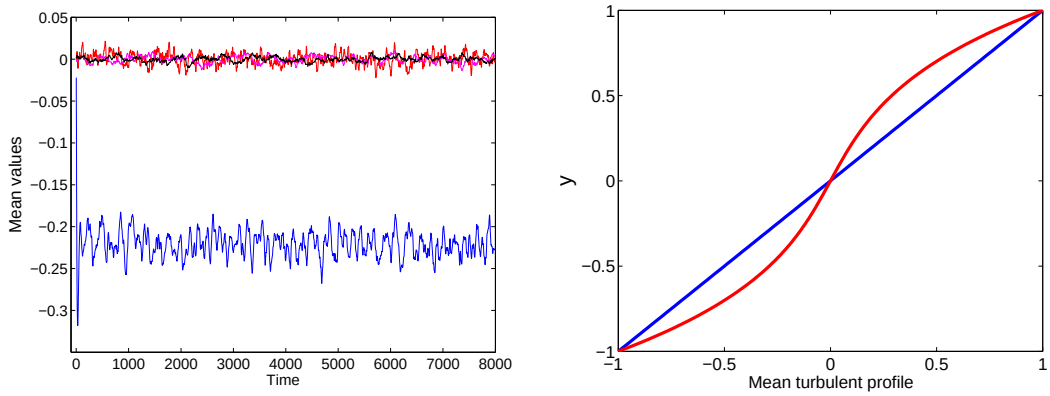

Figure 3.6: Left: Traces of the average flow components as functions of time: $\widetilde{U}_1 = -0.2210 \pm 0.0158$, $\widetilde{W}_1 = 1.8436e-04 \pm 0.0070$, $\widetilde{U}_0 = -1.6694e-04 \pm 0.0040$ and $\widetilde{W}_0 = -1.5888e-04 \pm 0.0030$ with $R = 200$ and $L_x \times L_z = 32 \times 32$. Right: Mean turbulent flow profile $u_{\mathrm{mf}} = y + \widetilde{U}_1 C y(1-y^2)$ with its characteristic **S**-shape. The laminar profile is in blue line. The values of $\widetilde{U}_1$, $\widetilde{W}_1$... are obtained by averaging the trace in the left panel over time.

Though the dimensions of the system for which these results have been obtained, $L_x = L_z = 32$, situate it well inside the extensive regime, we intended to check the robustness of the mean decay time behavior when the domain size is increased. Despite that gathering a large number of independent trials become tedious since it requires a much more computational (and human) times, we were able to collect few transients that shows that the mean decay time $\langle \tau_{\mathrm{tr}} \rangle$ diverges as $(R_{\mathrm{g}} - R)^{-1}$. However, the extrapolation to zero of $\langle \tau_{\mathrm{tr}} \rangle$ gives a slightly higher $R_{\mathrm{g}} \approx 173$. It is instructive, before closing this chapter, to give a glimpse on what happening in the physical space during a transient decay. Fig. 3.4 and Fig. 3.5 show the spatial distributions of the velocity U_0 and V_1 during a transient obtained by performing a quench experiment for $R_{\mathrm{i}} = 200$ to $R_{\mathrm{f}} = 168$, with $L_x \times L_z = 128 \times 64$. First , all the domain were turbulent ($R_{\mathrm{i}} = 200$). Then, the metastable turbulent flow nucleate pockets of laminar flow that next widens, until all the domain become laminar (between the two snapshots, $\Delta t \approx 2000$). The outbreak of these pockets can be seen as regions where the dissipation dominates the production of the turbulence and hence the perturbation energy decays to zero. In other words, regions where the self-sustainment of turbulence is no more "effective" become laminar pockets. Hence, the study of the self-sustainment of turbulence and the coexistence of laminar/turbulent domain and the contamination of one by the other are the keys to understand the transition to turbulence in pCf. The observed pattern in the spatial distribution of the velocity V_1 and U_0 are the starting point.

3.3.4 Mean turbulent flow

In the previous chapter, the mean values of the velocity component, e.g. U_1, was denoted by $\widetilde{U}_1 = \int_D U_1 \, ds/D$. Starting from an initial condition taken from some turbulent state, in which all the quantities $\widetilde{U}_1$, $\widetilde{U}_0 ... etc$ were turned off, it is interesting to note that after a short transient ($\Delta t \sim 50$), the mean value of the streamwise component U_1 builds up. As the sustained turbulent regime is reached, $\widetilde{U}_1$ has a negative value and is statistically constant ($\widetilde{U}_1 = -0.2210 \pm 0.0158$), as depicted in Fig. 3.6 with $R = 200$. In the same time, the transverse contribution $\widetilde{W}_1$ averages to zero, as well as $\widetilde{U}_0$ and $\widetilde{W}_0$.

The mean turbulent flow profile $u_{\rm mf} \equiv \overline{u}$ where the streamwise component $u = U_{\rm b} y + U_0 B(1-y^2) + U_1 C y(1-y^2)$, is displayed in Fig. 3.6 (right panel) as the superposition of a correction $Cy(1-y^2)$ with amplitude $\widetilde{U}_1$ to the base flow $U = U_{\rm b} y$, pointing out the expected formation of a central region with reduced shear. It will be interesting to study the patches of negative U_1 that should appear during growth/decay of turbulent spots, as a local counter-part to the steady state uniform correction in the sustained turbulent regime.

3.4 Conclusions

Our model that keeps quite close to the primitive Navier-Stokes equations and preserves their main properties also preserves the statistics of transients close to $R_{\rm g}$. Other questions posed by the transition to turbulence in globally sub-critical flows can be also attacked using our model, since it represents a simplified version of the Navier-Stokes equations, at least for R not too large. For example, whereas it is clear how streamwise vortices generate streaks through the lift-up effect introduced long ago, instability mechanisms and some nonlinear processes involved in the regeneration of vortices are still unclear in spite of recent progress described in (73). Also, the very coexistence of laminar and turbulent flow implied by global sub-criticality, the mechanisms by which one of the "phases" gains against the other, i.e., how spots grow (transition laminar $\rightarrow$ turbulent) or how the turbulent state collapses (transition turbulent $\rightarrow$ laminar), what is the role of the base flow correction (i.e., U_1) inside a turbulent domain, etc... are examples of questions that we intend to examine. Hence, the study of the model in view of elucidating specific processes such as the propagation of turbulent domains and the self-sustainment of turbulence with a deliberately spatiotemporal flavor is the heart of the forthcoming chapters.

Chapter 4

On the outskirts of a turbulent spot

Resumé

abstract

Numerical simulations of a model of plane Couette flow focusing on its in-plane spatio-temporal properties are used to study the dynamics of turbulent spots. While the core of a spot is filled with small scale velocity fluctuations, a large scale flow extending far away and occupying the full gap between the driving plates is revealed upon filtering out small scales. It is characterized by streamwise inflow towards the spot and spanwise outflow from the spot, giving it a quadrupolar shape. A correction to the base flow is present within the spot in the form of a spanwise vortex with vorticity opposite in sign to that of the base flow. The Reynolds stresses are shown to be at the origin of this recirculation, whereas the quadrupolar shape of the in-plane flow results from the transport of this recirculation by the base flow that pumps it towards the spot in the streamwise direction and flushes it in the spanwise direction to insure mass conservation. These results shed light on earlier observations in plane Couette flow or other wall flows experiencing a direct transition to turbulence by spot nucleation.

4.1 Introduction

Being stable against infinitesimal perturbations for all Reynolds numbers, plane Couette flow (pCf), the shear flow between two parallel plates moving in opposite directions with velocity $\pm U_{\mathrm{p}}$, is the prototype of flows that require localized finite amplitude disturbances to be pushed towards a turbulent regime. The transition is thus characterized by the nucleation and nonlinear growth of domains of turbulent flow, separated from laminar flow by sharp fronts and called *turbulent spots* (e.g., (98; 24; 27)). This kind of transition is not restricted to pCf but is also present in plane Blasius (boundary layer) flow (31) or plane Poiseuille flow. A review of some relevant laboratory experiments is given by Henningson *et al.* (42) and of their numerical counterpart given by Mathew & Das (69). In practice, direct transition to turbulence *via* spots can be expected whenever no low-Reynolds number instability of inertial origin exists, whereas turbulent solutions to the Navier–Stokes equations may exist and compete with the laminar base flow at moderate Reynolds number (68, Chap.6, §6.3).

Growing turbulent spots in pCf have been studied both experimentally (98; 24; 27) and numerically (25). In their pioneering direct simulations of Navier–Stokes equations with realistic no-slip boundary conditions, Lundbladh & Johansson (61) pointed out that (i) the wall-normal velocity component — typical of internal irregular small scale structures— faded away outside the spot but (ii) slowly varying in-plane velocity components extended far outside with an inwards streamwise motion towards the spot at the streamwise edges and an outward spanwise motion at its spanwise edges. These observations were made by low-pass Gaussian filtering the small scales of the velocity field at mid-gap. Tillmark (99) confirmed them experimentally by detecting the outwards spanwise component that developed over the full gap between the plates.

More recently, Schumacher & Eckhardt (91) re-investigated the growth of turbulent spots by means of direct numerical simulations but using unrealistic free-slip boundary conditions at the plates. By averaging the flow field between the two plates, they also observed that the turbulent spot was accompanied by an overall spanwise outflow and streamwise inflow, which they termed *quadrupolar*.

Spots seem to behave as obstacles in the base flow (58). Accordingly, they introduce additional pressure fields induced by the distribution of Reynolds stresses associated with the small scale fluctuations inside the spot and generating the large scale flows. A similar interpretation was put forward by Hayot & Pomeau (37) who introduced a *back-flow* to explain the organization of spiral turbulence in cylindrical Couette flow (18), with possible application to the banded turbulent regime discovered more recently in pCf (80) and numerically studied by Barkley & Tuckerman (5).

Previous experimental studies by Bottin *et al.* (12) have shown that, in the lowest part of the transitional Reynolds number range, flow patterns of interest extend over the full gap. We take advantage of this observation to study the

dynamics of spots using numerical simulations of a previously derived model of pCf shown to display sufficiently good properties for this purpose. The model is briefly sketched and typical results of simulations are presented in §4.2 emphasizing the output of the filtering procedure: (i) the in-plane quadrupolar flow outside the spot and (ii) a spanwise recirculation cell inside. These observations are then interpreted in §4.3 where the generation of these two large scale flow components is explained in terms of Reynolds stresses averaged over the surface of the spot. In the concluding section, we summarize our results and point to their relevance to the interpretation of previous observations in other wall flows of less academical interest, such as plane Poiseuille or Blasius flows.

4.2 Numerical simulations of turbulent spots

Our no-slip model was integrated on a rectangular (x, z) domain with periodic boundary conditions. Simulations were performed in a domain of size $(L_x \times L_z) = (128 \times 128)$ with effective space steps $\delta x = \delta z = 0.25$ and $\delta t = 0.01$; for details, see the previous chapter.

As an initial condition, we took localized expressions for Ψ_0, Ψ_1, and Φ_1:

$$\Psi_0(x, z, t = 0) = \Psi_1(x, z, t = 0) = \Phi_1(x, z, t = 0) = A \exp^{-(x^2+z^2)/S}$$

where A is an amplitude and S is the size of the germ. Parameters $A = 5$ and $S = 2$ were found efficient in generating turbulent spots for $R = 250$, well beyond $R_g \sim 173$, above which sustained turbulence is expected in our model. In practice, due to the highly unstable characteristics of the flow at such values of R, the apparent simplicity of the initial condition played no role after a few time units.

Spots are best illustrated by their most spectacular feature, namely their streamwise streaky structure (98; 24; 33; 16). In turn, the latter is best visualized from the amplitude U_0 since streamwise streaks are easily identified as regions where $|W_0| \ll |U_0|$ alternating in the spanwise direction, and since U_0 is associated with velocity perturbations that are maximum in the mid-gap plane $y = 0$. Figure 6.1 displays gray-level snapshots of U_0 at different times after launching. Denoting by (x_C, z_C) the in-plane coordinates of the center of the spot we see that, contrasting with the cases of plane Poiseuille or boundary layer flows, the spot does not drift due to the absence of mean advection. One can also notice its overall ovoid shape with dominant negative values (dark gray) for $x > x_C$ and positive values (light gray) for $x < x_C$. Regions where U_0 is positive correspond to high and low speed streaks for $y > 0$ and $y < 0$, respectively, which compares well with the experimental observations in (13).

In the sequel, we study the state at $t = 150$ but results and conclusions are identical at different times. The complete field (U_0, W_0) corresponding to this reference state is displayed in Figure 4.2. Except in the very center of the spot

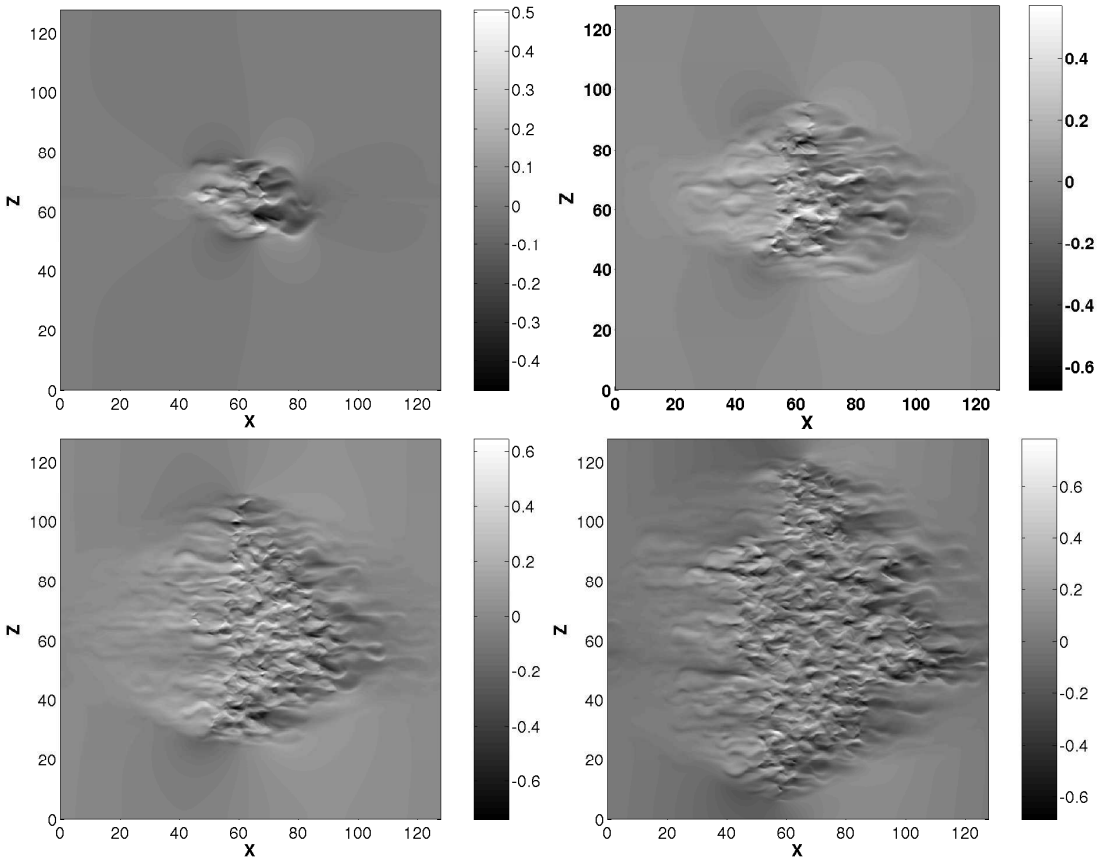

Figure 4.1: Growth of a turbulent spot at $R = 250$ in a wide domain ($L_x \times L_z = 128 \times 128$). Field of amplitude $U_0(x, z, t)$ in gray levels at $t = 50$, 150, 250 and 350 (from left to right and top to bottom). The whole domain becomes uniformly turbulent at $t \approx 700$.

that looks rather messy, streamwise structures are easily recognized but the trace of the large scale quadrupolar flow, of main concern in this chapter, is already visible.

As done by (61), we now proceed to the elimination of small scales using a Gaussian filter in spectral space:

$$\widehat{\overline{Z}}(k_x, k_z) = \widehat{Z}(k_x, k_z) \exp[-(k_x^2 + k_z^2)/(2\sigma)^2] \,, \tag{4.1}$$

where the hat denotes the Fourier transform of any quantity $Z = U_0, \ldots$. In physical space, this corresponds to a convolution with a kernel $\propto \exp\left(-\sigma\sqrt{\xi_x^2 + \xi_z^2}\right)$ where σ is the parameter controlling the width of the domain over which the small scales are smoothed out by the operation. Small scales, indicated by superscript 's', are recovered afterwards from the relation $Z^{\mathrm{s}} = Z - \overline{Z}$.

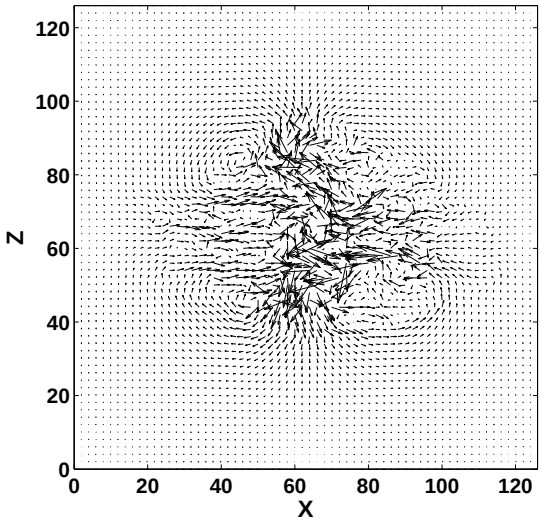

Figure 4.2: Streak flow field (U_0, W_0) at $t = 150$.

The diameter of the Gaussian averaging window has to be chosen in accordance with the size of the modulations to be eliminated, here the small scale streaks with spanwise wavelengths of the order 3–6 as can be guessed from Figure 4.2. We used $\sigma = \pi/11$, but the results were found to be rather insensitive to this choice provided that σ is sufficiently small.

As seen in Figure 4.3, this filtering procedure yields a clear picture of the flow outside the spot: the overall pattern formed by the in-plane components $\overline{U}_0$ and $\overline{W}_0$ has a quadrupolar aspect that could already be guessed from the consideration of the unfiltered stream-function Ψ_0 whose Laplacian is related to its vortical contents. In what follows, we term *drift flow* the large-scale velocity field $(\overline{U}_0, \overline{W}_0)$ with Poiseuille-like cross-stream profile by analogy with the case of Rayleigh–Bénard convection where a flow with the same global features was introduced by (93).

Figure 4.4 displays the velocity components associated with the fields Ψ_1, Φ_1. The distribution of the amplitude of $\overline{V}_1$, displayed in the left panel, represents an average wall-normal motion which is maximum in the mid-plane $y = 0$, positive on the right of the spot's center $x > x_C$ and negative on its left. In turn, the flow $(\overline{U}_1, \overline{W}_1)$ shown in the right panel consists of a region centered around the spot where $|\overline{U}_1| \gg |\overline{W}_1|$ and $\overline{U}_1 < 0$. This structure is easily interpreted as a wide spanwise recirculation cell with vorticity opposite in sign to that of the base flow. It is further reminiscent of what can be deduced from DNS simulations of (61), as displayed in seen their Fig. 9.

In Figure 4.5 (a) we display the profiles of $\overline{U}_0$ and $\overline{U}_1$ along a streamwise line going through the center of the spot. The dashed line corresponds to $\overline{U}_0$ and clearly points out the inwards character of the drift flow. In contrast, $\overline{U}_1$ (solid

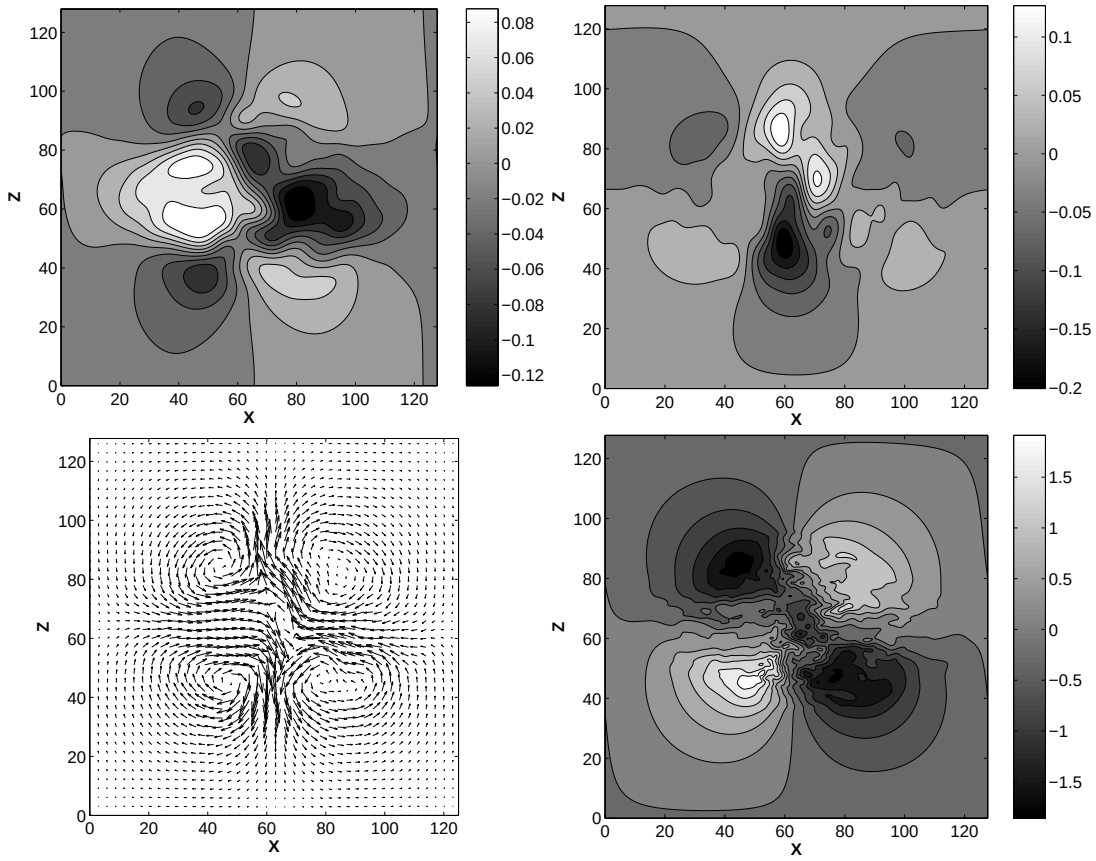

Figure 4.3: Top: level lines of averaged velocity components $\overline{U}_0$ (left) and $\overline{W}_0$ (right), illustrating large scale streamwise inflow and spanwise outflow around the spot. Bottom, left: representation of this flow as vectors. Bottom, right: level lines of the unfiltered stream function Ψ_0.

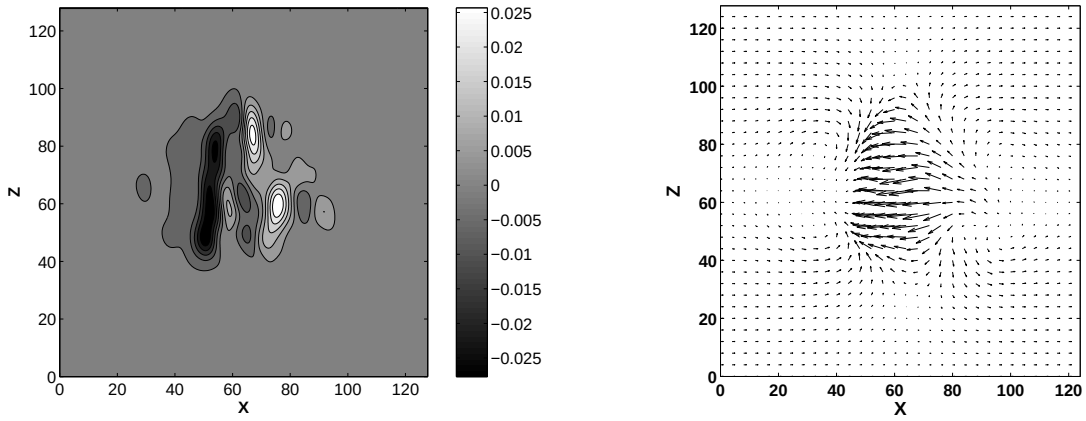

Figure 4.4: Velocity amplitudes $\overline{V}_1$ (left) and $(\overline{U}_1, \overline{W}_1)$ (right).

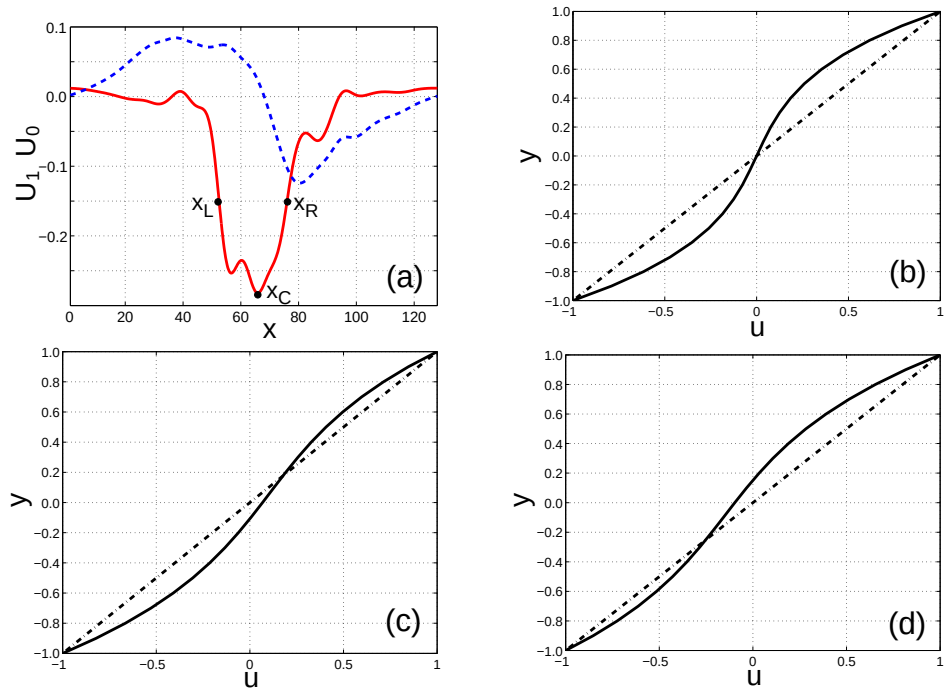

Figure 4.5: (a) $\overline{U}_1$ (red-solid) and $\overline{U}_0$ (blue-dashed) as functions of coordinate x along the streamwise center-line. (b–d) Full average streamwise velocity profiles $\overline{U}(y)$ at $x = x_C$ (b), $x = x_L$ (c) and $x = x_R$ (d); the laminar profile $U_b(y) \equiv y$ is indicated by a dashed-dotted line.

line) presents a deep trough at the location of the spot. At the spot's center where $\overline{U}_0 \simeq 0$, the superposition of the perturbation $u' = \overline{U}_1 C y(1-y^2)$ and the base flow $U_b(y) \equiv y$, shown in Figure 4.5 (b), displays the characteristic S shape of the turbulent velocity profile expected for pCf. The presence of the spot thus locally increases the wall friction. At different positions inside the spot, where $\overline{U}_0 \neq 0$ (and $\overline{W}_0 \neq 0$), the full superposition $\overline{U}(y) = y(1 + \overline{U}_1 C(1-y^2)) + \overline{U}_0 B(1-y^2)$ leads to asymmetric mean velocity profiles (Fig. 4.5(c) for point x_L and (d) for point x_R) that are reminiscent of the averaged profiles obtained by (5) in their simulations of the banded regime of turbulent pCf.

4.3 Generation of large scales from small scales

The mechanism driving the quadrupolar drift flow is discussed in terms of equations obtained by filtering from the model's equations, as described in the Appendix. We focus on the slowly varying quantities $A_0 = \overline{\Delta\Psi}_0$, $A_1 = \overline{\Delta\Psi}_1$, and $A_2 = \overline{\Delta\Phi}_1$, driven by $B_1 = -\xi\overline{U_0^s V_1^s}$ where $\xi = \alpha_2(\beta + \beta'') > 0$ and $B_2 = \alpha_1\overline{(U_0^s)^2 - (W_0^s)^2} + \alpha_2\overline{(U_1^s)^2 - (W_1^s)^2}$. The latter quantities represent the

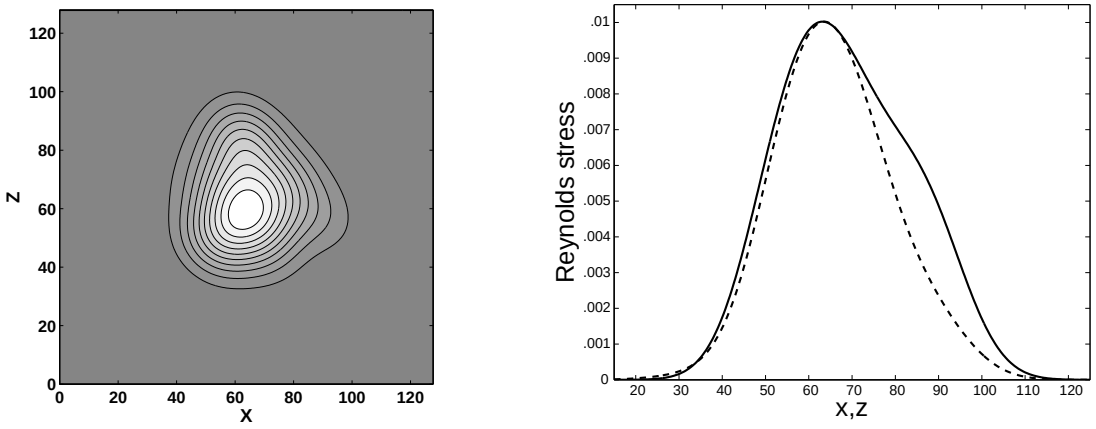

Figure 4.6: Distribution of the averaged Reynolds stress field $-\overline{U_0^{\rm s} V_1^{\rm s}}$ (left) and its variations along streamwise (solid line) and spanwise (dashed line) cuts through the maximum of the distribution taken as the center of the spot at $x_{\rm C} = 64$, $z_{\rm C} = 60$ (right).

components of the Reynolds stress tensor which do not average to zero over the surface of the spot (B_1 corresponds to the energy extracted from the laminar flow and B_2 mostly to the energy contained in the streamwise streaks).

Introducing slow variables X and Z whose rate of change is inversely proportional to the width of the window that is dragged over the data upon averaging through (4.1), one can observe that, in the equations, the quantity B_1 appears with one derivative in X or Z less than B_2, due to the fact that B_1 substitutes one in-plane differentiation by a cross-stream $\mathcal{O}(1)$ differentiation. Further assuming that the spot is in a quasi-steady state ($\partial_t \approx 0$) and that space derivatives are negligible when compared to $\mathcal{O}(1)$ constants when operating on the same quantities, at lowest significant order one can simplify Equations (4.5–4.7) to read:

$$R^{-1}\gamma_0 A_0 = a_1\left(\tfrac{3}{2}\partial_Z A_2 - \partial_X A_1\right), \tag{4.2}$$

$$R^{-1}\gamma_1 A_1 = \partial_Z B_1 - a_1 \partial_X A_0, \tag{4.3}$$

$$R^{-1}\gamma_1 A_2 = -\partial_X B_1. \tag{4.4}$$

The structure of this system invites one to examine the shape of the dominant Reynolds stress contribution B_1 as a function of the slow variables. Figure 4.6 displays the averaged Reynolds stress field associated with the small scales $-\overline{U_0^{\rm s} V_1^{\rm s}}$. As could be anticipated the latter is positive under the spot and one can furthermore observe its single-humped shape that, following (58) who developed a similar approach for spots in plane Poiseuille flow, can be modeled as a Gaussian function of the form $\exp[-(X^2+Z^2)/2]$. This assumption will help us to make an educated guess about the mechanisms at work.

Considering first Equation (4.4), from 3.6, i.e. $V_1 = \Delta\Phi_1/\beta$, we obtain that the contribution to $\overline{V}_1$ generated by B_1 is $\sim X\exp[-(X^2+Z^2)/2]$, i.e. a pattern

with a positive hump for $X > 0$ and a negative one for $X < 0$, resembling that in Figure 4.4 (left). This velocity component forms with $\overline{U}_1$ a large scale recirculation loop. As seen from 3.5, $\overline{U}_1$ contains two contributions of potential and rotational origins, respectively. In the neighborhood of the X axis, the variation of $\partial_X B_1$ is dominated by its X dependence so that $A_2 = (\partial_{XX} + \partial_{ZZ})\overline{\Phi}_1 \approx \partial_{XX}\overline{\Phi}_1 \sim -\partial_X B_1$ and, accordingly, $\partial_X \overline{\Phi}_1 \sim -B_1 \sim -\exp[-(X^2 + Z^2)/2]$. As to the rotational contribution $-\partial_Z \overline{\Psi}_1$, from (4.3) and forgetting the coupling with A_0 (which is of higher order owing to the way it is generated from A_1 and A_2), we have similarly $A_1 = (\partial_{XX} + \partial_{ZZ})\overline{\Psi}_1 \approx \partial_{ZZ}\overline{\Psi}_1 \sim \partial_Z B_1$, hence $-\partial_Z \overline{\Psi}_1 \sim -B_1$ so that it adds constructively to the potential part. The resulting $\overline{U}_1$ closes the recirculation loop as inferred from Figure 4.4 (right).

Inserting $A_1 \sim \partial_Z B_1$ and $A_2 \sim -\partial_X B_1$ in (4.2) we obtain a right hand side in the form $-XZ\exp[-(X^2 + Z^2)/2]$ for $\Delta\overline{\Psi}_0$ which is the vorticity contained in the (U_0, W_0) velocity field. This field displays four lobes with alternating signs. An approximation to the large scale drift flow along the axes can easily be obtained. Indeed, $\overline{U}_0$ can be obtained from $\overline{U}_0 = -\partial_Z \overline{\Psi}_0$ by integrating $A_0 = (\partial_{XX} + \partial_{ZZ})\Psi_0$ over Z and neglecting $\partial_{XX}\Psi_0$ since Ψ_0 varies much less with X than with Z along the X axis. We obtain $\overline{U}_0 \sim -X\exp[-(X^2 + Z^2)/2]$ which accounts for the observed inward flow along the streamwise center-line of the spot. The same argument can be transposed for the spanwise direction (now Ψ_0 varies most rapidly in the X direction, which makes $\partial_{ZZ}\Psi_0$ negligible and eases the integration over X), yielding $\overline{W}_0 \sim Z\exp[-(X^2 + Z^2)/2]$ which similarly accounts for the outward flow along the spanwise center-line. Notice however that this solution is too approximate to fulfil the continuity condition accurately since computing $\partial_X \overline{U}_0 + \partial_Z \overline{W}_0$ leaves a residual of the form $(X^2 - Z^2)\exp[-(X^2 + Z^2)/2]$, though the main contribution in $\exp[-(X^2 + Z^2)/2]$ is nicely compensated near the origin where the Gaussian is at its maximum. At any rate the chosen shape is only a simplifying assumption.

Physically, the spot is thus characterized by a mean correction to the base flow (represented in the model by $\overline{U}_1 < 0$) itself generated by a wall normal velocity component (here $\overline{V}_1$) and forming a large recirculation loop. In turn, the transport of that mean correction (here $\overline{U}_1 Cy(1 - y^2)$) by the base flow appears to be a source term for the large scale drift flow (here $(\overline{U}_0, \overline{W}_0)$) whose pattern is enslaved to its streamwise gradient, balancing viscous forces and inertia (according to $R^{-1}\gamma_0 \overline{U}_0 + a_1 \partial_x \overline{U}_1 \approx 0$) and expressing flow continuity ($\partial_x U_0 + \partial_z W_0 = 0$).

4.4 Conclusion

In this chapter, we have studied the large scale structure of the flow inside and around a turbulent spot in a transitional pCf model focusing on the in-plane dependence of a small number of velocity amplitudes. The approach is supported

by the qualitative consistency between previous experimental results in the transitional regime (13) and our own numerical simulations of the model.

Inside the spot, we find a wide spanwise recirculation loop with vorticity opposite in sign to that of the base flow. In particular, a patch of streamwise correction counteracting the base flow is observed, giving an S shape typical of turbulent flows to the velocity profile inside the spot. A reduced model (4.3–4.4) links this recirculation to Reynolds stresses $-\overline{U_0^{\rm s} V_1^{\rm s}}$ generated by the small scale fluctuations. Outside the spot, the existence of an inward-streamwise outward-spanwise quadrupolar drift flow has been pointed out, the origin of which is attributed to a linear coupling with this recirculation and linked to linear momentum conservation through (4.2). By simply assuming that the region where the Reynolds stresses contribute to the turbulent energy production (i.e. > 0) is one-humped with localized support, the main features of the large scale flow extracted from numerical simulations by filtering are recovered. In this approach, we only focused on the generation of large scales by small scales but considered neither (i) the interactions between small scales themselves nor (ii) the feedback of large scales on small scales. Closure assumptions are clearly needed in order to have a self-consistent theory, and especially to explain the sustainment of turbulence within a spot, problem (i), and its spreading as time proceeds, problem (ii).

Owing to the general character of the argument leading to their existence, one might also expect to find these large scale corrections in and around spots developing in transitional shear flows other than pCf for which they have already been accounted for (61; 91; 99). Evidence of their presence can indeed be obtained from Figure 12 reporting numerical work of (41) on plane Poiseuille flow and from Figures 6 and 9 describing the result of ensemble averaging of turbulent spots in boundary layer flow with slightly adverse pressure gradient in the laboratory experiments of (92). Despite its limited cross-stream resolution, our modeling of transitional plane Couette flow has thus been shown to provide valuable explanations to previous observations, which might call for new laboratory experiments since, besides the theoretical challenge of understanding laminar–turbulent coexistence in detail, the problem of the transition to turbulence in wall flows has a great technical importance.

Appendix: Model's equations and derivation of (4.2–4.4)

It was observed in Figure 6.1 that the flow within the turbulent spot resembles developed turbulent flow, see also (42; 58). Accordingly, one obtains that the only contributions to the averaged equations come from the terms that keep a constant sign over the surface of the spot, namely the main Reynolds stress term $-\overline{U_0 V_1}$ associated with energy extraction from the mean flow and the other terms $\overline{U_0^2}$, $\overline{W_0^2}$, $\overline{U_1^2}$, and $\overline{W_1^2}$. Equations (3.1-3.3) then reduce to:

$$(\partial_t - R^{-1}(\Delta - \gamma_0))\Delta\overline{\Psi}_0 = \tfrac{1}{2}\partial_{xz}\left(\alpha_1\overline{U_0^2 - W_0^2} + \alpha_2\overline{U_1^2 - W_1^2}\right) + a_1\left(\tfrac{3}{2}\partial_z\Delta\overline{\Phi}_1 - \partial_x\Delta\overline{\Psi}_1\right), \tag{4.5}$$

$$(\partial_t - R^{-1}(\Delta - \gamma_1))\Delta\overline{\Psi}_1 = \partial_z\left(\overline{-\xi U_0 V_1}\right) - a_1\partial_x\Delta\overline{\Psi}_0\,, \tag{4.6}$$

$$\left[\partial_t(\Delta - \beta^2) - R^{-1}(\Delta^2 - 2\beta^2\Delta + \gamma_1\beta^2)\right] = \beta^2\partial_x\left(\overline{-\xi U_0 V_1}\right), \tag{4.7}$$

with $\xi = \alpha_2(\beta + \beta'')$. Following Li & Widnall, we then split the velocity components into small and large scales, i.e. $U_0 \rightsquigarrow \overline{U}_0 + U_0^{\mathrm{s}}$, etc., and only keep the contribution to the Reynolds stresses coming from the small scales. This leads to the same set of equations as above except that U_0, $U_1 \ldots$ are replaced by their small scale parts U_0^{s}, U_1^{s} etc.

Chapter 5

Generation mechanism for streamwise vortices

abstract

Streamwise vortices play important role in the sustainment of wall-turbulence. Their generation mechanism is studied in the particular case of plane Couette flow using a model in terms of partial differential equations, obtained from the Navier-Stokes equations through a Galerkin projection. The sequence of events leading to their generation is as follows. A spanwise vortex, with vorticity opposite in sign to that of the base flow, is deformed by a flow spanning the whole gap between the driving plates. The resultant vortex has a crescent shape and its two legs are the streamwise vortices. The generation mechanism for the spanwise vortices is also elucidated. Comparisons with previous works are presented and a self-sustained cycle for wall-bounded turbulence is proposed.

5.1 Introduction

For a sufficiently large values of the Reynolds number, laminar flow close to a solid wall becomes turbulent. This laminar-turbulent transition process still leaves open several questions and problems of great practical importance. The turbulent state is sustained and has complex dynamics involving the interactions of many spatio-temporal flow patterns, referred as coherent structures (e.g. (76; 96)). Regions where the Reynolds stress $-uv$ (u is the streamwise (x) and v the wall-normal (y) perturbation velocity components) is positive indicate the spatial locations where energy is being extracted from the laminar flow and fed into the turbulent state (e.g. (77)). Therefore, to understand how turbulence is sustained, it is of interest to study the origin of this Reynolds stress.

A particular type of coherent structure having the dominant role in turbulence production is the streamwise vortex, an x-elongated region of streamwise vorticity. It is now well established that the generation of Reynolds stress $-uv$ occurs on each side of a streamwise vortex. The upwelling ($v \geq 0$) and downwelling ($v \leq 0$) motions associated with this vortex generate, through the lift-up effect, the streamwise perturbation u such that the product $-uv$ is positive on each side of the vortex (77).

For this reason, elucidating the generation mechanism of the streamwise vortices is crucial to understand the production of turbulence, as is the goal of this chapter in which we are concerned with the particular case of plane Couette flow (pCf), shear flow between two parallel plates moving in opposite directions with velocities $\pm U_\mathrm{p}$. This flow is stable for all Reynolds numbers R, but experiences a transition to turbulence when R exceeds the stability threshold $R_\mathrm{g}^\mathrm{exp} \sim 325$, based on the half-gap h and the velocity U_p ((13)).

An important feature of the streamwise vortices in pCf, for low-Reynolds numbers, is that they span all the gap between the driven plates. In their direct numerical simulations of Navier-Stokes equations, Lee & Kim (57) observed such vortical structures with circular cross-section and elongated in the x-direction. Their computational small box was sufficient to contain a pair of such vortices. Numerical simulations investigating the effect of the domain size on the dynamics of these structures were carried out by Komminaho *et al.* (56) who considered larger computational box ($88h \times 25h$). They obtained similar streamwise vortices but their dynamics was less constrained by the size of the box and they can meander in the flow field (Figure 8 in (56)). The used Reynolds number was $R = 750$, i.e. roughly twice the value of the stability threshold $R_\mathrm{g}^\mathrm{exp}$.

Papavassiliou & Hanratty (75) discussed some conditions for the existence of large streamwise vortices that extend from wall to wall. For example, a favorable property to their existence is the asymmetry of the base flow profile. In fact, flow outward from the bottom wall that extracts energy from the base flow, continues to do so when it moves past the mid-plane. Hence, the vortices contribute to the turbulence production by extracting energy across the entire gap and injecting it

into the turbulent state. In turn, this turbulent state sustains these vortices by some mechanisms, not clarified yet.

Tsukahara *et al.* (101) further examined the effects of the computational box size and the value of the Reynolds number on these vortices. Through the visualization of the instantaneous flow field, they found that these vortices are present for $R = 750$ as well as for the higher value $R = 2150$ (with the definition above) and that their spanwise width is about $5h$.

Finally, the studies of Bottin *et al.* (13) (for Reynolds numbers near R_g^{exp}) and, more recently, of Kitoh *et al.* (51) (for $R = 750$), give experimental evidence for these streamwise vortices and hence confirm the previous numerical results.

We take advantage of these numerical and experimental observations to study the dynamics of the streamwise vortices by means of numerical simulations in an extended computational box with low wall-normal resolution.

The outline of this chapter is as follows. In section §5.2, some mechanisms for the generation of streamwise vorticity are first presented. Their different contributions are studied with our model and comparisons are made with some previous works. The evolution of this streamwise vorticity to streamwise vortices is analyzed and a generation mechanism for streamwise vortices is elucidated in §5.3. It is further developed in §5.4 using a 1-dimensional model. In the last section §5.5, the origin of the spanwise vortices, flow patterns involved in this mechanism, is investigated. By piecing together the mechanisms described in this chapter, a self-sustained process for wall-bounded turbulence is proposed. The main results of the four sections are summarized in the conclusion §5.6.

5.2 Generation of streamwise vorticity

5.2.1 Previous works

The natural starting point of our study is the equation governing the streamwise vorticity. By denoting u the streamwise (x), v the wall-normal (y) and w the spanwise (z) velocity components (perturbations and base flow), the equation of the streamwise vorticity $\Omega_x = \partial_y w - \partial_z v$ reads (e.g.(90)):

$$\partial_t \Omega_x = -u\partial_x \Omega_x - v\partial_y \Omega_x - w\partial_z \Omega_x + \Omega_x \partial_x u + \partial_z u \partial_x v - \partial_y u \partial_x w + \Delta^2 \Omega_x / R. \quad (5.1)$$

The three first terms represent the nonlinear advection of Ω_x and the dissipation term is $\Delta^2\Omega_x/R$, where R is the Reynolds number. The stretching term is $\Omega_x\partial_x u$ and the tilting terms are $\partial_z u\partial_x v$ and $-\partial_y u\partial_x w$. More precisely, the term $-\partial_y u\partial_x w$ represents the generation of streamwise vorticity Ω_x by the tilting of wall-normal vorticity $\partial_x w$ into the x-direction by the wall-normal shear $\partial_y u$, as shown in Fig. 5.1. In the same way, the second term $\partial_z u\partial_x v$ represents the generation of Ω_x by the tilting of the spanwise vorticity $\partial_x v$ into the x-direction by the shear flow $\partial_z u$, as shown in Fig. 5.2.

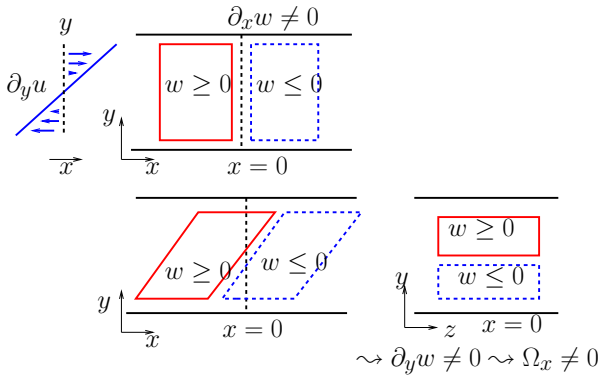

Figure 5.1: Tilting term $-\partial_y u \partial_x w$. Consider two regions of the spanwise velocity w which alternate in sign in the x-direction ($\partial_x w \neq 0$). Due to the wall-normal shear $\partial_y u$, the initial velocity distribution is deformed. Near $x = 0$, the velocity w becomes y-dependent, as shown in the plane (y, z). Consequently, streamwise vorticity is generated.

Despite the fact that these mechanisms are well-known, there is, however, much less of an agreement concerning the origin of streamwise vorticity (and vortices) in wall-bounded shear flows. Many possible scenarios have been proposed in the literature (for a review, see (76)) and some of them are given below, proposed either for pCf or for other shear flows.

In their numerical investigation of plane Poiseuille flow, Jimenez & Moin (49) were interested in the generation mechanism of streamwise vorticity. By analyzing the vorticity field, they found that a streamwise vortex lifts a layer of vorticity and rolls it around itself. When this rolled vortex layer encounters another one, wall-normal vorticity is induced. Then, the tilting of this vorticity into the streamwise direction by the mean shear (the term $-\partial_y u \partial_x w$) generates Ω_x.

Studying pCf, Hamilton *et al.* (36) found that $-\partial_y u \partial_x w$ was the source term with the largest contribution to Ω_x. However, much of the streamwise vorticity induced by this term is not in the correct x-independent Fourier mode, but in other modes, which do not represent streamwise vortices. Hence they argued that despite the fact that this mechanism is an important one, it is not sufficient to produce streamwise vortices. They suggested that some additional nonlinear constructive interactions must occur between these x-dependent Fourier modes to complete the generation of the streamwise vortices.

Using instantaneous visualizations of the velocity field, obtained from numerical simulations of plane Poiseuille flow, Brooke & Hanratty (15) found that the largest contribution to the generation of the streamwise vorticity comes from the term $-\partial_y u \partial_x w$. The contribution of the term $\partial_z u \partial_x v$ is less than 10% of that of $-\partial_y u \partial_x w$.

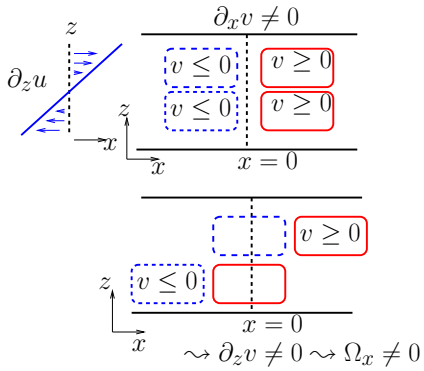

Figure 5.2: Tilting term $\partial_z u \partial_x v$. Consider two regions of the wall-normal velocity v which alternate in sign in the x-direction ($\partial_x v \neq 0$). Due to the spanwise shear $\partial_z u$, the initial velocity distribution is deformed. Near $x = 0$, the velocity v becomes z-dependent.

Moreover, by means of direct numerical simulations of turbulent channel flow, Schoppa & Hussain (90) have found that Ω_x intensification occurs due to the generation term $-\partial_y u \partial_x w$, which dominates the $\partial_z u \partial_x v$ term. However, according to these authors, the term $-\partial_y u \partial_x w$ is not responsible for vortex formation, which is driven by the stretching term $\Omega_x \partial_x u$. Hence, regions where $\partial_x u$ is positive are the eventual locations of streamwise vortices. The finite amplitude of this $\partial_x u$ is a consequence of the streak waviness. In our study, the locations where $\partial_x u \neq 0$ are also important, however, they are not due to the streak waviness but to the formation of stagnation points, as we will see later on.

5.2.2 Comparisons

From the streamwise vorticity $\Omega_x = \partial_y w - \partial_z v$, we define the averaged streamwise vorticity over the gap as:

$$\omega_x \equiv \int_{-1}^{1} \Omega_x S_1(y)\, dy. \tag{5.2}$$

Then, to compare the contributions of the individual nonlinear terms of the vorticity equation (5.1) to the generation of ω_x, it is easier to consider the equation for ω_x^2, since the quantity $\partial_t \omega_x^2$ is positive at (x, z) locations where ω_x is being increased, and negative where it is being reduced, as used in (36). The equation of ω_x^2 is obtained directly from Eq. 5.1 by averaging over y and then over the horizontal plane (x, z) and reads (with neither dissipative nor advective terms):

$$\frac{d}{dt}\overline{\omega_x^2} = \overline{t_1} + \overline{t_2} + \overline{t_3}, \tag{5.3}$$

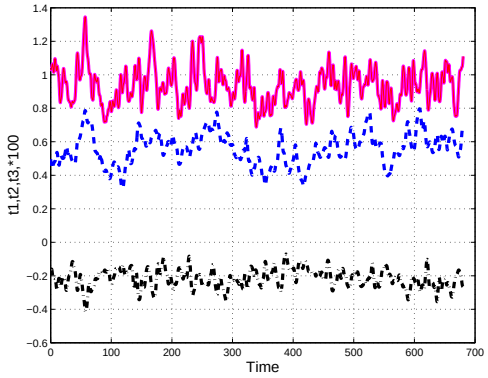

Figure 5.3: Contributions of the three terms $\overline{t_1}$, $\overline{t_2}$ and $\overline{t_3}$ to the quantity $\frac{d}{dt}\overline{\omega_x^2}$. Temporal evolution of: $\overline{t_1}$ in black dotted-line, $\overline{t_2}$ in blue dashed-line and $\overline{t_3}$ in red solid-line.

with: $t_1 = \langle \Omega_x \partial_x u \rangle$, $t_2 = \langle \partial_z u \partial_x v \rangle$, $t_3 = \langle -\partial_y u \partial_x w \rangle$, and where for a function f, we note

$$\langle f \rangle = (\int_{-1}^{1} f S_1(y)\, dy)\omega_x, \quad \text{and} \quad \overline{f} = \int_{xz} f\, dxdz.$$

Throughout the chapter, numerical simulations are performed in a computational box with streamwise and spanwise lengths $L_x \times L_z = 32 \times 32$. The spatial resolution is $dx = dz = 0.25$, the time step is $dt = 0.01$ and the Reynolds number is $R = 180 \geq R_{\mathrm{g}}$.

In accordance with the previous works, we find that the tilting term $-\partial_y u \partial_x w$ represents the largest positive contribution to the generation of the streamwise vorticity, as shown in Fig. 5.3. Despite the fact that the positive contribution of the term $\partial_z u \partial_x v$ is smaller, it is not negligible compared to that of $-\partial_y u \partial_x w$. Hence, both tilting mechanisms are important. In addition to that, the generation of streamwise vortices is not due to the stretching term $\Omega_x \partial_x u$ which here is a *compression* term since its contribution is negative. This last point attests to the fact that there is another mechanism which elongates and transforms streamwise vorticity into streamwise vortices.

It is rewarding to examine why the behaviors of the two tilting terms are similar while the stretching term is a sink term. This analysis is done in the next section.

5.3 Generation of streamwise vortices

5.3.1 Equations of the vorticities

Using the velocity expansions of the perturbations and Eq. 5.2, we have:

$$\omega_x \equiv \int_{-1}^{1} \Omega_x S_1(y)\, dy = \beta W_1 - \partial_z V_1,$$

where $\beta = \sqrt{3}$ accounts for a wall-normal gradient. Then the governing equation for ω_x follows from W_1 and V_1-equations and reads (without the dissipative terms):

$$\begin{aligned} \partial_t \omega_x &= \beta \partial_t W_1 - \partial_z \partial_t V_1 = \\ &= -\alpha_2 (U_0 \partial_x . + W_0 \partial_z .) \tilde{\omega_x} + \beta \beta'' V_1 W_0 \\ &+ \alpha_3 \partial_z U_0 \partial_x V_1 - a_1 \beta \tilde{U_\mathrm{b}} \partial_x W_0 + \tilde{\omega_x} \partial_x U_0, \end{aligned} \tag{5.4}$$

where $\tilde{U_\mathrm{b}} = U_\mathrm{b} + \frac{\alpha_2}{a_1} U_1$ and $\tilde{\omega_x} \equiv (\beta W_1 - \frac{\alpha_3}{\alpha_2} \partial_z V_1)$. Due to the fact that in the no-slip case $\alpha_2 = \sqrt{15}/6 \neq \alpha_3 = 5\sqrt{15}/22$, in contrast with the free-slip case, we have $\omega_x \neq \tilde{\omega_x}$. However, the spatial distributions of ω_x and $\tilde{\omega_x}$ are similar and in the following they are considered equivalent.

Two remarks are in order. First, the last three terms in (5.4) exist in both free- and no-slip cases. Their physical interpretations are easily recovered from Eq. 5.1 and are as follows. The term $\tilde{\omega_x} \partial_x U_0$ accounts for the stretching of the vorticity Ω_x by the flow $U_0 R_0(y)$ filling all the gap. The term $\partial_z U_0 \partial_x V_1$ represents the tilting of a spanwise vorticity $\partial_x V_1 S_1(y)$ by a spanwise shear of the flow component $U_0 R_0(y)$. The last term $-a_1 \beta \tilde{U_\mathrm{b}} \partial_x W_0$ accounts for the tilting of wall-normal vorticity $\partial_x W_0 R_0(y)$ by the flow component $U(y) + U_1 R_1(y)$. In regions where U_1 is negative, $U(y) + U_1 R_1(y)$ has locally an **S**-shape (for the no-slip case). Hence, $U_1 R_1(y)$ represents a *local* correction to the base flow $U(y)$. The flow component $U(y) + U_1 R_1(y)$ as well as its projection $\tilde{U_\mathrm{b}} = U_\mathrm{b} + \frac{\alpha_2}{a_1} U_1$ are termed herein the corrected base flow. The factor β in front of $-\beta \tilde{U_\mathrm{b}} \partial_x W_0$ accounts for the wall-normal gradient of this flow.

Second, to compare the contributions of these terms to the generation of the streamwise vorticity, we multiply Eq. 5.4 by ω_x, average over the domain the three quantities $\omega_x(-a_1 \beta \tilde{U_\mathrm{b}} \partial_x W_0)$, $\omega_x(\alpha_3 \partial_z U_0 \partial_x V_1)$ and $\omega_x \tilde{\omega_x} \partial_x U_0$ and study their temporal contributions to $\frac{d}{dt}\overline{\omega_x^2}$. As in §5.2.2, we find that the two first terms are source terms with positive contribution of roughly the same order and that the last term is a sink term.

For later use, we introduce the spanwise vorticity Ω_z associated with the perturbations and defined by $\Omega_z = \partial_x v' - \partial_y u'$ with $u' = U_0 R_0(y) + U_1 R_1(y)$ and $v' = v = V_1 S_1(y)$. Once averaged over y, it yields:

$$\omega_z \equiv \int_{-1}^{1} \Omega_z S_1(y)\, dy = \partial_x V_1 - \beta U_1,$$

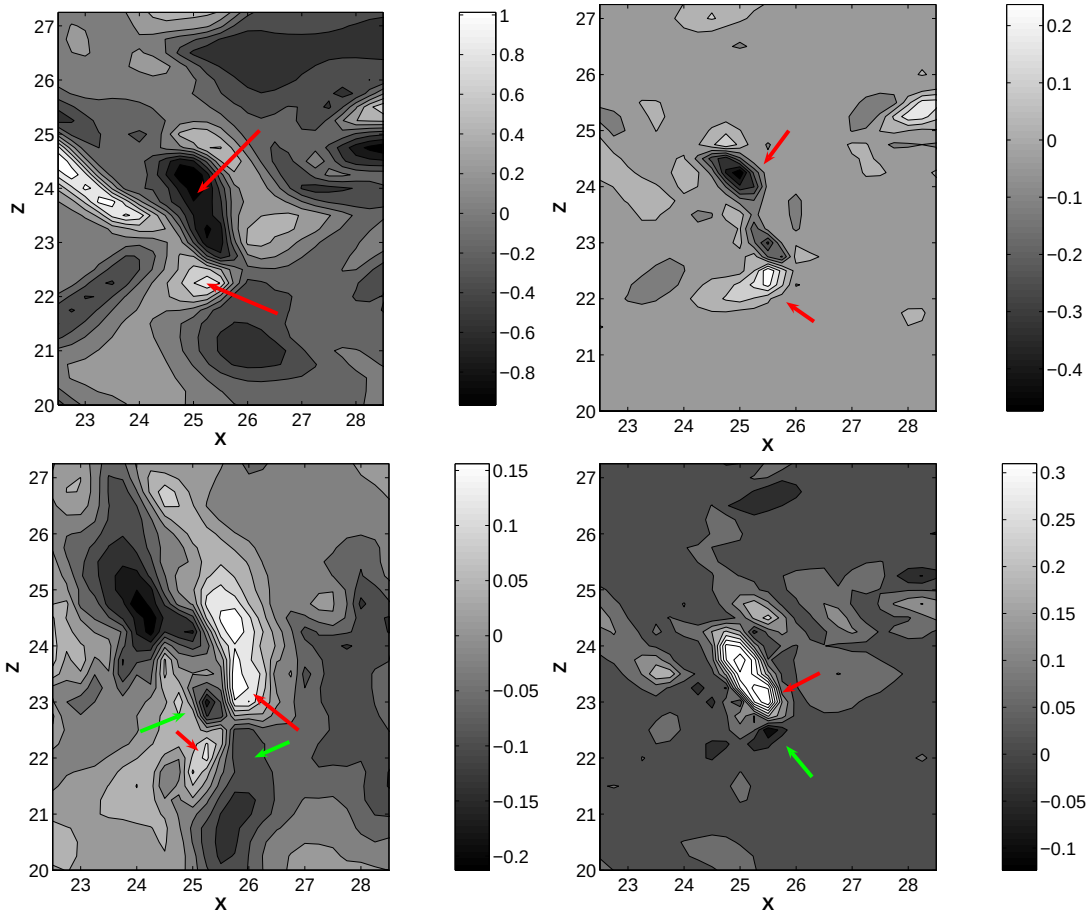

Figure 5.4: From left to right and top to bottom: ω_x, $\alpha_3 \partial_z U_0 \partial_x V_1$, $-a_1 \beta \tilde{U_b} \partial_x W_0$ and $\tilde{\omega_x} \partial_x U_0$, at $t = 5$. There are two patches of positive and negative ω_x, indicated by the two arrows. The distributions of $\alpha_3 \partial_z U_0 \partial_x V_1$ and of $-a_1 \beta \tilde{U_b} \partial_x W_0$ are similar to the one of ω_x.

and its governing equation reads:

$$\begin{aligned} \partial_t \omega_z &= \partial_x \partial_t V_1 - \beta \partial_t U_1 = \\ &= -\alpha_2 (U_0 \partial_x . + W_0 \partial_z .) \tilde{\omega_z} + \beta (a_1 U_b \partial_x U_0 + W_1 \partial_z U_0) \\ &\quad -\beta'' \beta V_1 U_0 - \alpha_3 \partial_x W_0 \partial_z V_1 + \alpha_2 \tilde{\omega_z} \partial_z W_0, \end{aligned} \tag{5.5}$$

where $\tilde{\omega_z} \equiv (\frac{\alpha_3}{\alpha_2} \partial_x V_1 - \beta U_1)$. The spatial distributions of ω_z and $\tilde{\omega_z}$ are similar (for the same reason as before for ω_x and $\tilde{\omega_x}$) and they are considered equivalent.

5.3.2 Generation of ω_x and the *key-structure*

The spatial distributions of the last three terms in Eq. 5.4 are now studied. As attested to by Figure 5.4, both terms $\alpha_3 \partial_z U_0 \partial_x V_1$ and $-a_1 \beta \tilde{U_b} \partial_x W_0$ are source

terms since their distributions are similar to the one of ω_x, in contrast with $\tilde{\omega_x}\partial_x U_0$ which is a sink term since it has opposite-signed distribution to that of ω_x. Since the nature of these terms is related to the local structure of the flow, the distributions of the velocity components are now studied.

On one hand, the distribution of V_1, displayed in the left panel of Fig. 5.5, represents two patches of negative and positive values elongated in the spanwise direction. On the other hand, the in-plane flow (U_1, W_1) shown in the right panel of Fig. 5.5 consists of a region where $|U_1| \gg |W_1|$ and $U_1 \leq 0$. Regions where U_1 is negative play a crucial role in the dynamics as we will see. As explained in Fig. 5.6, these particular distributions of (U_1, W_1) and V_1 represent a z-elongated spanwise vortex with positive ω_z (Fig. 5.5). In the literature, such vortices are called retrograde spanwise vortices since their rotation is in the opposite sense to the base flow. Note that regions in which ω_z has a sign opposite to the mean wall shear were observed in (49) (qualified there by *curious phenomenon*).

Furthermore, the pattern formed by the flow (U_0, W_0), given in Fig. 5.5, has a quadrupolar structure with an inflow U_0 towards the patch of ω_z and a spanwise outflow W_0 pointing out of this patch. The (x, z)-location where $U_0 \approx 0$ and $\partial_x U_0 \leq 0$ is termed a stagnation point herein (as the one shown in Fig. 5.5).

Hence, in the region where ω_x is generated, there is a spanwise vortex, defined by a z-elongated patch of positive ω_z, and a quadrupolar flow (U_0, W_0) with a stagnation point ($U_0 \approx 0$ and $\partial_x U_0 \leq 0$). In the following, this particular flow-structure is termed key-structure. In chapter 4, we have encountered a similar flow-structure involving a large-scale recirculation in the (x, y)-plane elongated in the z-direction and a large-scale quadrupolar flow (U_0, W_0) with the inflow towards the spot (compare Fig. 5.5 here with Fig. 4.3 and Fig. 4.4). By similarity, this particular flow-structure, developing on the outskirts of the spot, can be called a *large-scale key-structure*. Hence, it is interesting to note that similar flow-structure does occur inside the turbulent domain (localized or not) and outside it.

Next, by considering Eq. 5.4 and studying each term in the r.h.s with the idealized flow distribution given by the key-structure, we can easily recover the nature of each term. For example, it is clear that the term $\omega_x \partial_x U_0$ is a sink term since near the stagnation point where $\partial_x U_0 \leq 0$, it has a negative contribution in $\frac{d}{dt}\overline{\omega_x^2} = ... + \overline{\omega_x^2 \partial_x U_0}$. The nature of the two remaining tilting terms is explained in Fig. 5.7. This analysis highlights the role of the key-structure on the generation of streamwise vorticity ω_x. Its occurrence will be attested to by some statistical tools in §5.3.6.

Before tracking the evolution of this generated ω_x to streamwise vortices, it is intriguing to compare the contribution of each tilting term to this ω_x. Such comparison is rewarding for the physical interpretation of the forthcoming generation process of streamwise vortices.

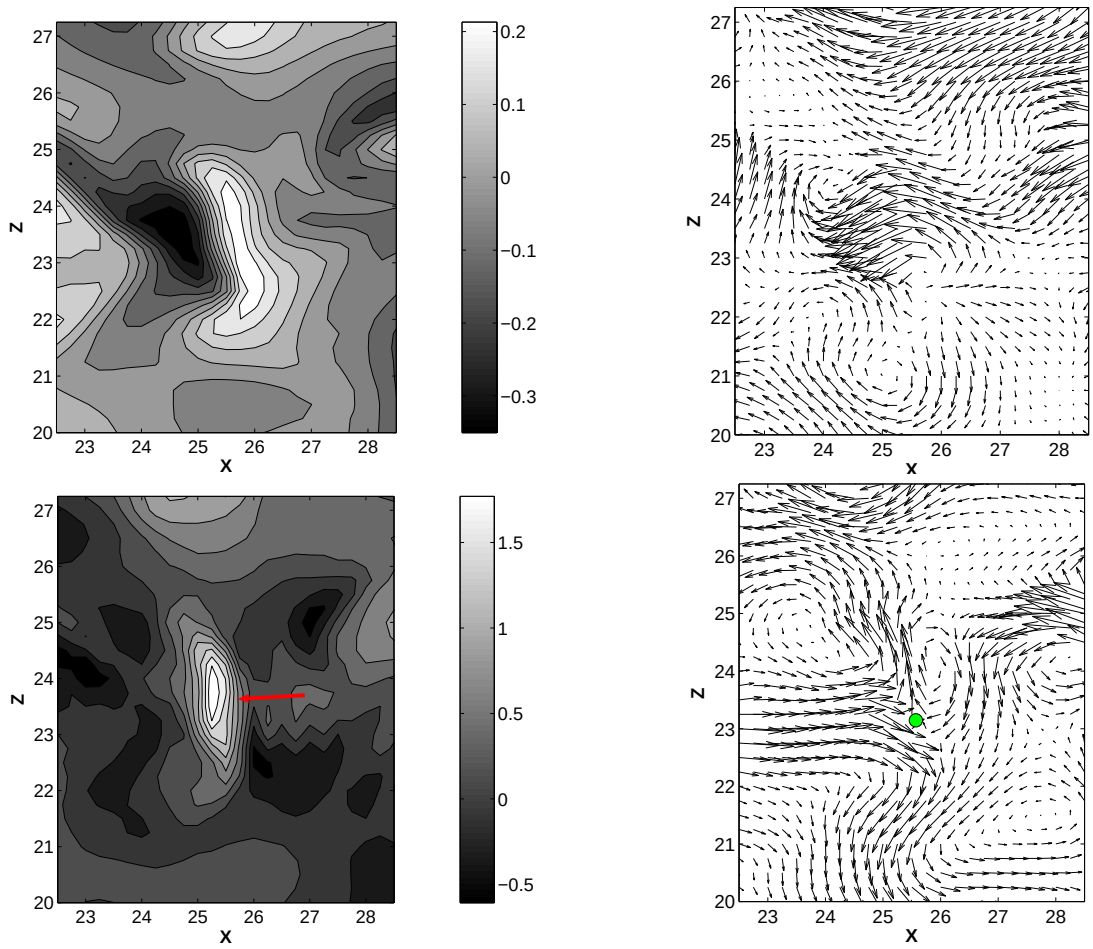

Figure 5.5: From left to right and top to bottom: Spatial distribution of V_1, the flow field (U_1, W_1), ω_z, and the flow field (U_0, W_0). The stagnation point ($U_0 \approx 0$ and $\partial_x U_0 \leq 0$) is marked with a red point. $t = 6$.

5.3.3 Different roles of both tilting terms: Complementarity

The contribution of each tilting term in the generation of ω_x is now discussed. Special care is to be addressed to the wall-normal velocity V_1 since the existence of streamwise vorticity ω_x does not imply existence of streamwise vortices unless V_1 exists. Thus, it is important to note that the velocity V_1 associated with the generated ω_x comes from the tilting of spanwise vorticity by the spanwise shear (the term $\partial_z U_0 \partial_x V_1$) and that the tilting of wall-normal vorticity contributes only to the generation of spanwise velocity W_1.

Since this wall-normal velocity V_1 represents the potential part of the flow ($\beta V_1 = \Delta_2 \Phi_1$), it is clear that only the terms present in the equation governing

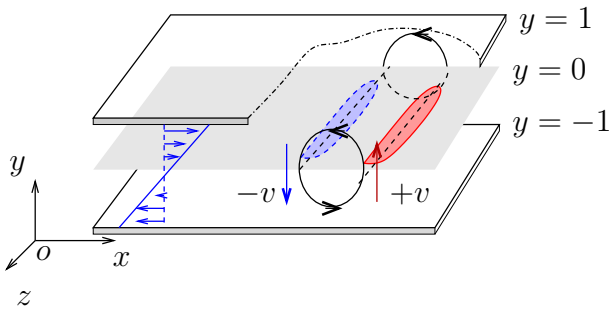

Figure 5.6: The 3D reconstruction of the flow (U_1R_1, W_1R_1, V_1S_1), using the distribution of the velocity components U_1, V_1 and W_1 given in Fig. 5.5, shows a spanwise vortex with vorticity opposite in sign to that of the base flow. Red-solid (blue-dashed) contours indicate regions of positive (negative) values.

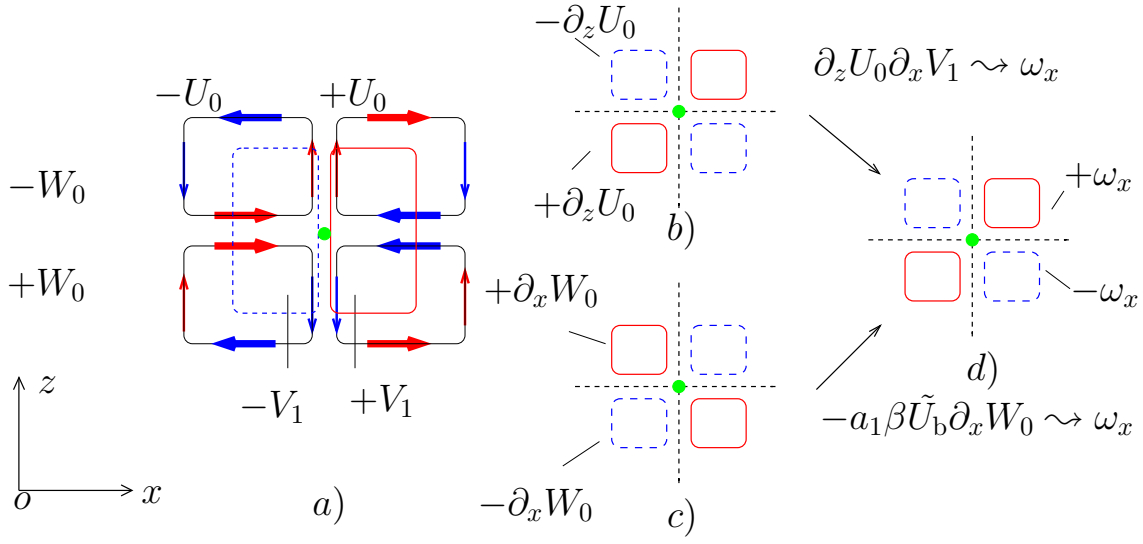

Figure 5.7: Consider the idealized key-structure represented by the quadrupolar flow (U_0, W_0) with its stagnation point indicated by the black point and with two z-elongated patches of V_1, with x-alternating sign (a). The distributions of $\partial_z U_0$ and $\partial_x W_0$ are easily obtained from that of U_0 (b) and W_0 (c). Then, the signs of $\partial_x V_1 \partial_z U_0$ (with $\partial_x V_1 \geq 0$) and of $-a_1 \beta \tilde{U}_\mathrm{b} \partial_x W_0$ (where $\tilde{U}_\mathrm{b} \geq 0$) are determined (d). The distributions of the two terms are hence similar around the stagnation point. Red-solid (blue-dashed) contours indicate regions of positive (negative) values. Positive (negative) quantities are marked with "+"(-).

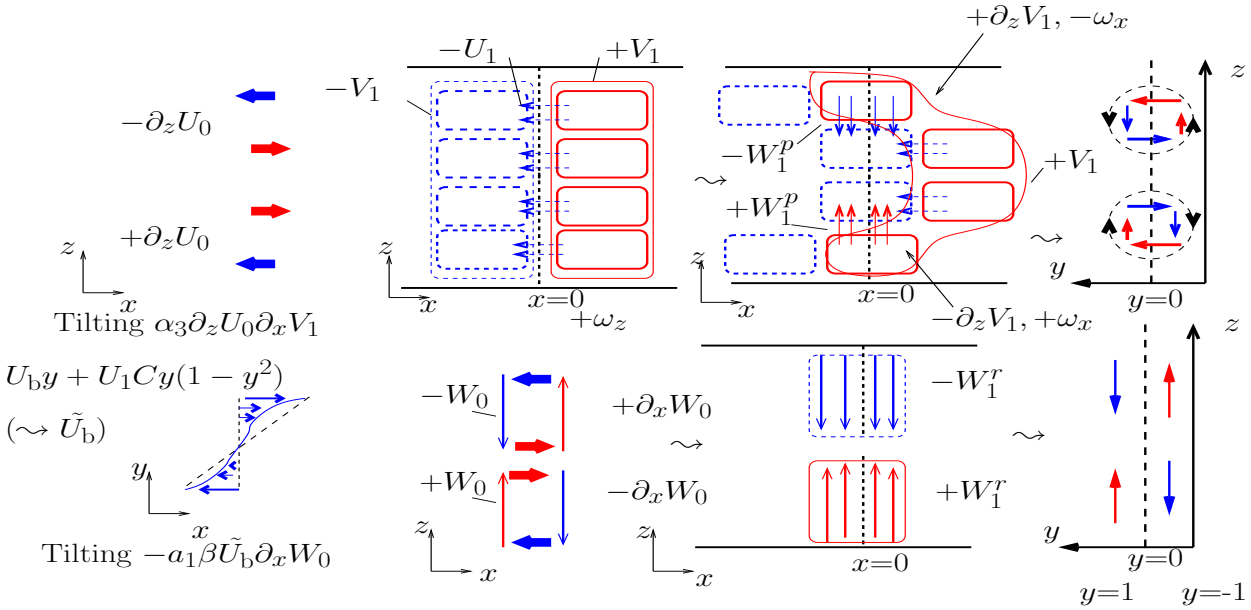

Figure 5.8: On the complementarity of the two tilting terms $\partial_z U_0 \partial_x V_1$ and $-\beta \tilde{U}_b \partial_x W_0$. Same convention as in Fig. 5.7. The two z-elongated patches of V_1 account for the spanwise vortex ($\omega_z \geq 0$) and $\partial_z U_0$ represents the spanwise shear associated with the key-structure. Only the half of the quadrupolar flow (U_0, W_0) is shown here. The velocity W_1^r has the same sign as W_1^p. Compare with Fig. 5.2 and Fig. 5.1. The resultant $\omega_x = \beta W_1 - \partial_z V_1$, with $W_1 = W_1^p + W_1^r$, represents an embryo of streamwise vortices, shown in the (y, z)-plane at $x = 0$.

the velocity potential Φ_1 might produce V_1. This is further discussed below.

The tilting term $-a_1 \beta \tilde{U}_b \partial_x W_0$ can be written as the sum of $-a_1 \beta U_b \partial_x W_0$ and $-\alpha_2 \beta U_1 \partial_x W_0$, since $\tilde{U}_b = U_b + \frac{\alpha_2}{a_1} U_1$. The first term $-a_1 \beta U_b \partial_x W_0$ is present in the equation of the stream-function Ψ_1 (Eq. 3.2), whereas it is absent in the equation of the potential velocity Φ_1 (Eq. 3.3). Hence, it only generates a spanwise velocity of rotational origin, $W_1 = \partial_x \Psi_1$.

The second term $-\alpha_2 \beta U_1 \partial_x W_0$ might produce V_1 since it is present in the equation for Φ_1 (in N_{W_1}). However, this term is a sink term in the equation of ω_x. In fact, the two terms $-\alpha_2 \beta U_1 \partial_x W_0$ and $-a_1 \beta U_b \partial_x W_0$ have opposite-signed distributions (U_1 is negative as inferred from Fig. 5.5 while $U_b = 1$), and since the latter has a same-signed distribution as the source term $-a_1 \beta \tilde{U}_b \partial_x W_0$ ($\tilde{U}_b \geq 0$), so the former is a sink term. Therefore, the tilting term $-a_1 \tilde{U}_b \partial_x W_0$ produces a spanwise velocity, noted W_1^r (the superscript "r" indicates its rotational origin) which forms two sheets of streamwise vorticity ω_x (and not streamwise vortices), as shown in Fig. 5.8 (compare also with Fig. 5.1). Consider now the second tilting term. As shown in Fig. 5.8, the tilting of the spanwise vorticity by positive (negative) $\partial_z U_0$ produces negative (positive) $\partial_z V_1$. To this z-dependent V_1 corre-

sponds a velocity potential Φ_1 and hence a spanwise velocity $W_1^p = \partial_z \Phi_1$, where the superscript "p" indicates its potential origin. Its distribution is obtained from the one of V_1 through the continuity equation ($\partial_z W_1^p \propto V_1$). The negative (positive) $\partial_z V_1$ together with positive (negative) W_1^p gives a positive (negative) patch of ω_x (compare also with Fig. 5.2). This W_1^p has a similar distribution that of W_1^r and this allows us to highlight the complementarity of the two tilting terms. The tilting of the spanwise vorticity ω_z into the streamwise direction provides the wall-normal velocity V_1 and its corresponding spanwise velocity W_1^p (of potential origin), whereas the tilting of the wall-normal vorticity only provides the spanwise velocity component W_1^r (of rotational origin). The two spanwise velocities have similar distributions and their sum, with the wall-normal velocity V_1, gives two adjacent patches of ω_x which is an embryo of streamwise vortices. Hence the two tilting terms play complementary roles in the generation of this embryo, as summarized in Fig. 5.8. In the next section, we study the growth of this embryo to streamwise vortices.

5.3.4 Nonlinear advection of ω_x by (U_0, W_0)

The vorticity ω_x shown in Fig. 5.4 consists of two regions of positive and negative values. Their subsequent evolution is given in Fig. 5.9: they become elongated in the x-direction and, as we will see later on, form two counter-rotating vortices. The mechanism by which the initial patches of ω_x become x-elongated is simply the nonlinear advection by the two-dimensional flow (U_0, W_0). By lumping together this mechanism with the mechanisms studied in the previous sub-sections, the two-time process: (1) tilting of vorticities and then (2) nonlinear advection of ω_x by (U_0, W_0), is called *deformation* of a spanwise vortex to two counter-rotating streamwise vortices. Two points must be considered regarding this process. The first point concerns the most suitable quantity to be studied in order to give a simple picture of the generation of streamwise vortices from spanwise vortices. The second point concerns the phase (2) of the process. Showing the nonlinear advection of ω_x by the flow (U_0, W_0) by considering the distribution of the advective terms at each time and studying their contributions to ω_x will generate a huge number of figures, similar to Fig. 5.10, and an alternative is presented below. Regarding the first point, this deformation is easily represented by the common quantity to both kinds of vortices (spanwise ($+\omega_z$) and streamwise vortices ($\pm\omega_x$)), which is the wall-normal velocity V_1. This velocity allows us to track the evolution of spanwise vortices to streamwise vortices, whereas this is not easy with ω_x and ω_z. Furthermore, the governing equation of V_1 is explicitly integrated in the numerical simulation (in fact, it is Eq. 3.3 since $\beta V_1 = \Delta_2 \Phi_1$), in contrast with Eq. 5.4 and Eq. 5.5 for ω_x and ω_z which are not integrated. Moreover, the presence of this wall-normal velocity V_1 guarantees that the vorticity, oriented in either the spanwise or streamwise directions, corresponds respectively to spanwise and streamwise vortices. Following the deformation of a spanwise

vortex to two counter-rotating streamwise vortices using the isocontours of V_1, is presented in §5.3.5, and shows some *crescent* structures similar to the one depicted in Fig. 5.8 with the red-line contour. The second point is studied in §5.4 using a set of partial differential equations of (x, t) governing the flow (U_0, W_0), the spanwise vortex and the streamwise vortices.

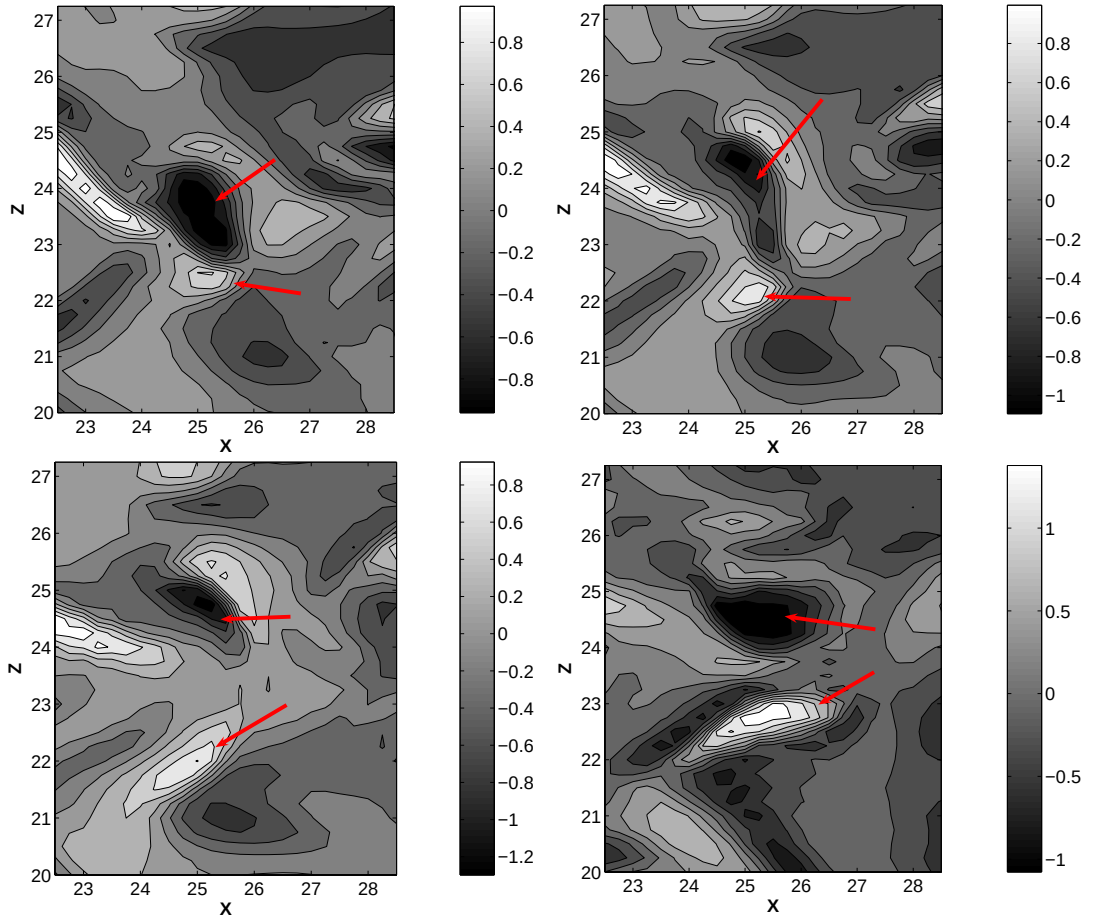

Figure 5.9: Sequence of figures showing the formation of streamwise vortices. The isocontours of the vorticity ω_x are reported. From left to right and top to bottom: (a) $t = 5$,(b) $t = 7$,(c) $t = 12$,(d) $t = 17$. The two patches with positive and negative values of ω_x are elongated in the streamwise direction and form two counter-rotating vortices.

5.3.5 From spanwise to streamwise vortices

Figure 5.11 displays the evolution of the spanwise vortex (shown in Fig. 5.5) using the velocity V_1. In each sub-figure, the total flow (U_0, W_0) is shown with vectors.

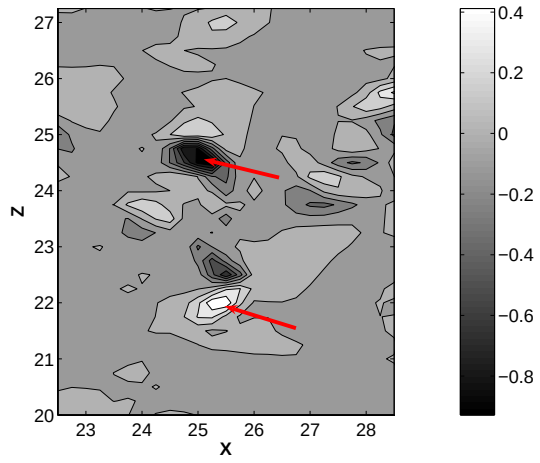

Figure 5.10: Spatial distribution of the term $-(U_0\partial_x . + W_0\partial_z .)\tilde{\omega}_x$ at $t = 5$.

From sub-figures (a) to (d), the isocontours of V_1 are *deformed*. From (c) to (d), the positive patches of V_1 are advected in the streamwise direction towards negative x and they both come closer. The last configuration is a *crescent* vortex shown in Fig. 5.12 together with the associated flow field (U_1, W_1). While the spanwise vortex represents its *head*, the two counter-rotating streamwise vortices form the *legs* of this crescent vortex and they regenerate the streaks by the lift-up effect. Regions with positive (negative) V_1 at $t = 17$ correspond to regions of negative (positive) U_0 (represented with horizontal vectors since $|U_0| \gg |W_0|$). Therefore, on each side of the legs, we have positive Reynolds stress $-U_0V_1$, as shown in Fig. 5.13. Hence, the streamwise vortices extract the energy from the base flow across the gap, as discussed in (75). By inspecting the full turbulent domain, we have found that the regions which make essential contributions to the production of energy are at both sides of the legs of the several crescent vortices. Also, we have found two kinds of crescent vortices, the first one already shown in Fig. 5.11 and the second one shown in Fig. 5.13. As attested to by Figure 5.14, the crescent vortices are numerous in the turbulent domain and can be observed by monitoring the wall-normal velocity V_1. Both kinds of crescent vortices can be easily depicted in this figure. They have roughly similar size ($\approx 2h$ in x and $3h$ in z) for different Reynolds numbers $R \in [180, 250]$.

A remark is worth making here. As shown in Fig. 5.15, the deformation of a spanwise vortex with $\omega_z \geq 0$ gives a crescent vortex (of either the first or the second kind) which regenerates the streaks, whereas the deformation of a spanwise vortex with $\omega_z \leq 0$ would give a crescent vortex which damps the streaks (anti

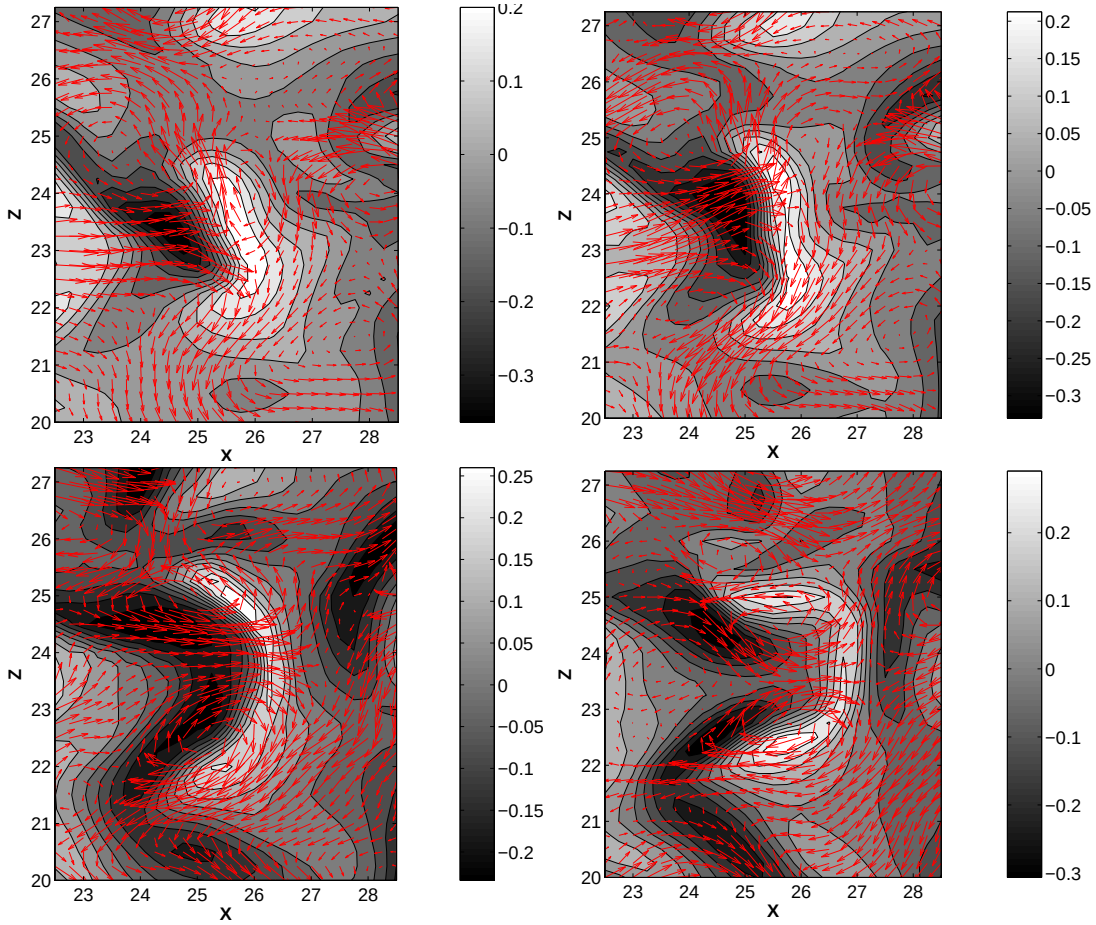

Figure 5.11: Sequence of figures showing the deformation of the spanwise vortex to a crescent vortex. From left to right and top to bottom: (a) $t = 5$, (b) $t = 7$, (c) $t = 12$, (d) $t = 17$. Wall-normal velocity V_1 in gray levels and the flow (U_0, W_0) is shown with red vectors. The two legs of the crescent vortex ($t = 17$) are x-elongated and form the streamwise vortices.

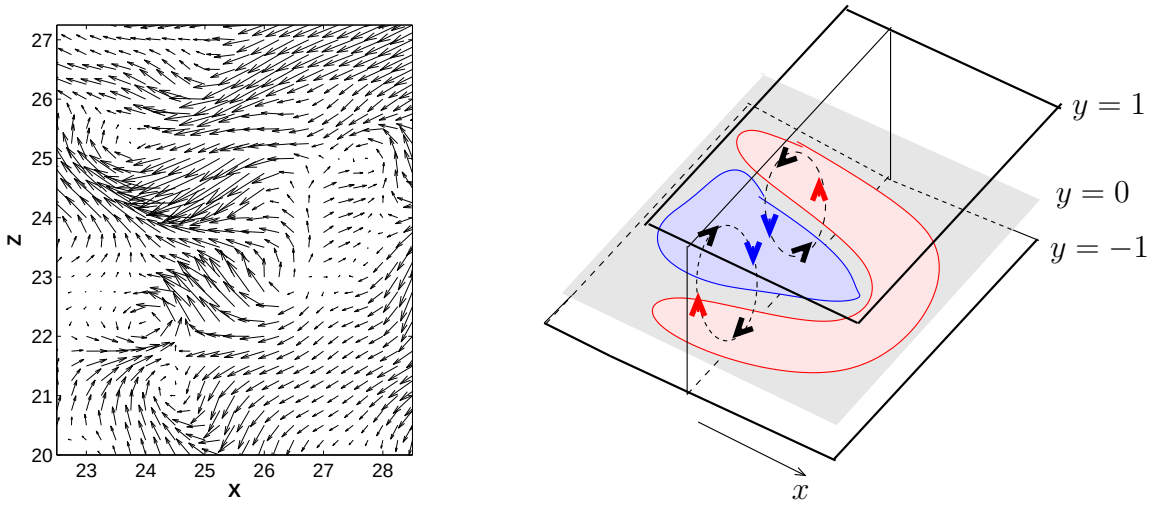

Figure 5.12: Left: The velocity (U_1, W_1) at $t = 17$. The corresponding V_1 is given in Fig. 5.11. The region dominated by positive (negative) W_1 represents a streamwise vortex. The $3D$ reconstruction of this flow represents a crescent vortex (right panel).

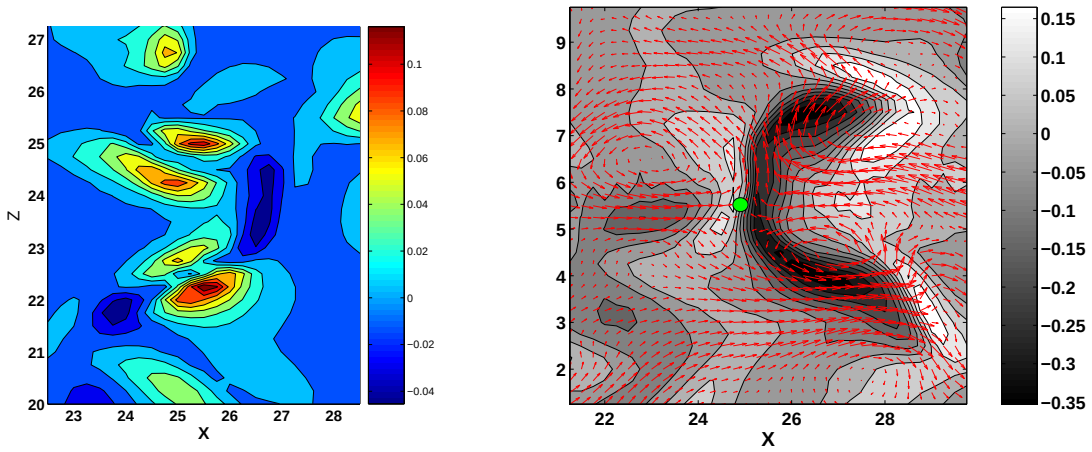

Figure 5.13: Left: The legs of the crescent vortex (Fig. 5.12) are two streamwise vortices. On each side of the vortex, there is a region of positive Reynolds stress $-U_0V_1$. Right: Second kind of crescent vortices. The velocity V_1 is depicted by its isocontours and the flow (U_0, W_0) is shown with vectors.

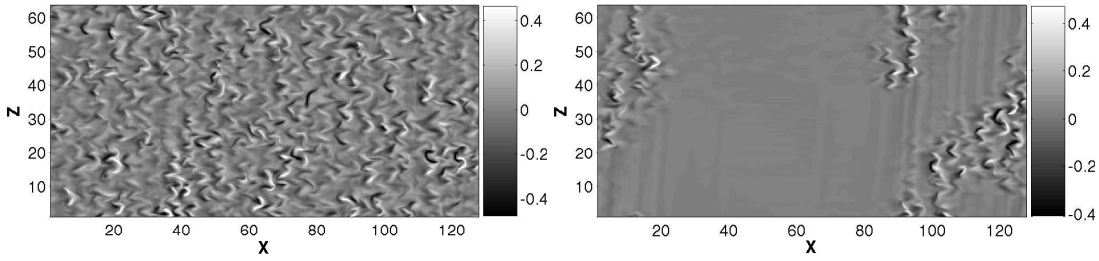

Figure 5.14: The crescent vortices are numerous in the turbulent domain, as attested to here by the spatial distribution of V_1 in a large numerical box with $L_x \times L_z = 128h \times 64h$. Left: for a sustained turbulent state with $R = 200 \geq R_g \sim 173$. Right: During the decay of the turbulent state where pockets of laminar flow nucleate and widen, $R = 168 \leq R_g$.

lift-up effect giving $-U_0 V_1 \leq 0$). Therefore, only spanwise vortices with $\omega_z \geq 0$, i.e. retrograde, are important in the self-sustainment of turbulence.

The question about which kind of crescent vortex will be generated by the deformation of a given spanwise vortex by a quadrupolar flow (U_0, W_0) relies on the symmetry of this flow. The study of such a point is more suitable in terms of ordinary differential equations and is presented in the next chapter.

Since the key-structure is at the origin of the generation of ω_x by the tilting mechanisms, its occurrence is now studied using some statistical tools.

5.3.6 Statistical tools

The occurrence of some events related to the key-structure can be measured by well defined quantities. First, since a retrograde spanwise vortex is characterized by a positive $\partial_x V_1$ and the stagnation point by a negative $\partial_x U_0$, the simple signature of the event leading to the generation of a crescent vortex is the positiveness of the (correlation) quantity:

$$\mathcal{A}(t) \equiv \overline{-\partial_x U_0 \partial_x V_1} > 0,$$

where the overline denotes the spatial average. Second, using the wall-normal vorticity $-\Delta_2 \Psi_0 = \partial_z U_0 - \partial_x W_0$ of the quadrupolar flow (U_0, W_0) and the streamwise vorticity ω_x, as shown in Fig. 5.7, the occurrence of such key-structure is confirmed by the positiveness of the quantity:

$$\mathcal{C}(t) \equiv \overline{(-\Delta_2 \Psi_0)\omega_x} > 0.$$

Furthermore, the streamwise vortices and the streaks are characterized by a spanwise gradient $\partial_z V_1$ and $\partial_z U_0$ respectively. Hence, the occurrence of the lift-up

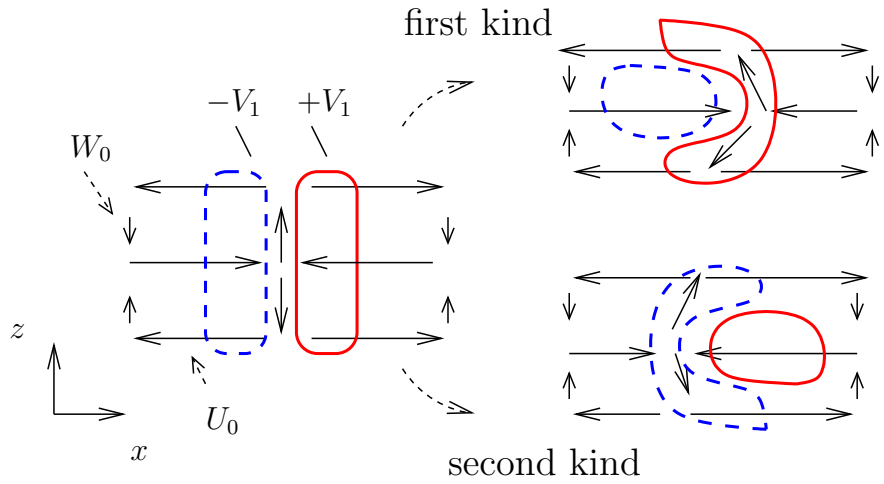

Figure 5.15: The deformation of a spanwise vortex (with $\omega_z \geq 0$) by a quadrupolar flow (U_0, W_0) can give one of the two kinds of crescent vortices. Same contour convention as in Fig. 5.7. For the first kind, both adjacent regions with opposite-signed ω_x on the left of the stagnation point in Fig. 5.7 are x-elongated (see also Fig. 5.9), whereas, for the second kind, both regions on the right of this point are x-elongated.

is attested to by the positiveness of the quantity

$$\mathcal{F}(t) \equiv \overline{-\partial_z V_1 \partial_z U_0} > 0.$$

Let us now quantify the contribution of a single crescent vortex to the total Reynolds stress $\mathcal{B} \equiv \overline{-U_0 V_1}$. If d denotes the surface of the sub-domain containing such vortex ($d \approx 3.5 \times 2.5$), so $\int_d -U_0 V_1 \, dxdz$ measures its contribution in terms of Reynolds stress. It follows that the quantity

$$\mathcal{B}' \equiv \mathcal{B} / \int_d -U_0 V_1 \, dxdz$$

is related to the "number" of crescent vortices in the whole domain. In the same way,

$$\mathcal{A}' \equiv \mathcal{A} / \int_d -\partial_x U_0 \partial_x V_1 \, dxdz$$

accounts for the number of occurrence of the event leading to the formation of the crescent vortex, as well as the quantities

$$\mathcal{C}' \equiv \mathcal{C} / \int_d (-\Delta_2 \Psi_0) \omega_x \, dxdz, \quad \mathcal{F}' \equiv \mathcal{F} / \int_d -\partial_z V_1 \partial_z U_0 \, dxdz.$$

Since all the quotients above are related to the same event, i.e. generation of a crescent vortex, it is interesting to verify that they give similar values or at

Table 5.1: Contribution of a single crescent vortex, for $R = 180$

Quantity	$\int_d -U_0 V_1 \, dxdz$	$\int_d -\partial_x U_0 \partial_x V_1 \, dxdz$	$\int_d -\partial_z U_0 \partial_z V_1 \, dxdz$	$\int_d (-\Delta_2 \Psi_0)\omega_x \, dxdz$
value	0.28± 0.05	0.25± 0.6	1.17 ± 0.12	2.53 ± 0.12

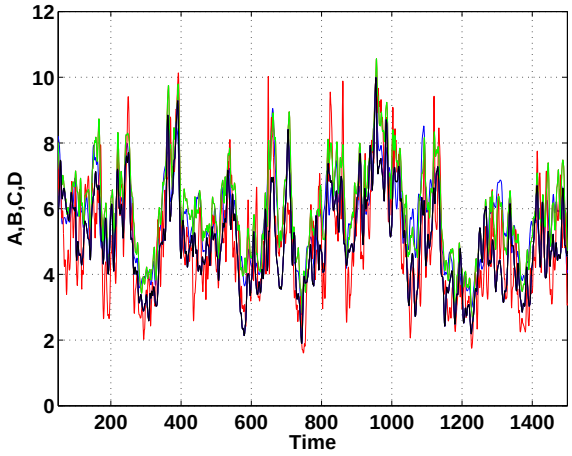

Figure 5.16: Some statistical tools. $R = 180$, $L_x \times L_z = 32 \times 32$. The rescaled quantities: $\mathcal{A}'$ in black, $\mathcal{B}'$ in red, $\mathcal{C}'$ in blue and $\mathcal{F}'$ in green. These quantities do not cancel and since they describe the same event (generation of a crescent vortex), so they are similar.

least that their time behaviors are similar. This is in fact the case, witnessed in Fig. 5.16 where the rescaled quantities (using Table 5.1) have similar time behaviors.

Many other events can be measured with more complicated quantities and tools, but the quantities considered here are sufficient to attest the frequently encountered key-structure.

5.3.7 Conclusions on the generation of streamwise vortices

The streamwise vortices are produced through a two-time process. First, adjacent regions of streamwise vorticity ω_x with opposite signs are generated by the tilting of the spanwise (wall-normal) vorticity into the x-direction by the shear $\partial_z U_0$ $(-\beta \tilde{U}_\mathrm{b})$. The contributions of these tilting terms are correlated due to a particular distribution of the velocity components, termed key-structure. Its fre-

quent occurrence was confirmed by some statistical tools (§5.3.6). Then in a second time, the nonlinear advection of ω_x by the flow field (U_0, W_0) results in two counter-rotating streamwise vortices. This two-time process is summarized as follows. A spanwise vortex with positive ω_z is deformed by the flow (U_0, W_0) and yields two counter-rotating streamwise vortices. Then, the tilting of the wall-normal vorticity by the corrected base flow intensifies the in-plane spanwise velocity associated with these streamwise vortices.

In the next two sections, we further illustrate (i) the generation of streamwise vortices with a simple model and (ii) study the generation of spanwise vortices.

5.4 From spanwise to streamwise vortices: an illustrative model

In this section, a model is derived to illustrate the deformation of a spanwise vortex into two counter-rotating streamwise vortices under the action of the flow (U_0, W_0).

5.4.1 Derivation

The field functions Ψ_0, Ψ_1 and Φ_1 are expanded onto a complete basis of z-dependent functions with x, t-dependent amplitudes. The equations of the no-slip model (3.1-3.3) are then projected onto this functional basis.

For the stream-function Ψ_0, we choose an odd expansion in z. With this choice, justified later on, the parity of the remaining functions Ψ_1 and Φ_1 is determined using the symmetries of the problem.

It follows that Ψ_0, Ψ_1 and Φ_1 have these Fourier expansions:

$$\begin{aligned}
\Psi_0 &= \sum_{n\geq 1} A_n(x,t)\sin(n\theta z),\\
\Psi_1 &= \sum_{n\geq 1} B_n(x,t)\sin(n\theta z),\\
\Phi_1 &= \sum_{n\geq 0} C_n(x,t)\cos(n\theta z),
\end{aligned}$$

where $\theta = 2\pi/L_z$ is the spanwise fundamental. A dipole (U_0, W_0) such as the one depicted in Fig. 5.11 (at $t = 17$) can be represented at the lowest order, by the first mode of the stream-function $\Psi_0(x, z, t) = A_1(x, t)\sin(\theta z)$, which changes its sign along the z-direction. Then, since the vorticity $\Delta_2\Psi_1$ is generated linearly by $\Delta_2\Psi_0$ through the linear term $-a_1 U_\mathrm{b}\partial_x\Delta_2\Psi_0$ in Eq. 3.2, the stream function Ψ_1 has to include the first mode too. Then, the first z-independent mode of Φ_1, C_0, represents a spanwise vortex characterized by $V_1 = \partial_{xx}C_0/\beta$ and $U_1 = \partial_x C_0$ (with $W_1 = 0$). The second mode $C_1\cos(\theta z)$ represents two

streamwise vortices where the corresponding wall-normal velocity reads $V_1 = \Delta_2\Phi_1/\beta = (\partial_{xx} - \theta^2)C_1\cos(\theta z)/\beta \propto \cos(\theta z)$. These streamwise vortices have the correct z-distribution and are able to regenerate the streaks $U_0 \equiv -\partial_z\Psi_0 = -A_1\theta\cos(\theta z) \propto \cos(\theta z)$. The sign of C_1 is determined by the dynamic and has to be examined later on. Hence, the expansions for the fields are:

$$\Psi_0 = A_1(x,t)\sin(\theta z), \quad \Psi_1 = B_1(x,t)\sin(\theta z), \quad \Phi_1 = C_0(x,t) + C_1(x,t)\cos(\theta z).$$

The projection gives the set of equations forming the illustrative model:

$$(\partial_t + R^{-1}(\delta_1 - \gamma_0))\delta_1 A_1 = -\delta_1 a_1(\tfrac{3}{2}\theta C_1 - \partial_x B_1) + TN^{A_1}, \tag{5.6}$$

$$(\partial_t + R^{-1}(\delta_1 - \gamma_1))\delta_1 B_1 = -a_1\delta_1\partial_x A_1 + TN^{B_1}, \tag{5.7}$$

$$(\partial_t + R^{-1}(\partial_{xx} - \beta^2))(\partial_{xx} - \beta^2)\partial_{xx}C_0 = \tfrac{\sqrt{15}}{2}\theta^2\partial_{xx}(A_1B_1) + TN^{C_0} + \gamma_6 R^{-1}\partial_{xx}C_0, \tag{5.8}$$

$$(\partial_t + R^{-1}(\delta_1 - \beta^2))(\delta_1 - \beta^2)\Delta_1 C_1 = \gamma_6 R^{-1}\delta_1 C_1 + \theta\sqrt{15}\left(\tfrac{5}{22}(\delta_1 - \tfrac{1}{4})(A_1\partial_{xxx}C_0) - \partial_x A_1\partial_{xx}C_0\right), \tag{5.9}$$

where $\delta_1 \equiv (\partial_{xx} - \theta^2)$, $a_1 = 1/\sqrt{7}$ and $\gamma_6 = 45/2$. The nonlinear terms TN^{A_1}, TN^{B_1} and TN^{C_0} are given in the appendix.

The only parameters of this model are the Reynolds number and θ. We choose $\theta = \pi$ so that the spanwise width of the streaks is of the same order as with the no-slip model (~ 1).

Our aim is to illustrate how a streak deforms a spanwise vortex to give streamwise vortices which in turn, regenerate the streak through the lift-up mechanism. Hence starting with a streak A_1 and a spanwise vortex C_0, we have to show that (i) the streamwise vortices C_1 are generated by the nonlinear action of the streaks on this spanwise vortex and (ii) that these streamwise vortices have the right sign, i.e. that they amplify the streaks (lift-up) instead of damping them (anti lift-up).

The first point (i) is easy to prove since the r.h.s. of the governing equation for C_1 contains the product of A_1 and C_0, which proves that the streamwise vortices C_1 are solely induced by the nonlinear action of A_1 on C_0. Then, this C_1 would regenerate the streaks by the lift-up term $-\delta_1 a_1 \frac{3}{2}\theta C_1$ if C_1 has the correct sign. The two points (i) and (ii) are further examined by means of numerical simulations.

5.4.2 Numerical integrations

For the initial condition, we take $A_1(x,0) = \frac{1}{2\sqrt{\sqrt{\pi}}}e^{-2(x-x_c)^2}$, $C_0(x,0) = (x - x_c)e^{(x-x_c)^2}/2$, $C_1 = B_1 = 0$ and $x_c = 4$. The streak $U_0 = -\theta A_1\cos(\theta z)$, associated with this A_1, is positive at $z = 1$ as seen in Fig. 5.17. The retrograde spanwise vortex, associated with C_0, is depicted in Fig. 5.17 by the wall-normal velocity componant V_1. It is also characterized by a z-elongated patch of positive vorticity

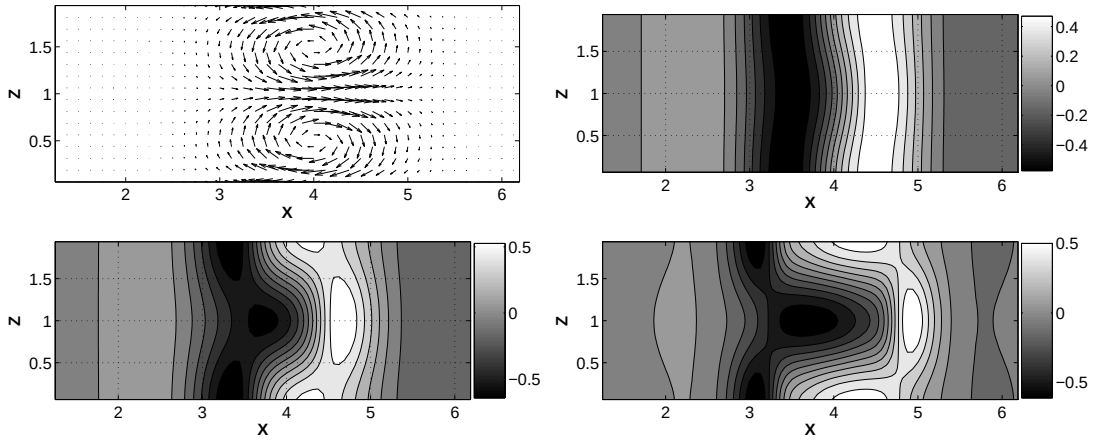

Figure 5.17: From left to right and top to bottom: the flow field (U_0, W_0) represented with vectors, V_1 at $t = 0.2$ at its subsequent evolution at $t = 1$ and $t = 6$. $R = 180$.

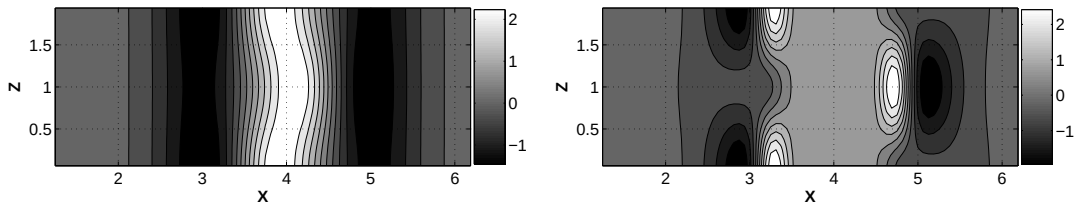

Figure 5.18: The isocontours of ω_z at $t = 0.2$ (left) and $t = 6$ (right). The spanwise vortex is characterized by a positive spanwise vorticity $\omega_z = \partial_x V_1 - \beta U_1$. The head of the crescent vortex (right panel) is a spanwise vortex, with $\omega_z \geq 0$.

ω_z, as shown in Fig. 5.18. The width of this spanwise vortex (~ 1) is close to the one observed in the numerical simulations.

As in the previous section, we follow the temporal evolution of the spanwise vortex using the velocity V_1. As displayed in Fig. 5.17, the contours of V_1 are deformed and result in a crescent contour. Together with the corresponding velocity field (U_1, W_1) given in Fig. 5.19 (left), this crescent contour is a crescent vortex. Its two legs are two counter-rotating vortices, represented by two x-elongated patches with opposite-signed ω_x depicted in Fig. 5.19 (right), whereas its head is a spanwise vortex with $\omega_z \geq 0$ as shown in Fig. 5.18.

It is easy to recover some results related to the tilting mechanisms. For instance, the generated ω_x given in Fig. 5.19 has a distribution similar to that of the term $\partial_z U_0 \partial_x V_1$, which passes from positive to negative values in the z-direction as inferred from the flow (U_0, W_0) and V_1 depicted in Fig. 5.17.

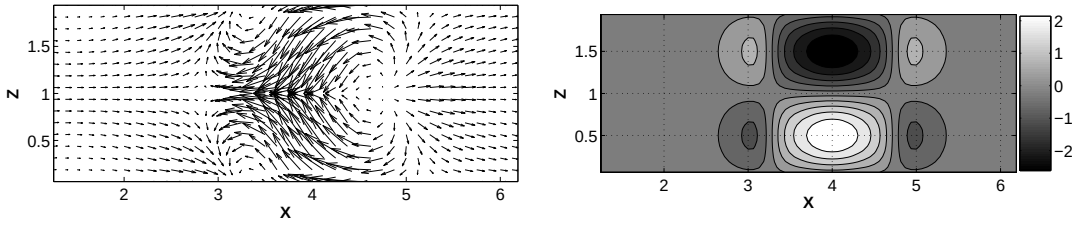

Figure 5.19: Left: the velocity field (U_1, W_1) at $t = 6$. Right: the isocontours of ω_x at t=6.

Regarding the role of the crescent vortex, it is clear from Fig. 5.17 that the positive (negative) x-elongated patches of V_1 correspond to the negative (positive) regions of U_0. Hence, on each side of the legs, we have positive Reynolds stress $-U_0V_1$: the streamwise vortices have the right sign and the lift-up feeds energy into the system.

As we stated in the previous section, the crescent vortices are essentially of two kinds. An example of generation for the first kind was already given in Fig. 5.17. By considering an initial condition with the same spanwise vortex ($\omega_z \geq 0$) as above but with a dipole (U_0, W_0) rotating in the opposite direction, $A_1 \to -A_1$, a crescent vortex of the second kind is generated. The corresponding ω_x and V_1 are obtained respectively from Fig. 5.19 and Fig. 5.17 by $((x - x_c), \omega_x) \to (-(x - x_c), -\omega_x)$ and $((x - x_c), V_1) \to (-(x - x_c), -V_1)$.

As a conclusion, the events leading to the formation of the streamwise vortices are well captured and explained by this illustrative model.

In the next section, the generation mechanism of the spanwise vortices is investigated. We can already note from the equations of the illustrative model, that the only source term for the spanwise vortex C_0 is the nonlinear term $\theta^2\partial_{xx}(A_1B_1)$ (when $C_0 = C_1 = 0$). Since A_1 and B_1 are the stream-functions of the in-plane flow, this source term shows that the spanwise vortex is generated from the nonlinear interactions of the in-plane flow components.

5.5 Generation mechanism for the spanwise vortices

5.5.1 Study of the spanwise vorticity equation

From §5.3.1, the governing equation for ω_z is:

$$\begin{aligned}\partial_t\omega_z &= \partial_x\partial_t V_1 - \beta\partial_t U_1 = \\ &= -\alpha_2(U_0\partial_x . + W_0\partial_z .)\tilde{\omega_z} + \beta(a_1U_b\partial_x U_0 + W_1\partial_z U_0) \\ &\quad -\beta''\beta V_1U_0 - \alpha_3\partial_x W_0\partial_z V_1 + \alpha_2\tilde{\omega_z}\partial_z W_0. \end{aligned} \tag{5.10}$$

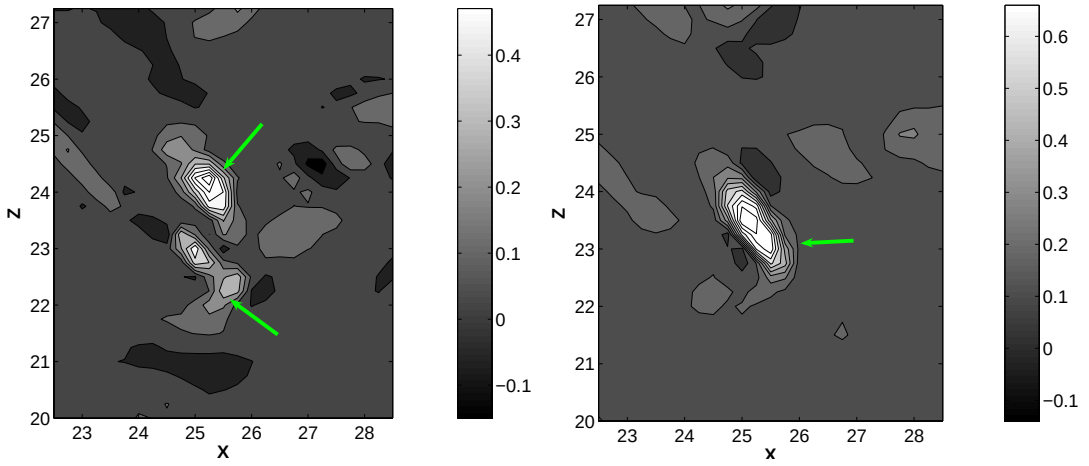

Figure 5.20: Spatial distribution of the advective term $-\alpha_2 W_0 \partial_z \tilde{\omega_z}$ (left) and the stretching term $\alpha_2 \tilde{\omega_z} \partial_z W_0$ (right) at $t = 5$.

As done for ω_x, we start by considering the contributions of some (dominant) terms in the equation of ω_z. The distributions of $-\alpha_2 W_0 \partial_z \tilde{\omega_z}$, $a_1 \beta U_\mathrm{b} \partial_x U_0$ and $\alpha_2 \tilde{\omega_z} \partial_z W_0$ are given in Fig. 5.20 and Fig. 5.21, while the distribution of ω_z was already given in Fig. 5.5. It is clear that $a_1 \beta U_\mathrm{b} \partial_x U_0$ is a sink term since it represents a region with negative values where ω_z is positive (this is obvious since near the stagnation point, $\partial_x U_0 \leq 0$ and $U_\mathrm{b} = 1$). In contrast, the stretching term $\alpha_2 \tilde{\omega_z} \partial_z W_0$ represents a region with positive values since $\partial_z W_0$ is positive near the stagnation point ($\partial_z W_0 = -\partial_x U_0 \geq 0$). This term intensifies ω_z. The behaviors of these two terms can be verified from a statistical point of view by showing that the temporal value of the spatial averaged $\overline{\omega_z (U_\mathrm{b} \partial_x U_0)}$ is negative whereas the value of $\overline{\omega_z (\tilde{\omega_z} \partial_z W_0)}$ is positive in the equation of $\overline{\omega_z^2}$.

Furthermore, due to the nonlinear advection by W_0, the patch of the spanwise vorticity is elongated in the z-direction ($-\alpha_2 W_0 \partial_z \tilde{\omega_z}$), as depicted in Fig. 5.20. Near the stagnation point, the contribution of this term vanishes ($W_0 \sim 0$), whereas the contribution of the stretching term $\alpha_2 \tilde{\omega_z} \partial_z W_0$ is maximal.

Despite this analysis of the main contributions to ω_z, it is difficult to understand the generation of the spanwise vortices which are characterized, in particular, by the wall-normal velocity V_1. In fact, the spanwise vorticity can be written as $\omega_z = \partial_x V_1 - \beta U_1 = \omega_z^p + \omega_z^r$, where the first part is of potential origin $\omega_z^p = \partial_x V_1 - \beta U_1^p$ and the other part is of rotational origin $\omega_z^r = -\beta U_1^r$. The presence of a spanwise vortex implies a non-zero ω_z^p since ω_z^r represents sheets of vorticity and not vortices.

The study of the equation of ω_z enables us, however, to identify the terms which play an important role in the generation of z-elongated region of ω_z^p and which are not zero when V_1 is zero. The first term is $-\alpha_2 U_1 \partial_z W_0$ and comes

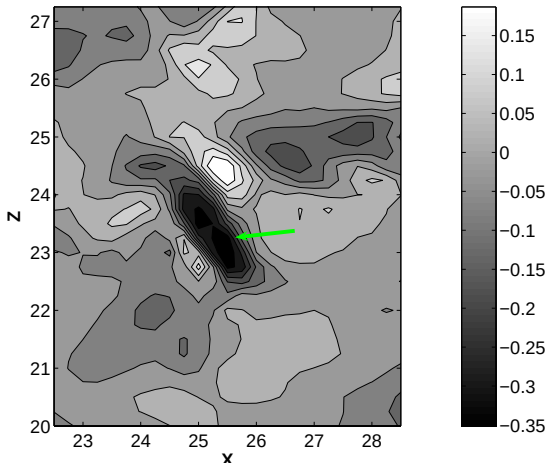

Figure 5.21: Spatial distribution of the sink term $\beta a_1 U_\mathrm{b} \partial_x U_0$.

from the stretching term $\alpha_2 \tilde{\omega_z} \partial_z W_0$. The second term is $\alpha_2 W_0 \partial_z U_1$ and comes from $-\alpha_2 W_0 \partial_z \tilde{\omega_z}$. These two terms are present in the nonlinear term N_{U_1} in the equation governing U_1. Their roles in the generation of spanwise vortices are summarized as follows. An initial localized region of negative U_1 of rotational origin (i.e., without V_1) is intensified and stretched along the spanwise direction by these two terms. Then to this z-elongated region of U_1, a wall-normal velocity V_1 is induced by the pressure to satisfy the continuity equation and hence a spanwise vortex is generated (and characterized by $\omega_z^p \geq 0$). To prove this mechanism, we have to show that these two terms are source terms for (a positive) ω_z^p which reads:

$$\beta \omega_z^p = \partial_x \beta V_1 - \beta^2 U_1^p = (\Delta_2 - \beta^2) \partial_x \Phi_1,$$

since $\beta V_1 = \Delta_2 \Phi_1$ and $U_1^p = \partial_x \Phi_1$. Then, using the equation of Φ_1 (3.3) which reads (without dissipative terms):

$$\partial_t (\Delta_2 - \beta^2) \Delta_2 \Phi_1 = \beta^2 (\partial_x N_{U_1} + \partial_z N_{W_1}) - \beta \Delta_2 N_{V_1},$$

and deriving it w.r.t x and considering in the r.h.s only the two nonlinear terms in N_{U_1} with which we are concerned, yields the equation for ω_z^p:

$$\partial_t \Delta_2 \omega_z^p = \beta^2 \alpha_2 \partial_{xx} (-U_1 \partial_z W_0 + W_0 \partial_z U_1).$$

This equation shows the generation of ω_z^p through the nonlinear interaction of the rotational flow (U_0, W_0) and the rotational part of the flow (U_1, W_1), noted (U_1^r, W_1^r), and can be written as:

$$\partial_t \Delta_2 \omega_z^p = \beta^2 \alpha_2 \partial_{xx} (-U_1^r \partial_z W_0 + W_0 \partial_z U_1^r).$$

This fact is also supported by Eq.5.8 since the amplitude C_0 of the spanwise vortex attains a finite value, when starting from a flow with no wall-normal velocity ($C_0 = C_1 = 0$ thus is $V_1 = 0$), thanks to the nonlinear term $A_1 B_1$, where A_1 and B_1 represent respectively the stream function of the rotational flow (U_0, W_0) and the rotational part of the flow (U_1, W_1).

To gain some insight into the distribution of the generated ω_z^p from the equation above, we have to further simplify the equation above (by dropping Δ_2 and ∂_{xx}). At first approximation, we can suppose that ω_z^p is slowly z-varying, hence the gradient in the z-direction is smaller than the gradient in the x-direction which yields $\Delta_2 \omega_z^p \approx \partial_{xx} \omega_z^p$, and we get:

$$\partial_t \partial_{xx} \omega_z^p \approx \beta^2 \alpha_2 \partial_{xx} (-U_1^r \partial_z W_0 + W_0 \partial_z U_1^r).$$

Then simplifying the x-derivative yields:

$$\partial_t \omega_z^p \approx \beta^2 \alpha_2 (-U_1^r \partial_z W_0 + W_0 \partial_z U_1^r).$$

As shown in Fig. 5.22, the r.h.s. of this equation has, around the stagnation point, a positive and z-elongated distribution. Thus the resultant ω_z^p consists of a positive patch.

Therefore the potential part of the vorticity, ω_z^p, is generated through the nonlinear interactions between a correction of rotational origin ($U_1^r \leq 0$) to the base flow and a quadrupolar flow (U_0, W_0).

5.5.2 Generation of the quadrupolar flow (U_0, W_0)

We consider now the generation of this quadrupolar flow (U_0, W_0), characterized by a stream function Ψ_0. We will see that in addition to the lift-up, the streaks U_0 can be generated by another mechanism, which does not necessitate a wall-normal motion. Hence, streaks can exist without streamwise vortices, as noted by (90).

This mechanism is linear and is driven by the term $-U_\mathrm{b} \partial_x U_1$ in the U_0-equation. Consider, as initial condition, a localized region of negative $U_1^r \leq 0$ located at $(x_\mathrm{c}, z_\mathrm{c})$. For $x \leq x_\mathrm{c}$, ($x \geq x_\mathrm{c}$) $\partial_x U_1^r$ is negative (positive) and hence the generated U_0 is positive (negative), according to $\partial_t U_0 \sim -U_\mathrm{b} \partial_x U_1$. This distribution of the induced U_0 points out its inflow character. It has a stagnation point ($U_0 \approx 0$ and $\partial_x U_0 \leq 0$) located at $(x_\mathrm{c}, z_\mathrm{c})$.

This linear source term comes from the Galerkin projection of the term $-U_\mathrm{b} y \partial_x U_1 R_1(y)$ in the equation of $U_0 R_0(y)$. It represents the generation of $U_0 R_0$ through the shearing of $U_1 R_1(y)$ by the base flow $U_\mathrm{b} y$. Hence, the inflow U_0 and its characteristic stagnation point are the consequences of the shearing by the base flow of the localized region of negative U_1. The outflow W_0 derives from the continuity equation $\partial_x U_0 + \partial_z W_0 = 0$.

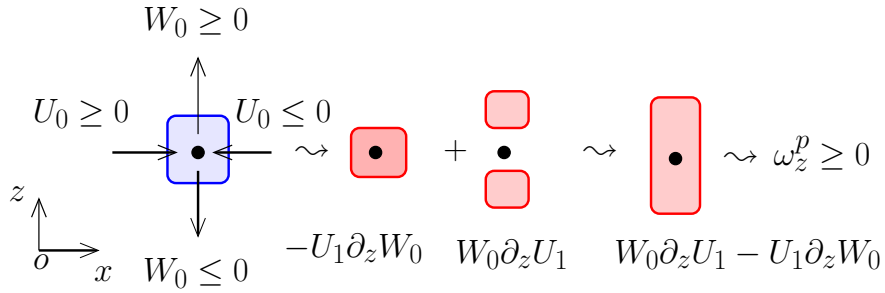

Figure 5.22: Generation of the spanwise vorticity ω_z^p. Consider a localized region of negative $U_1 (= U_1^r)$ with the inflow U_0 and outflow W_0. Based on this velocity distribution, the contributions of both terms $-U_1\partial_z W_0$ and $W_0\partial_z U_1$ result in a positive and z-elongated region. The resultant ω_z^p is a z-elongated patch with positive values. See also Fig. 5.20. Solid-red (dashed-blue) contours indicate positive (negative) values.

Similar generation of the quadrupolar flow (U_0, W_0) by this linear mechanism has been encountered in Chapter 2, where the shearing of the large-scale component of the correction to the base flow, U_1, by the base flow U_b, gives the large-scale inflow U_0 with a stagnation point at the center of the spot. Here the same mechanism does apply but with small-scale structures.

A more physical intepretation to this mechanism as well as the role of the different terms in the U_0-equation will be discussed later.

5.5.3 Generation of the spanwise vortex

The different steps in the generation process of spanwise vortices are given in Fig. 5.23 and discussed as follows. Consider a localized region of negative $U_1 = U_1^r$, which represents a correction of rotational origin to the base flow. The base flow shears this U_1^r and generates the inflow U_0 with its characteristic stagnation point ($U_0 \approx 0$ and $\partial_x U_0 \leq 0$ at the center of the region of U_1^r). Then, according to the continuity equation, an outflow W_0 is induced with $\partial_z W_0 = -\partial_x U_0 \geq 0$ at the center of the region of U_1^r.

Under the action of this outflow W_0, the distribution of U_1 is intensified and elongated into the z-direction, thanks to the generation of the potential part U_1^p by the two terms $-U_1^r\partial_z W_0$ and $W_0\partial_z U_1^r$ and is given now by the sum $U_1 = U_1^r + U_1^p$. The distribution of the flow associated with this U_1 depends on the wall-normal coordinate y and is given by $U_1 R_1(y)$. Since U_1 is negative, we have a flow towards negative x for positive y and conversely, for negative y, the flow is towards positive x. Due to incompressibility, this flow escapes towards negative y and in the other half space, the fluid escapes towards positive y. This wall-normal escaping motion generates the velocity V_1.

This is nicely supported by the V_1-equation since all the terms in its r.h.s

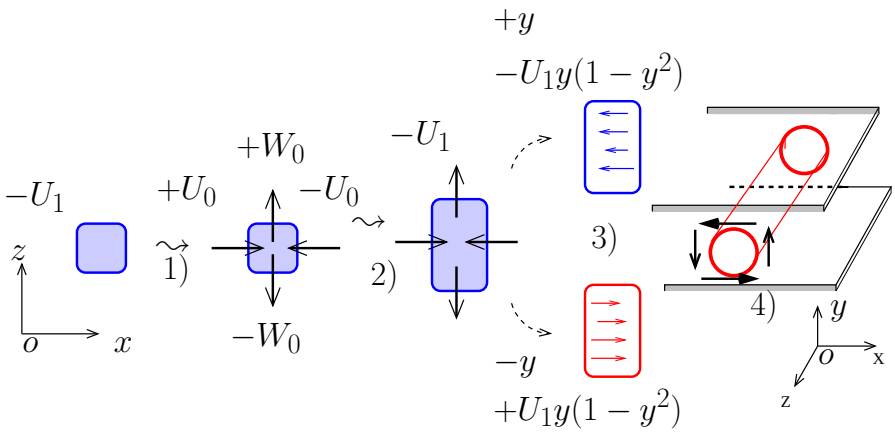

Figure 5.23: Generation of a retrograde spanwise vortex. Consider a localized region of negative U_1 of rotational origin. The base flow shears this velocity and generates U_0 with its characteristic stagnation point and the spanwise outflow $\partial_z W_0 \geq 0$ (1). This spanwise velocity intensifies (by the term $-U_1 \partial_z W_0$) the velocity U_1 and elongates (by the term $W_0 \partial_z U_1$) its region in the spanwise direction (2). To this z-elongated region of U_1, with its y-reconstruction given in sub-figure (3), a wall-normal velocity V_1 is generated. The resultant retrograde spanwise vortex in shown in (4). Positive (negative) quantities are marked with "+"(-).

vanish when $V_1 = 0$ except the pressure term P_1, the role of which is to assure the incompressibility of the flow. Hence, from the in-plane motion (U_0, W_0, U_1^r, W_1^r), a wall-normal velocity V_1 (associated with the spanwise vortex) emerges due to the pressure.

Note finally that we were concerned in this study with some terms which play an important role in the generation of a spanwise vortex (especially $-U_1 \partial_z W_0$ and $W_0 \partial_z U_1$). For example, the term $U_0 \partial_x U_1$ which compresses the initial region of U_1 in the x-direction was deliberately omitted (to simplify the presentation) and only the related term $W_0 \partial_z U_1$, which elongates this region in z, is studied.

Further details which are necessary for the study of the self-sustained mechanisms (see below), as the size of the initial patch of U_1, the spanwise streaks spacing, and the size of the generated spanwise vortex, will be given later.

5.6 Discussion and conclusion

The main question that was addressed in this chapter concerns the generation mechanism for streamwise vortices. By analyzing each term contributing to the generation of the streamwise vorticity in the physical space and tracking the evolution of this vorticity into streamwise vortices in time, we have found a process for streamwise vortices generation where the flow field (U_0, W_0) related to

the streaks (represented by the velocity component U_0) plays a crucial role. This process is summarized as follows. A retrograde spanwise vortex is deformed by the flow (U_0, W_0) and gives a crescent vortex where its legs are two counter-rotating vortices. Then, the tilting of the wall-normal vorticity by the corrected base flow intensifies the in-plane spanwise velocity associated with these streamwise vortices. They regenerate the streaks by the lift-up effect.

Then, we derived an illustrative model in terms of four PDEs, showing the generation of streamwise vortices from spanwise vortices. In the last part of this chapter, a mechanism for the generation of spanwise vortices was presented. Under the action of the flow field (U_0, W_0), a localized region of streamwise velocity correction, represented in the model by $U_1 \leq 0$, is intensified and stretched in the spanwise direction under the action of W_0 (where $\partial_z W_0 = -\partial_x U_0 \geq 0$). To this z-elongated region, a wall-normal velocity is generated by the pressure to satisfy the continuity equation. This wall-normal velocity and the z-elongated region of U_1 form the spanwise vortex.

Our results leave one with a rather different understanding of the mechanisms of streamwise vortices formation to what might have been inferred from other works. In some previous studies, direct numerical simulations of a highly constrained plane Couette flow and plane Poiseuille flow were used by minimizing the lateral dimensions of the domain or by externally imposing a streaky flow with a chosen analytical form.

Hamilton *et. al* (36) stressed on the fact that studies have to be made in unconstrained turbulent flows and that comparisons are needed to conclusively comment on any generation mechanisms and their occurence in real turbulent flow.

The works of (56; 101) (among others) as well as the present work are examples of such studies. In fact, in our simulations, no constraints were imposed. The flow was free to evolve in an extended domain and no perturbation with particular shape was externally imposed to this flow. The coherent structures were free to move and we obtained rich spatiotemporal dynamic.

The main difference with the turbulent flow in the experiments is the low y-resolution. But near the stability threshold R_{g}, this low resolution is justified based on (i) the experimental observations (large coherent structures spanning all the gap, e.g. Bottin *et al.* (13)) and (ii) the fact that all the dynamics elucidated in the present study (flow structures as well as the mechanisms) still hold when we increase the y-resolution in both free-slip and no-slip cases. The derivation procedure of models with higher y-resolution in the free-slip case (involving harmonic functions) is straightforward and is detailed in (64). In the appendix, we give a glimpse on the derivation of higher y-resolution models for the no-slip case.

Although we will not undertake a detailed comparison here, we will present some points found with our model and revealing a close correspondence to well-known instantaneous experimental events. One has to keep in mind, however, that we will extend the analysis beyond the case of pCf and consider other shear

flows, better documented in the literature. Hence, we have to be careful in comparing the present results with others due to their similarity. For instance, the question whether the crescent vortices are the representation in the case of pCf of the well-known hairpin vortices, needs a complete study to account for their possible relationship, despite the fact that they share several common features. If it is the case, the present model will constitute an ideal tool for studying such vortices and giving insight into some of the several proposed mechanisms for their generation (e.g., see the recent work of Heist *et al.* (2000)(43)).

Furthermore, the stagnation points ($U_0 \approx 0$ and $\partial_x U_0 \leq 0$) found in the present study, agree well with experimental events. Note first that in the half-space $y \geq 0$, positive U_0 represents a high-speed streak since $U(y) + U_0 R_0(y) \geq U(y)$ and that negative U_0 represents a low-speed streak since $U(y) + U_0 R_0(y) \leq U(y)$. In the half-space $y \leq 0$, the situation is reversed. We have shown that these stagnation points play important role in the generation of the spanwise vortices (and then streamwise vortices).

Bogard & Tiederman (10) have also shown that the stagnation points are important because they are associated with the regions containing high Reynolds stress production. They discussed their physical origin and according to these authors, they are a straightforward kinematic consequence of the impact of a high-speed streak on the back of a low-speed streak. Quoting (10), when a low-speed fluid is lifted away from the wall by the streamwise vortices, it will represent an obstacle onto which the high-speed fluid will impact and then flow around. This would cause the impingement point—termed in the present chapter a stagnation point—and produces a shear layer with high (negative) velocity gradient in the streamwise direction. These shear layers are another important feature of the wall-bounded turbulence and they have been shown to be related to the turbulence production in fully turbulent flow at low Reynolds numbers (e.g.(8)) as well as inside localized region of turbulence (e.g. (41)). In addition to the negative streamwise gradient $\partial_x u$, they are characterized by a positive $\partial_x v$ (e.g. see Figure 12 in (8)), which is in fair agreement with our finding $\partial_x V_1 \geq 0$.

As we have already mentioned, Schoppa & Hussain (90) have shown that the streamwise velocity gradient (but positive $\partial_x u$) plays an important role in the generation of streamwise vortices (stretching term $\Omega_x \partial_x u$) and that it is a consequence of the streak waviness induced by a sinuous instability.

In our study, we have shown that (i) the origin of this gradient is the linear shearing of the correction to the base flow (the velocity U_1) by the base flow itself (§5.5.2) which gives a negative $\partial_x U_0$ and that (ii) the origin of the positive $\partial_x V_1$ is the retrograde spanwise vortex.

Furthermore, by measuring the statistical properties of the vorticity field in boundary layer flow, Balint *et al.* (4) found that the stretching of the spanwise vorticity in the spanwise direction, due to a positive $\partial_z w$, is more frequent than compression. According to Antonia & Kim (2), it is plausible to assume that this $\partial_z w$ is the result of a wallward moving fluid which, on encountering the wall,

is deviated in both positive and negative z-directions. In the present study, the spanwise vorticity is also stretched in the z-direction (rather than compressed) due to the positiveness of $\partial_z W_0$, which is related, however, to the stagnation points events ($\partial_z W_0 = -\partial_x U_0 \geq 0$).

Hence, there is an agreement between the shear layer structure observed in turbulent flows and the key-structure studied in this chapter. Both represent *islands* where the turbulence is being produced.

Finally, the present study prompts us to consider the self-sustainment of the turbulence. By piecing together the mechanisms described in this chapter, a self-sustained process for wall-bounded turbulence can be proposed. In fact, we have studied two sequences of events. The first sequence deals with the generation of a spanwise vortex and the second sequence concerns its subsequent evolution, i.e. its deformation into a crescent vortex and the generation of streamwise vortices. To present a complete self-sustained process, it suffices to link between the last point, the streaks regenerated by lift-up, and the first point, the localized region of negative U_1. Once the streak is amplified by the streamwise vortices, it is sheared by the base flow U_b and generates U_1, according to the term $-a_1 U_\mathrm{b} \partial_x U_0$ in the U_1-equation. Regions of negative U_1 nucleate at the leading edge of a low speed streak ($U_0 \leq 0$) and at the trailing edge of a high speed streak ($U_0 \geq 0$). In these regions, spanwise vortices are then generated and the cycle restarts. Hence, the immediate next step is to formulate this cycle in terms of a set of ordinary differential equations (ODEs). Such ODEs model provides an ideal system for studying the interplay between the streaks, the correction to the base flow and the different types of vortices.

Appendix A: nonlinear terms of the illustrative model

The nonlinear terms TN^{A_1}, TN^{B_1} and TN^{C_0} read:

$$
\begin{aligned}
TN^{A_1} &= \tfrac{\sqrt{15}}{4}(\theta(\theta^2 C_1\partial_x C_0 + C_1\partial_{xxx}C_0 - \partial_{xx}C_1\partial_x C_0) - \partial_x B_1\partial_{xxx}C_0) \\
&+ \sqrt{\tfrac{5}{12}}((\theta^2(\partial_x B_1\partial_x C_0 + \tfrac{5}{2}B_1\partial_{xx}C_0) - (\partial_{xxx}B_1\partial_x C_0 + \tfrac{5}{2}\partial_{xx}B_1\partial_{xx}C_0))) \\
TN^{B_1} &= \tfrac{3\sqrt{5}}{4}(\theta^2(\partial_x(A_1\partial_x C_0) + \partial_x A_1\partial_x C_0) + \partial_x(\partial_x A_1\partial_{xx}C_0) - 2\partial_x(\partial_{xx}A_1\partial_x C_0)), \\
TN^{C_0} &= -\tfrac{\sqrt{15}}{8}(3\theta^3\partial_x(A_1C_1) + \theta(A_1\partial_{xxx}C_1 + 5\partial_x A_1\partial_{xx}C_1) + 4\theta\partial_{xx}A_1\partial_x C_1) \\
&\quad -\tfrac{5}{44}\sqrt{15}\theta(\theta^2\partial_{xxx}(A_1C_1) - \partial_x(\partial_x A_1\partial_{xxx}C_1) \\
&\quad -(A_1\partial_{xxxxx}C_1) + \partial_{xxx}A_1\partial_{xx}C_1).
\end{aligned}
$$

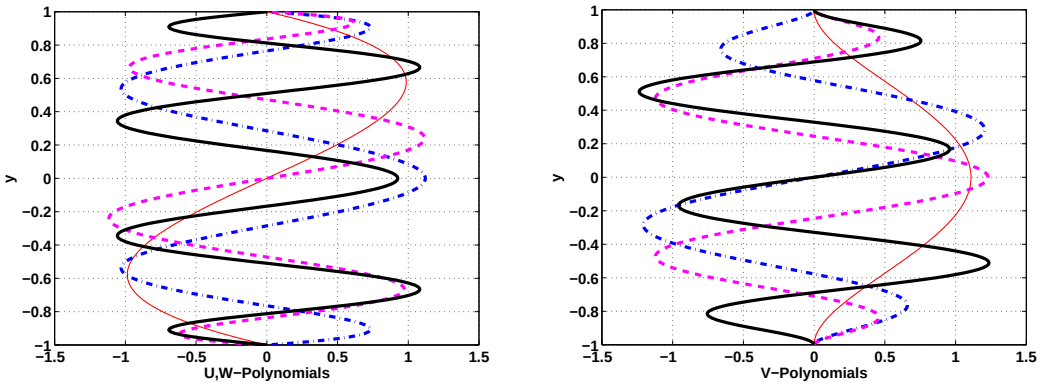

Figure 5.24: Right: polynomials for (u, w), R_1 in thin red-line, R_2 in dash-dotted blue, R_3 in dashed magenta and R_4 in solid-black. Left: polynomials for v, S_1 in thin red-line, S_2 in dash-dotted blue, S_3 in dashed magenta and S_4 in solid-black.

Appendix B: Higher order no-slip models

The y-resolution of the no-slip model is increased by further including y-polynomials. The Gram-Schmidt orthogonalization is used to construct an orthogonal basis of such polynomials. We give here the expansions of the velocities truncated at the order 4.

$$\begin{aligned} v &= V_1 S_1 + V_2 S_2 + V_3 S_3 + V_4 S_4, \\ u &= U_0 R_0 + U_1 R_1 + U_2 R_2 + U_3 R_3 + U_4 R_4, \end{aligned}$$

with the same expansion for the spanwise velocity w as u. The orthonormal polynomials, plotted in Fig. 5.24, read:

$$\begin{aligned} S_2(y) &= A_2 y(1 - a_2 y^2)(1 - y^2)^2, \\ S_3(y) &= A_3(1 + a_3 y^2)(1 + b_3 y^2)(1 - y^2)^2, \\ S_4(y) &= A_4 y(a_4^2 - y^2)(b_4^2 - y^2)(a_5^2 - y^2)(1 - y^2)^2, \\ R_2(y) &= B_2(1 - y^2)(1 - 14y^2 + 21y^4), \\ R_3(y) &= B_3 y(1 - y^2)(7.2494 - 42.84y^2 + 46.41y^4), \\ R_4(y) &= B_4(1.14 - y^2)(1 - y^2)(0.66 - y^2)(0.028 - y^2)(0.26 - y^2), \end{aligned}$$

with $a_2 = 3$, $b_3 = -16.6312$, $a_3 = -1.9842$, $a_4 = 0.3288$, $b_4 = 1.0968$, $a_5 = 0.6880$ and the A_i, and B_i are normalization constants. As illustrated in Fig. 5.25, most of the perturbation kinetic energy

$$E_{\text{tot}} \equiv \tfrac{1}{2}\int_V u^2{+}v^2{+}w^2\, dV = \tfrac{1}{2}\int_{xz} (U_0^2{+}W_0^2)\, dxdz + \sum_{k=1..4} \tfrac{1}{2}\int_{xz} (U_k^2{+}V_k^2{+}W_k^2)\, dxdz,$$

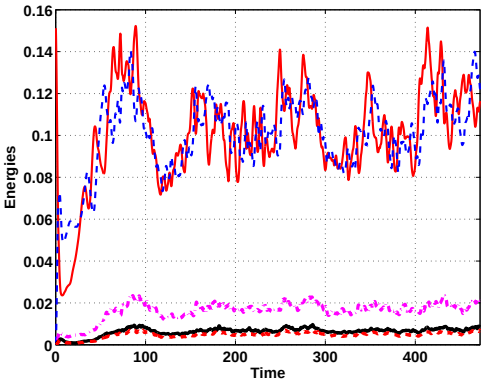

Figure 5.25: Energies contained in the modes, E_0 in red-solid, E_1 in blue-dashed, E_2 in magenta-dotted, E_3 in black-solid, E_4 in red-dashed. $E_0 \sim E_1 > E_2 > E_3 > E_4$. Most of the energy is contained in the two first modes, i.e $k = 0$ (U_0, W_0) and $k = 1$ (U_1, W_1, V_1). $R = 250$ and $L_x \times L_z = 32 \times 32$.

is contained in the two first modes, i.e $k = 0$ (U_0, W_0) and $k = 1$ (U_1, W_1, V_1), constituting precisely the no-slip model studied in the present chapter.

Chapter 6

Spreading mechanism

abstract

In this chapter we study the spreading mechanism of turbulent spots in plane Couette flow, where fluid is sheared between two parallel plates moving in opposite directions. The analysis of the coherent structures on the border between the laminar and turbulent regions reveals the existence of many vortices with wall-normal axes occupying the full gap between the plates. The streamwise component of the velocity field of these vortices are the streaks. Due to their self-advection, these vortices move parallel to the plates. During their motions, they carry the other perturbation components such as the streamwise and spanwise vortices.

6.1 Introduction

Plane Couette flow (pCf), shear flow between two parallel plates moving in opposite directions with velocities $\pm U_{\mathrm{p}}$, experiences a transition to turbulence marked by the nucleation and growth of *turbulent spots*, *i.e.* patches of turbulent flow scattered amidst laminar flow and separated from it by well defined fronts (e.g.(23)).

This transition is not restricted to the pCf case but also occurs in other shear flows with great practical interest, such as plane Poiseuille (16) and boundary layer flows (33). Despite a large body of numerical (61; 91; 53) and laboratory (98; 99; 22; 13) experiments, many questions regarding such transition remain unanswered, such as the mechanisms involved in the growth of turbulent spots (64; 69).

Based on experiments in boundary layer flow, Gad-El-Hak *et al.* (33) proposed a mechanism called growth by destabilization. The spot was observed to travel with a lower velocity than the surrounding flow. Hence it acts as a blockage and the laminar flow field on the outskirts of this spot is accelerated. The base flow as well as its linear stability property are modified and the growth of infinitesimal perturbations occurs.

Dauchot & Daviaud (23) discussed this mechanism in an experimental study of the pCf. Externally applied perturbations that trigger turbulent spots were made by injecting turbulent jets into the laminar flow. They found velocity profiles indicating that the flow is accelerated outside the spot, supporting the mechanism of (33). But a direct demonstration of this mechanism has not yet appeared.

Tillmark (99) experimentally analyzed the flow field in the vicinity of the spot in the pCf. He found that, in the spanwise direction, the spot forces the fluid outwards, giving rise to a spanwise outflow filling all the gap between the two plates. The flow outside the spot is hence modified and he suggested that the spanwise growth of turbulent spots can be due to the destabilization mechanism of Gad-El-Hak *et al.* (33). In the numerical study of Schumacher & Eckhardt (91), a more complete picture of the flow on the outskirts of the spot was given. In addition to the spanwise outflow observed in (99), they found a streamwise inflow towards the spot. They argued that the flow outside the spot plays an important role in the spreading of the spot. They stressed the fact, however, that this spreading is driven by a nonlinear mechanism.

In their experimental investigations of the dynamics of spots in the plane Poiseuille flow, Carlson *et al.* (16) noted that the spots were accompagnied by oblique waves at their leading edge (wingtips). It was difficult, however, to find out whether the waves broke down and formed the new turbulence on the wingtips, or whether they are overtaken by the existing turbulence.

The nature of these waves and their role in the spreading of the spot were studied, using numerical simulations, by Henningson *et al.* (40). Due to the

modification of its stability properties by the presence of the spot, the surrounding flow is susceptible to unstable oblique Tollmien–Schlichting waves which may grow and then break down into turbulence. However, the linear growth rate of these waves calculated by Henningson (39) is too small compared to the observed one. Therefore, he suggested that the waves attain their large growth rate by some additional mechanisms.

Furthermore, Alavyoon *et al.* (1) compared spots in plane Poiseuille and boundary layer flows and pointed out the absence of waves at the wingtips of spots in the latter case. According to these authors, this indicates that if the same spreading mechanism is at work in both cases, then the waves are of no importance for the spreading itself. Whereas, if these waves play an important role in the spreading of spots in plane Poiseuille flow, then the spreading mechanisms are different and depend on the flow configurations. Hence, the role of the waves in the breakdown process and in the spreading mechanism of turbulent domain remains unclear and needs further study, as noted by Hennigson.

Therefore, the question of which mechanism is involved in the spreading of spots in shear flows is to a large extent open and despite a large body of experiments, a simple intuitive physical picture has been lacking.

An attempt to tackle such question led us to make use of our no-slip model. The outline of this chapter is as follows. In §6.2, some numerical results on the dynamics of turbulent spots are described. Then the structure of the flow at the boundary between laminar and turbulent domains is analyzed and the spreading mechanism is elucidated §6.3. This mechanism is further illustrated using a simple one-dimensional model. The main results of this chapter are assessed in the conclusion §6.4.

6.2 Growth of a turbulent spot

A standard Fourier pseudo-spectral method with periodic boundary conditions in the streamwise and spanwise directions has been implemented for the integration of the equations of the model (3.1-3.3). For details on the numerical method, see chapter 3.

As initial condition we take localized functions Ψ_0, Ψ_1 and Φ_1:

$$\Psi_0(x,z,t=0) = \Psi_1(x,z,t=0) = \Phi_1(x,z,t=0) = A\exp^{-(x^2+z^2)/\sigma},$$

where A is an amplitude and σ is related to the size of the initial turbulent domain.

Tracking the growth of a turbulent spot can be done by using one component of the velocity or vorticity fields at a given y-plane. Of particular benefit for our present study is the wall-normal vorticity associated to the drift flow (U_0, W_0). Figure 6.1 displays gray-level snapshots of $\Delta_2\Psi_0 = \partial_x W_0 - \partial_z U_0$, where $\Delta_2 =$

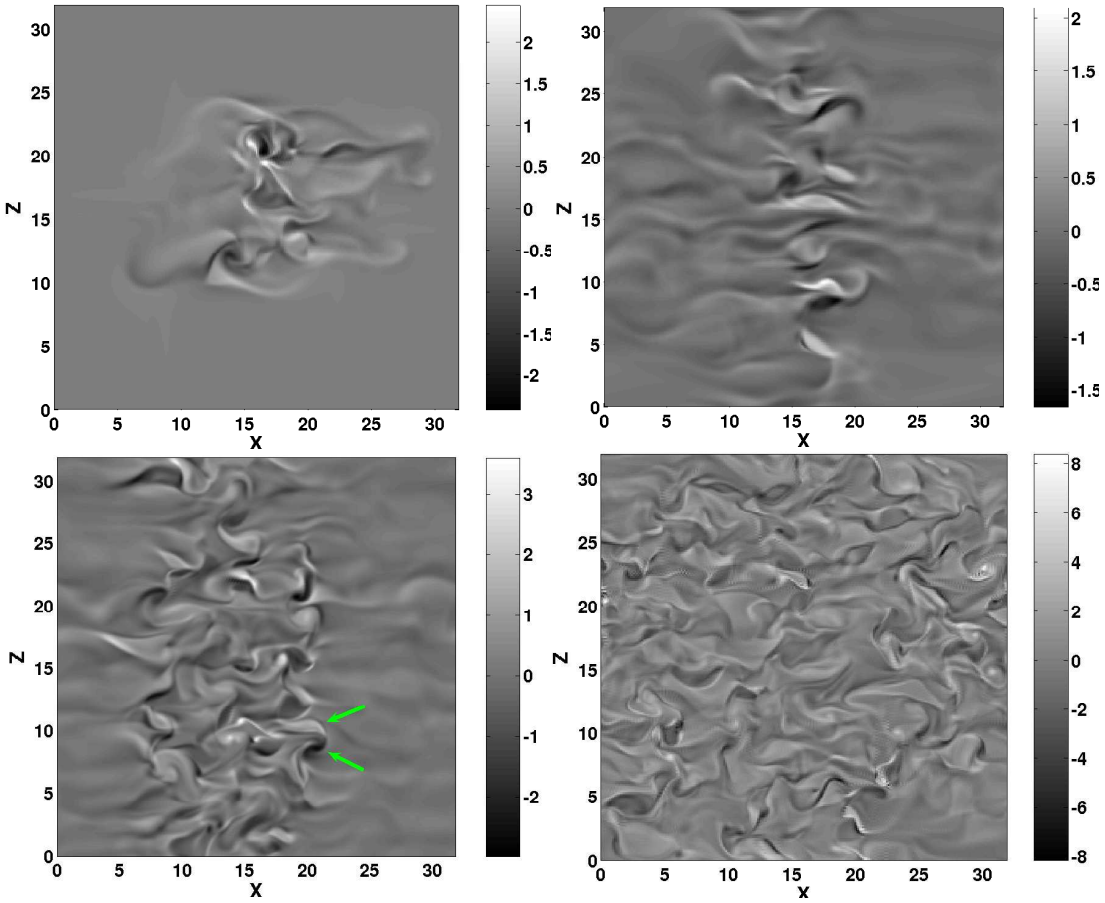

Figure 6.1: Growth of a turbulent spot with $R = 200$ in a domain with $L_x \times L_z = 32 \times 32$. Wall-normal vorticity $\Delta_2\Psi_0$ in gray levels. From left to right and top to bottom: t=20, 70, 156, 210.

$\partial_{xx} + \partial_{zz}$, at different times after initiation. The spot grows and contaminates the laminar domain at $t \sim 210$.

6.2.1 Coherent structures on the front

Flow structures at the boundaries between the laminar and turbulent domains are the elements needed for understanding the spreading mechanism of the spots. Arrows in Fig. 6.1 (at $t = 156$) show two adjacent patches with opposite signed vorticity $\Delta_2\Psi_0$ lying on the front propagating to the right. As shown in Fig. 6.2, these patches correspond to two counterrotating vortices (U_0, W_0). First, streamwise streaks U_0 are easily identified as regions where $|U_0| \gg |W_0|$. The sign of U_0 is alternating in the spanwise direction between positive and negative values, so that when the centers of the vortices lie along the z-axis, the distance between

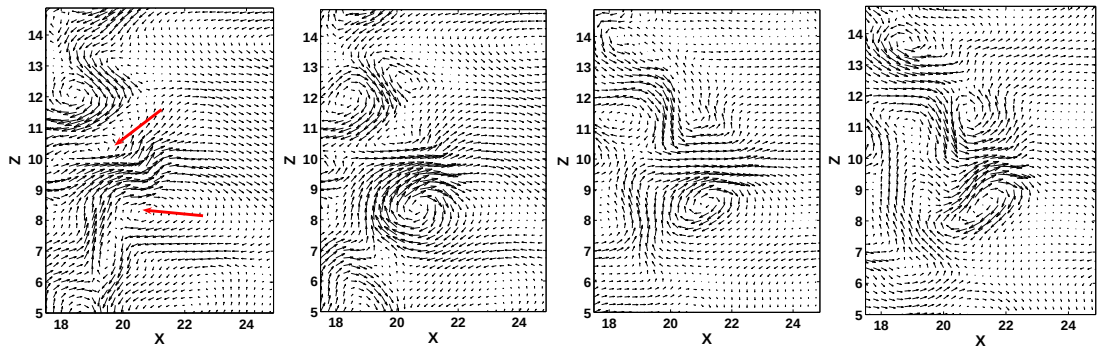

Figure 6.2: The flow (U_0, W_0) represented by arrows. From left to right: t=154, 156, 160 and $t = 162$.

the centers corresponds roughly to the width of the streak. This distance varies from $1h$ to $3h$, as can be seen from Fig. 6.2. Second, as may be inferred from the sense of rotation of both vortices, this dipole is propagating to the right. Before studying the origin and the consequence of this motion, it is instructive to track the expansion of the turbulent spot with the remaining flow velocity components.

Fig. 6.3 displays the spatial distribution of the wall-normal velocity V_1 and the flow field (U_1, W_1), corresponding to the region in Fig. 6.2. The reconstruction of the total flow field $((U_1, W_1)R_1(y), V_1S_1(y))$ in this region reveals a crescent vortex, studied in the previous chapters. Its legs are two streamwise vortices which regenerate the streaks U_0 through the lift-up.

As we have seen in Part II (Figure 15), there are two kinds of crescent vortices. During the spreading of the spot, both kinds are present inside the turbulent domain, but more interestingly, the crescent vortices present in the front propagating to the right (in the streamwise direction or roughly in the oblique direction) are of the first kind, as the one shown in Fig. 6.3, while the other kind populates the front propagating to the left. This observation is explained later on.

6.3 The spreading mechanism

The numerical simulations of the model have been used to identify elementary processes involved in the spreading mechanism. The dipoles (U_0, W_0) carry, during their propagation, the perturbation components (U_1, V_1, W_1...) in the (x, z)-plane. This spreading mechanism has two points to be examined. The first concerns the origin of the motion of the dipoles while the second deals with the consequence of such motion.

Elements of proof for both points can be given by studying the contribution of the advective term $U_0\partial_x f + W_0\partial_z f$ in the governing equation of f, where

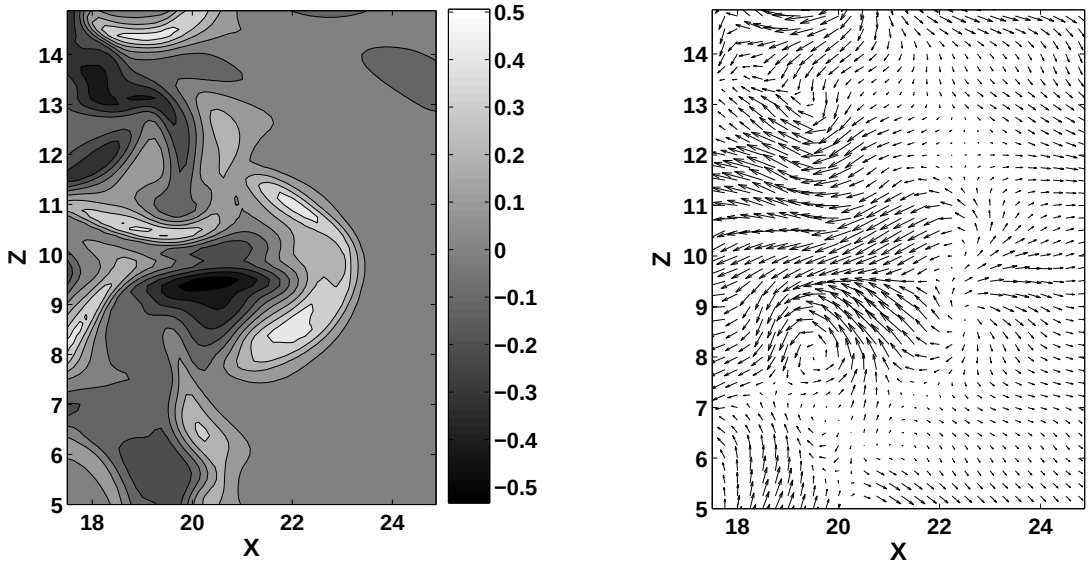

Figure 6.3: The isocontours of V_1 (left) and the field (U_1, W_1) (right) at $t = 156$. This flow distribution represents a crescent vortex.

the quantity f can be the wall-normal vorticities $\Delta_2\Psi_0$, $\Delta_2\Psi_1$, or the velocity V_1 or the streamwise vorticity etc. However, since this method produces data sets requiring a lot of post-treatment, it will be used only in §6.3.1 to study the origin of the motion of the dipoles (U_0, W_0) (first point). The entrainment of the perturbation components by these dipoles (second point) is investigated using a model in §6.3.2.

6.3.1 Origin of the dipole motion (U_0, W_0)

Let us consider the governing equation for the stream-function Ψ_0 of the drift flow (U_0, W_0) which can be rewritten as:

$$(\partial_t - R^{-1}(\Delta_2 - \gamma_0))\Delta_2\Psi_0 \;=\; J_0 + J_1 + J_2 + J_3 + J_4 + J_5, \qquad (6.1)$$

where the wall-normal vorticity of the flow (U_0, W_0) is $\partial_x W_0 - \partial_z U_0 = \Delta_2\Psi_0$. On the right hand side (r.h.s) we have:

$$\begin{aligned}
J_0 &= -\alpha_1(U_0\partial_x . + W_0\partial_z .)\Delta_2\Psi_0,\\
J_1 &= -a_1(U_\mathrm{b} + \tfrac{\alpha_2}{a_1}U_1)\partial_x\Delta_2\Psi_1,\\
J_2 &= -\alpha_2(\beta' + \beta)V_1\Delta_2\Psi_1,\\
J_3 &= \alpha_2\tfrac{3}{2}(U_1\partial_z . - W_1\partial_x .)\Delta_2\Phi_1,\\
J_4 &= -\alpha_2 W_1\partial_z\Delta_2\Psi_1,\\
J_5 &= a_1\tfrac{3}{2}U_\mathrm{b}\partial_z\Delta_2\Phi_1.
\end{aligned}$$

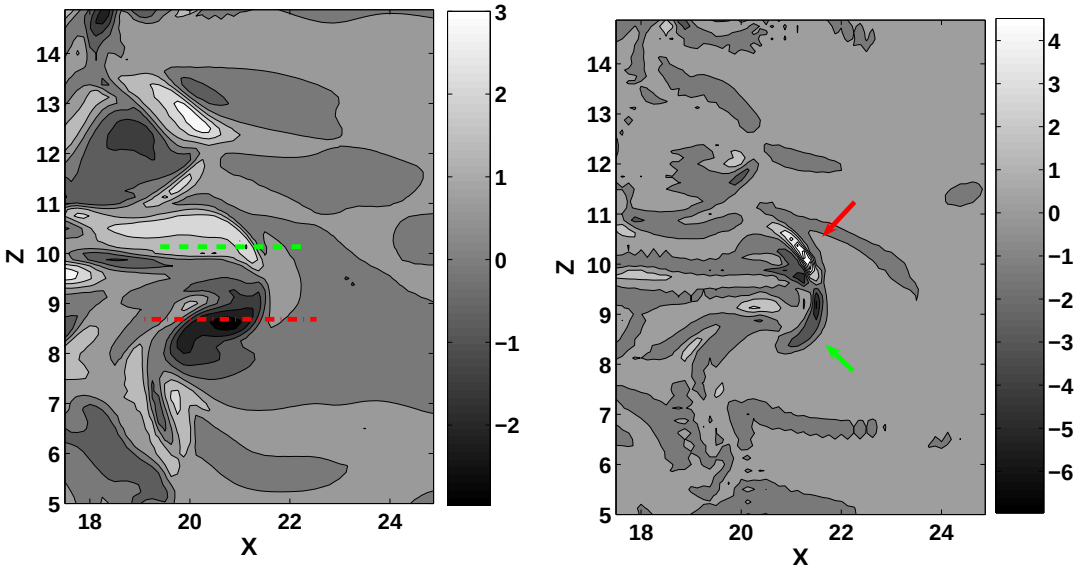

Figure 6.4: Left: Distribution of the wall-normal vorticity $\Delta_2\Psi_0$ at $t = 156$. The two patches of $\Delta_2\Psi_0$ with positive and negative values correspond to the dipole depicted in Fig. 6.2. Right: the spatial distribution of J_0 presents two patches of positive and negative values in front of $\Delta_2\Psi_0$.

The vorticity $\Delta_2\Psi_0$ results from the projection over $R_0(y)$ of the three-dimensional wall-normal vorticity $\partial_x w - \partial_z u$. In the same way, both terms J_0 and J_1 come from the projection over $R_0(y)$ of the term $u\partial_x(\partial_x w - \partial_z u)$ in the equation governing the vorticity $\partial_x w - \partial_z u$. The projection over $R_1(y)$ of $\partial_x w - \partial_z u$ gives the vorticity $\Delta_2\Psi_1 = \partial_x W_1 - \partial_z U_1$.

Note that by setting the flow components V_1, W_1 and U_1 to zero, all the terms in the r.h.s of Eq. 6.1 vanish except J_0. Hence, the equation governing the drift-flow reduces to the two-dimensional Navier-Stokes equation, with an additional viscous damping $R^{-1}\gamma_0$ induced by the friction of this flow on the plates. The term J_0 represents the advection of the two-dimensional flow $(U_0, W_0)R_0$ for its own vorticity $\Delta_2\Psi_0 R_0$.

The second term J_1 accounts for the generation of $\Delta_2\Psi_0 R_0$ through the shearing of the vorticity $\Delta_2\Psi_1 R_1$ by the velocity component $u' = U(y) + U_1 R_1(y)$. A physical interpretation of this shearing mechanism can be found in chapter 4. In regions where U_1 is negative, $U_1 R_1$ represents a correction to the base flow so that this u' has locally an **S**-shape, similar to the mean profile of the turbulent plane Couette flow. In the following, the scalar $\tilde{U_b} = U_b + \frac{\alpha_2}{a_1} U_1$ as well as u' are termed the corrected base flow.

Note finally that the lift-up effect is represented by the term J_5. Further interpretations of the terms in the r.h.s will be introduced on demand to analyze their different roles.

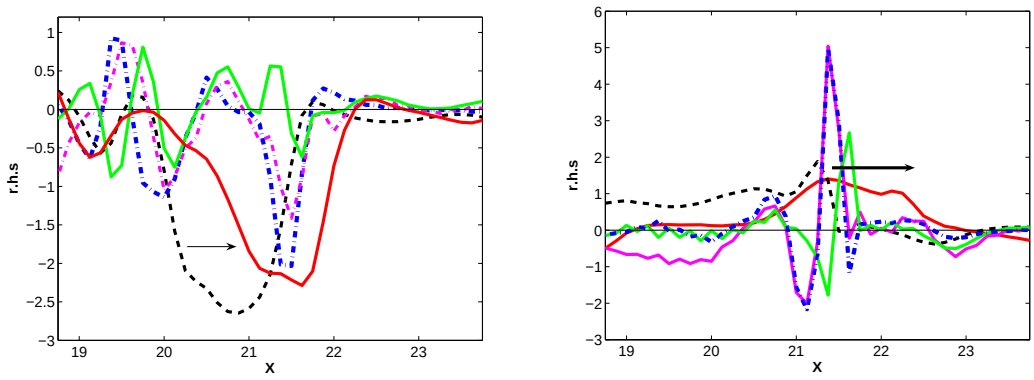

Figure 6.5: Different quantities as functions of coordinate x along the red (left panel) and green (right panel) line in Fig. 6.1. The values of $\Delta_2\Psi_0$ at $t = 156$ (in black dashed-line) and at $t = 162$ (in solid red line). The total r.h.s of Eq. 6.1 in dashed magenta. J_0 in dash-dotted blue line and J_1 in solid green line. The arrows indicate the sense of propagation.

Consider now the dipole depicted at successive times in Fig. 6.2. Its wall-normal vorticity $\Delta_2\Psi_0$ consists of two adjacent patches with opposite signs as shown in Fig. 6.4 (left). In front of each one, there is a same-signed patch of J_0, given in the right panel of this figure. This distribution of J_0 is reminiscent of the distribution of the nonlinear term, in two-dimensional Navier-Stokes equation, in front of a propagating dipole. Hence, the origin of the motion of the considered dipole would be the self-advection of the flow (U_0, W_0) if J_0 is preponderant over the other terms in the r.h.s of Eq. 6.1. This is indeed the case as attested to by Figure 6.5 where we plotted $\Delta_2\Psi_0$ between two successive instants as a function of x along the streamwise red-line (for $z \sim 9$) and the green-line (for $z \sim 10$) in Fig. 6.4 together with the whole r.h.s. of Eq. 6.1. The term J_0 represents the largest contribution to this r.h.s. which is negative (positive) in front of the negative (positive) patch of $\Delta_2\Psi_0$ so that this vorticity propagates to the right. From a physical point of view, this propagation can be explained as the effect of the induced velocity of one vortex on the other in accordance to the Biot–Savart law.

In the following we study the contributions, albeit weaker, of the other terms. Such study will give a clear picture of the roles of these terms. Since it involves the interactions between the coherent structures previously studied in chapter **??**, a summary of the mechanisms at work is given here.

First, the term J_1 acts against the propagation of the dipole by damping the vorticity $\Delta_2\Psi_0$. Indeed, this term is positive (negative) where $\Delta_2\Psi_0$ is negative (positive), as shown in Fig. 6.5. The origin of such behavior is as follows. Once the streaks U_0 are regenerated by the streamwise vortices, they are sheared by

the base flow (linear transport) and induce the velocity component U_1 according to $\partial_t U_1 \sim -a_1 U_\mathrm{b} \partial_x U_0$ (see previous chapters). Within the formulation of the equations in terms of stream functions, this generation mechanism is represented by the linear term $-a_1 U_\mathrm{b} \partial_x \Delta_2 \Psi_0$ in the equation governing $\Delta_2 \Psi_1$ (3.2). Hence, the distribution of the induced vorticity $\Delta_2 \Psi_1$ through the shearing of the vorticity $\Delta_2 \Psi_0$ by the base flow is roughly given by $\Delta_2 \Psi_1 \sim -a_1 U_\mathrm{b} \partial_x \Delta_2 \Psi_0$ (with $U_\mathrm{b} = 1$). It follows that:

$$J_1 = -a_1 \tilde{U_\mathrm{b}} \partial_x \Delta_2 \Psi_1 \sim \tilde{U_\mathrm{b}} \partial_{xx} \Delta_2 \Psi_0,$$

showing that J_1 behaves like a dissipative term (with $\tilde{U_\mathrm{b}} \geq 0$).

Consider then the term J_2, which involves the quantities V_1 and $\Delta_2 \Psi_1$. On the right of both patches of positive and negative values of $\Delta_2 \Psi_0$, the velocity V_1 remains positive (crescent contour) whereas $\Delta_2 \Psi_1$ ($\sim -U_\mathrm{b} \partial_x \Delta_2 \Psi_0$) changes its sign. It follows that in front of the dipole, J_2 and J_0 have opposite-signed distributions, thus, the former term acts against the progression of the dipole.

The remaining terms J_3, J_4 and J_5 are now considered. As shown in chapter 5, the head of the crescent vortex is a spanwise vortex, where the flow (U_1, W_1) is dominated by $|U_1| \gg |W_1|$ and $U_1 \leq 0$ (although $U_1 \sim 0$ in the present case). Hence, lumping the three terms and neglecting the contribution of W_1 yield:

$$J_3 + J_4 + J_5 \approx a_1 \tfrac{3}{2} (U_\mathrm{b} + \tfrac{\alpha_2}{a_1} U_1) \partial_z \Delta_2 \Phi_1,$$

which accounts for the lift-up effect, i.e. the extraction of the energy from the corrected base flow $(U_\mathrm{b} + \frac{\alpha_2}{a_1} U_1)$ by the wall-normal velocity V_1. Therefore, the quantity $J_3 + J_4 + J_5$ is a source term for the streaks and thus for their wall-normal vorticity $\Delta_2 \Psi_0$.

As a conclusion, by analyzing the different terms in the r.h.s of Eq. 6.1, this short study shows that (i) the dominant term is J_0 and that (ii) the distributions of the different remaining terms can be determined since the involved quantities (U_1, U_0, V_1,...) are correlated through the cycle of self-sustained mechanisms for wall-bounded turbulence (Chap. 4). The propagation of the vortices (U_0, W_0) is hence due to their self-advection (the term J_0). While some of these terms enhance the propagation, such as $J_3 + J_4 + J_5$ which intensifies the vorticity of the dipole, other terms act against this propagation by either weakening this vorticity, such as J_1, or by damping the contribution of J_0, such as J_2.

Note, however, that the preponderance of one term over the others is not permanent. For example, it is clear that during the linear growth of the vorticity $\Delta_2 \Psi_0$ by the lift-up effect, the nonlinear contribution of J_0 is negligible compared to that of J_5. In other words, arguing that a term dominates another one necessitates the explicit reference to which mechanism in the cycle is occuring. In this study we were only concerned about the origin of the propagation of the dipoles once they are generated and about the roles of the different terms in the r.h.s of Eq. 6.1 in this propagation.

In the following, the consequence of the motion of the dipoles on the other perturbation components is studied using a set of 1-dimensional partial differential equations.

6.3.2 Entrainment of the perturbations: an illustrative model

A simple model is now derived to illustrate the entrainment of the perturbations in the x-direction through the motion of the dipoles (U_0, W_0). The z-dependence of the perturbations is frozen on some Fourier modes. The symmetries of the problem are then used to simplify the expansions of the fields by choosing a set of functions satisfying a particular symmetry. This choice is driven by the fact that the wall-normal vorticity of a dipole propagating in the x-direction is odd in z.

Hence, the fields Ψ_0, Ψ_1 and Φ_1 for such a solution have these Fourier expansions:

$$\begin{aligned}
\Psi_0 &= \sum_{n\geq 1} A_n(x,t)\sin(n\theta z),\\
\Psi_1 &= \sum_{n\geq 1} B_n(x,t)\sin(n\theta z),\\
\Phi_1 &= \sum_{n\geq 0} C_n(x,t)\cos(n\theta z),
\end{aligned}$$

where $\theta = 2\pi/L_z$ is the spanwise fundamental.

A stream-function of a dipole (U_0, W_0) can be represented by the first mode $\Psi_0(x,z,t) = A_1(x,t)\sin(\theta z)$. However, due to the z-periodicity, this dipole cannot propagate in the x-direction. To remedy this, it is sufficient to include the second harmonic in this expansion, $A_2(x,t)\sin(2\theta z)$. The superposition of these two modes yields a modulated array of vortices in the spanwise direction.

Then for the stream-function Ψ_1, we have to include the first two modes, since the vorticity $\Delta_2\Psi_1$ is linearly generated from $\Delta_2\Psi_0$ through the linear term $-a_1 U_\mathrm{b}\partial_x\Delta_2\Psi_0$ (Eq. 3.2).

Last, the expansion of the potential velocity Φ_1, which is related to the wall-normal velocity V_1 of the vortices (either spanwise or streamwise), is truncated. The nonlinear interactions of the in-plane (x,z) flow components induce this V_1 through the terms $-U_1\partial_z W_0$ and $W_0\partial_z U_1$ (Chap. 5). Accordingly, we have to keep the Fourier modes generated by these terms with $U_1 = -\partial_z\Psi_1$ and $W_0 = \partial_x\Psi_0$. With the retained modes for Ψ_0 and Ψ_1, these modes are 1, $\cos(\theta z)$, $\cos(2\theta z)$ and $\cos(3\theta z)$. Finally, the expansions read:

$$\Psi_0 = A_1(x,t)\sin(\theta z) + A_2(x,t)\sin(2\theta z), \tag{6.2}$$

$$\Psi_1 = B_1(x,t)\sin(\theta z) + B_2(x,t)\sin(2\theta z), \tag{6.3}$$

$$\Phi_1 = C_0(x,t) + C_1(x,t)\cos(\theta z) + C_2(x,t)\cos(2\theta z) + C_3(x,t)\cos(3\theta z) \tag{6.4}$$

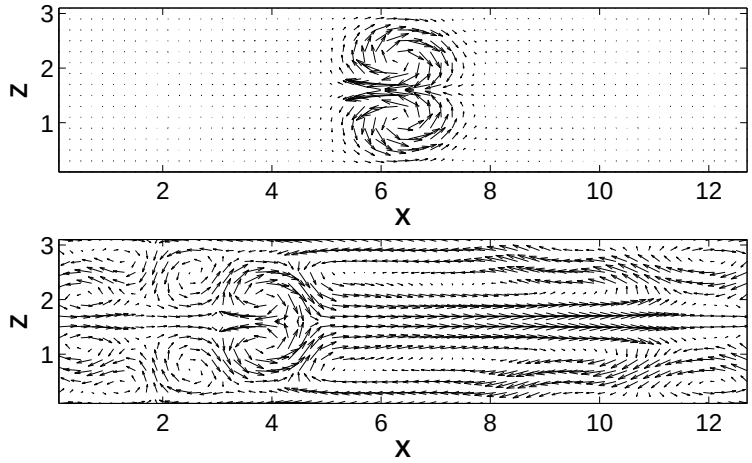

Figure 6.6: The propagating dipole depicted by the flow (U_0, W_0) at $t = 0.1$ (top) and $t = 5$ (bottom). $R = 200$.

Numerical results

The numerical integration of the illustrative model can be easily done using the code already developed for the no-slip model. Between two successive time steps, all the Fourier modes of the three fields are set to zero except the retained modes in the expansions above.

As an initial condition we take $A_1(x,0) = -\frac{4}{5\pi^2}e^{-2(x-x_C)^2}$, $A_2(x,0) = -\frac{1}{2}A_1(x,0)$, C_0=C_1=C_2=C_3=0, $B_1(x,0) = -\frac{4}{9\sqrt{\sqrt{3\pi}}}e^{-(x-x_C)^2/6}$ and $B_2(x,0) = -\frac{1}{2}B_1(x,0)$. The streamwise length of the computational domain is $L_x = 12.8$ with $x_C = L_x/2$ and the Reynolds number is $R = 200$. Choosing $\theta = 2\pi/L_z$ with $L_z = 3.2$ yields a streak U_0 with a spanwise width of about $\approx L_z/2 = 1.6$. With the retained value of θ, we have $U_0(x,z,0) \approx O(1)$ and $U_1(x,z,0) \approx O(1)$.

First, the dipole (U_0, W_0) depicted in Figure 6.6 is propagating to the left, as could be inferred from the sense of rotation of both vortices. This propagation is also tracked by its vorticity $\Delta_2\Psi_0$ as shown in Fig. 6.7. Second, during its propagation, this dipole carries the other flow components. Indeed, Figure 6.8 illustrates the generation and the entrainment of a crescent vortex to the left, depicted by the wall-normal velocity V_1. The corresponding flow field (U_1, W_1) is given in Fig. 6.9. The legs of this crescent are two streamwise vortices characterized by two patches of streamwise vorticity $\omega_x = \beta W_1 - \partial_z V_1$, as shown in Fig. 6.10. During their propagation to the left, they regenerate the streaks and produce positive Reynolds stress $-U_0V_1$: positive (negative) patches of V_1 correspond to the negative (positive) regions of U_0. Hence during its motion,

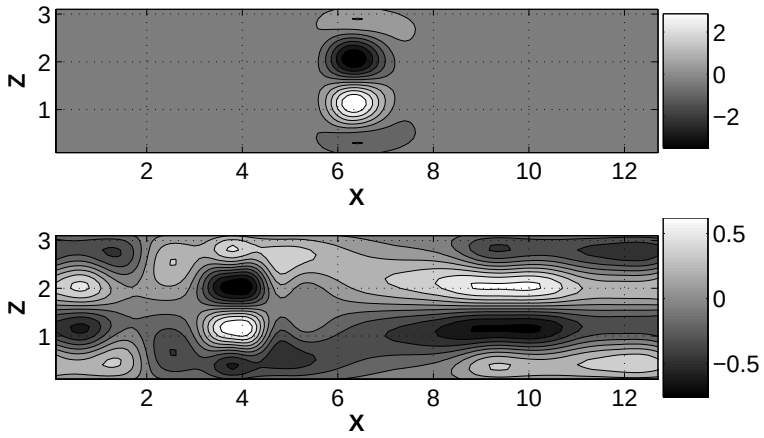

Figure 6.7: The wall-normal vorticity $\Delta_2\Psi_0$ at $t = 0.1$ (top) and $t = 5$ (bottom).

the dipole (U_0, W_0) carries the crescent vortex, which continues to regenerate it through the lift-up effect.

Afterwards, the wall-normal vorticity $\Delta_2\Psi_0$ associated with these streaks is sheared by the base flow and a vorticity $\Delta_2\Psi_1$ is induced. Its distribution is roughly given by $\Delta_2\Psi_1 \sim -a_1 U_\mathrm{b}\partial_x\Delta_2\Psi_0$, as shown in Fig. 6.10 by the arrows. In turn, this vorticity damps the progression of the dipole (the term J_1).

Finally we have stated in §6.2 that, for a given spot, each front was populated by a particular kind of the crescent vortices. The reason behind this distribution is simple. Depending on the sense of rotation of the dipole (U_0, W_0), a spanwise vortex is deformed by this dipole and gives a crescent vortex of the first or the second kind. If it is of the first kind (as the one depicted in Fig. 6.8), it is advected to the left whereas, if it is of the second kind, it is advected to the right (as the one depicted in Fig. 6.3).

As a conclusion, this model illustrates well the entrainment of the flow quantities by a propagating dipole (U_0, W_0). The interactions between the flow components encountered in the previous section such as the lift-up effect, are well captured by this model. Its natural limitation is that the dipole is allowed to propagate only in the x-direction, since its z-dependence is frozen.

6.4 Discussion and conclusion

In this chapter, the spreading of a turbulent spot was investigated. The contamination of the laminar domain by the turbulent domain is the consequence of the motion in the horizontal-plane of wall-normal vortices spanning all the gap between the two plates.

First, we have shown that the dynamic of these dipoles is governed by their

self-advection. Second, during their motion, these dipoles carry the other perturbation components and continue to interact with them. For instance, the carried crescent vortex continues to regenerate the streaks by the lift-up mechanism. As a consequence of this entrainment by the dipoles, the front propagating to the right is populated by crescent vortices of the first kind, whereas the one propagating to the left is populated by crescent vortices of the second kind. The core of the spot, however, is filled with both kinds, as shown in Fig. 6.11.

Furthermore, our aim is to present the elementary building block of the spreading mechanism which is the motion of the dipoles. For this reason, we did not study the interactions of these blocks, for instance, when two dipoles moving in opposite directions encounter one another and then propagate in the spanwise direction, as shown in Fig. 6.11. Moreover, depending on the sense of their rotation, the dipoles propagate in the (x, z)-plane towards the x-direction but also towards the oblique direction, since they are not all symmetric in z. Figure 6.2 (for $t = 156$) gives an example of such dipole (for $z \geq 11, x \leq 21$). Its vorticity is shown in Fig. 6.1.

Furthermore, we have seen in Chap. 4 that on the outskirts of the turbulent spot, there is a quadrupolar large-scale flow denoted by $(\overline{U_0}, \overline{W_0})$. Some possible consequences of this flow on the spreading of the spot can be provided by the present study. The large-scale streamwise inflow $\overline{U_0}$ could hinder this spreading since it pushes the small-scale dipoles (U_0, W_0) towards the core of the spot, thus acting against their progression in the streamwise direction, as illustrated in Fig. 6.11.

In contrast, the large scale outflow $\overline{W_0}$ contributes to the spreading of the spot in the spanwise direction by advecting the perturbations in the core of the spot outwards. This outflow $\overline{W_0}$ acting in both spanwise directions would explain the spot splitting phenomenon, occuring at Reynolds numbers close to the transitional and observed in experimental studies (e.g. (23)) and in other shear flows experiencing a transition to turbulence by nucleation of spots, as plane Poiseuille flow (16).

Despite its limited cross-stream resolution, our model for pCf gives valuable hints about the spreading mechanism of turbulent spots. First, the presented mechanism still holds when we increase the wall-normal resolution. A glimpse on the derivation of such higher order models is given in Chap. 5. Second, the models derived in Chap. 2 for pCf with free-slip boundary conditions on the plates for different resolutions in y, exhibit the same spreading mechanism as in the no-slip case. Third, evidence of the presence of the dipoles on the front can be obtained from laboratory experiments by measuring the wall-normal vorticity either at the mid-plane or by averaging it over the gap. The experimental investigation of Schröder & Kompenhaus (92) is an example of such studies but in other wall flow of more practical interest than pCf. Their Figure 6 and Figure 13 describe the result of an ensemble average of the wall-normal vorticity of spots in boundary layer flow and show small adjacent regions of opposite-signed vorticity.

Clearly, further studies investigating the internal structures of turbulent spots and especially the substructures on the edge of the spot are needed to conclusively comment on the spreading mechanism presented in this chapter and its occurence in real turbulent spot. The experimental works of Perry (79) and of Sankaran *et al.* (85; 86) who investigated the structure of a spot in boundary layer flow as well as the numerical investigation of Singer (94) and the recent experiments of Makita & Nishizawa (62), are examples of such studies.

Finally, the present discussion of the spreading mechanism and the flow patterns at the boundaries could be a stepping stone for a quantitative estimation and derivation of the front propagation speed v_{fr}. The formula $v_{\mathrm{fr}} \propto \Gamma/2\pi r$, where Γ is the recirculation of the vortices (U_0, W_0) and r is related to the streak spacing, could be a good starting point.

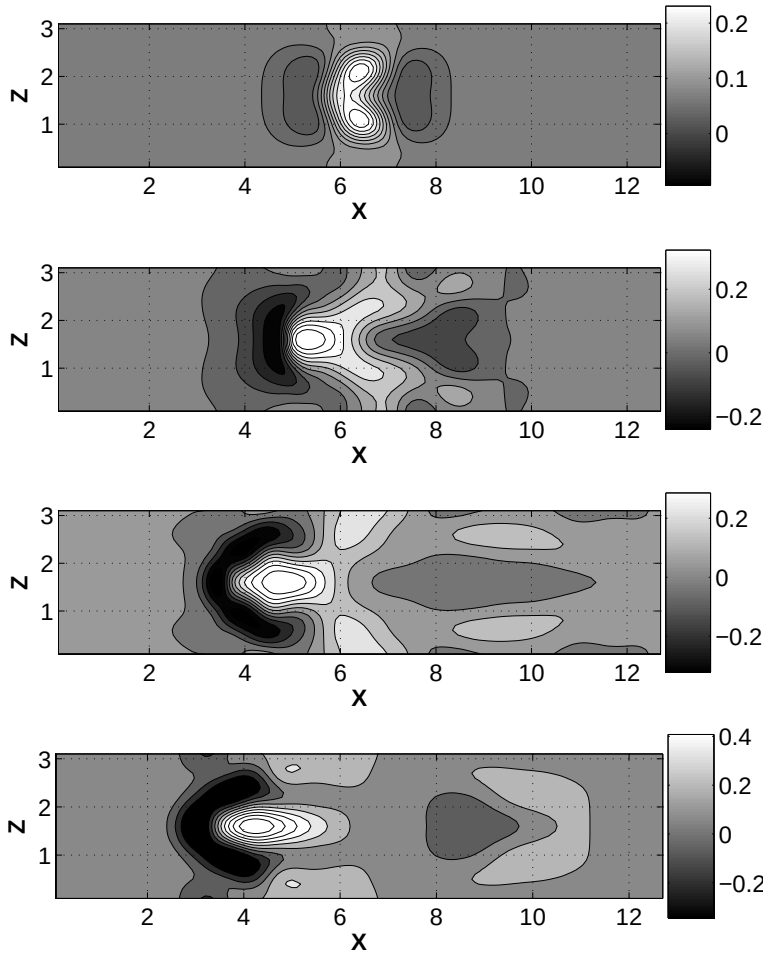

Figure 6.8: Generation and entrainment of a crescent vortex, depicted by its vertical velocity V_1. From top to bottom, t = 0.1,1,3 and 5. The flow field (U_1, W_1) is given below in Fig. 6.9.

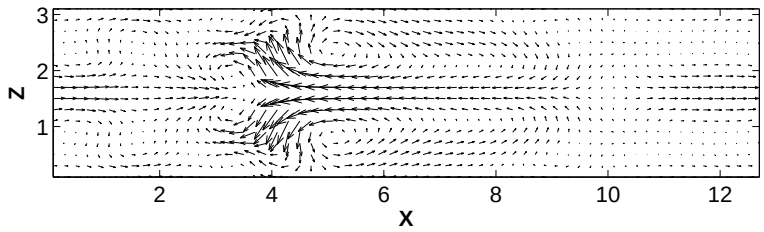

Figure 6.9: The flow field (U_1, W_1) at $t = 5$. This flow field together with the corresponding V_1, represents a crescent vortex.

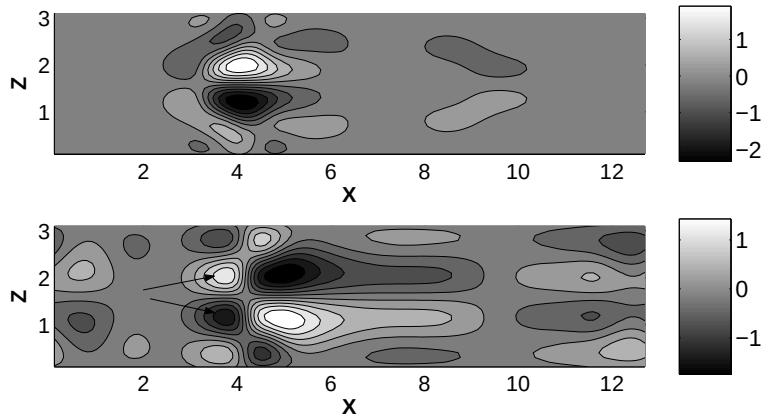

Figure 6.10: Top: the streamwise vorticity ω_x. Bottom: the wall-normal vorticity $\Delta_2\Psi_1$ at $t = 5$.

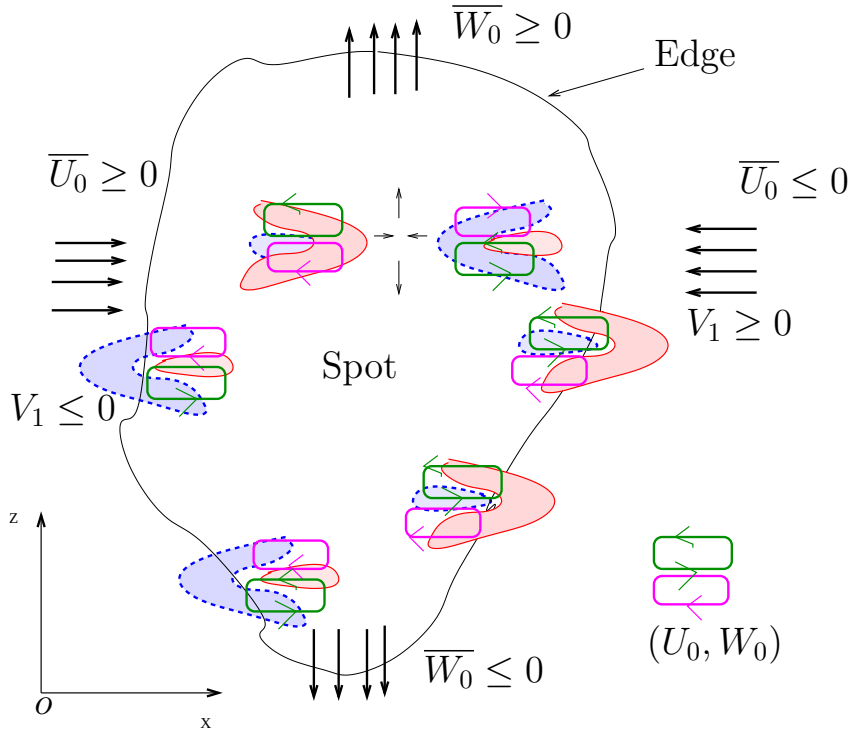

Figure 6.11: General view of the spreading mechanism, with the role of the large scale flow outside the spot. The outflow contributes in the spreading of the spot in the spanwise direction, whereas the inflow acts against the progression of the small-scales dipoles (U_0, W_0) in the x-direction. Red-solid (blue-dashed) contours indicate regions of positive (negative) values.

Bibliography

[1] Alavyoon, F. Henningson, D.S. & Alfredsson, P.H. Turbulent spots in plane Poiseuille flow-flow visualization. Phys. Fluids **29** (1986) 1328–1331.

[2] Antonia, R.A. & Kim, J. Low-Reynolds-number effects on near-wall turbulence. J. Fluid Mech. **276** (1994) 61–80.

[3] Baggett, J. S. & Trefethen, L. N. Low-dimensional models of subcritical transition to turbulence. Phys. Fluids **9**, (1997) 1043–1053.

[4] Balint, J.L. Wallace, J.M. Vukoslavcevic, P. The velocity and vorticity vector-fields of a turbulent boundary-layer.2. Statistical properties. J. Fluid Mech. **228** (1991) 53–86.

[5] D. Barkley & L. Tuckerman, Mean Flow of Turbulent-Laminar Patterns in Plane Couette Flow, to appear in J. Fluid. Mech. (2007).

[6] Barkley, D. Tuckerman, L.S. Computational study of turbulent-laminar patterns in Couette flow. Phys. Rev. Lett. **94** (2005) 014502.

[7] Blackwelder RF. An Experimental Model for Near-Wall Structure, AIAA 98-2960, 1998 (also In: Panton RL, editor. Self-sustaining mechanisms of wall turbulence. Boston: Computational Mechanics Publications, 1997).

[8] Bech, K.H. Tillmark, N. Alfredsson, P.H. Andersson, H.I. An investigation of turbulent plane Couette flow at low Reynolds numbers. J. Fluid Mech. **286** (1995) 291–325.

[9] Berkooz, G., Holmes, P. & Lumley, J. L. The proper orthogonal decomposition in the analysis of turbulent flows. Annu. Rev. Fluid Mech. **25**, (1993) 539–575.

[10] Bogard D.G, Tiederman W.G. Characteristics of ejections in turbulent channel flow. J Fluid Mech. **1** (1987) 1.

[11] Bottin, S. and Chaté, H. Statistical analysis of the transition to turbulence in plane Couette flow. Eur. Phys. J. B., **6**, (1998) 143–155.

[12] Bottin, S. Daviaud F, Manneville P, Dauchot O. Discontinuous transition to spatiotemporal intermittency in plane Couette flow. Europhys. Lett. **43** (1998) 171–176.

[13] Bottin S., Dauchot O. Daviaud F. Manneville P. Experimental evidence of streamwise vortices as finite amplitude solutions in transitional plane Couette flow, Phys. Fluids **10** (1998) 2597–2607.

[14] Brandt L, Cossu C, Chomaz L, Huerre P, Henningson D. On the convectively unstable nature of optimal streaks in boundary layers, J. Fluid Mech. **485** (2003), 221-242.

[15] Brooke J.W, Hanratty T.J, Origin of turbulence-producing eddies in a channel flow. Phys. Fluids A (1993), **5**,1011.

[16] Carlson, D.R. Widnall, S.E. Peeters, M.F. A flow visualization of transition in plane Poiseuille flow, J. Fluid Mech. **121** (1982) 487–505.

[17] Corrsin S. Some current problems in turbulent shear flows (1955). In Panton RL, editor. Self-sustaining mechanisms of wall turbulence. Boston: Computational Mechanics Publications, 1997.

[18] D. Coles, Transition in circular Couette flow, J. Fluid Mech. **21** (1965) 385–425.

[19] Cros A. Le Gal, P. Spatiotemporal intermittency in the torsional Couette flow between a rotating and a stationary disk. Physics of Fluids. **14**, (2002) 3755–3765.

[20] Darbyshire, A.G. and Mullin, T. Transition to turbulence in constant-mass-flux pipe flows. J. Fluid. Mech. **289**, 83-114 (1995).

[21] Dauchot, O. Manneville, P. Local Versus Global Concepts in Hydrodynamic Stability Theory. J. Phys. II **7** (1997) 371–389.

[22] Dauchot O. Daviaud F. Finite amplitude perturbation in plane Couette flow. Europhysics letters. **28** (4), (1994) 225–230.

[23] Dauchot O. Daviaud F. Finite amplitude perturbation and spots growth-mechanism in plane Couette flow Physics of Fluids. **7** (2), (1995) 335–343.

[24] F. Daviaud, J. Hegseth & P. Bergé, Subcritical transition to turbulence in plane Couette flow, Phys. Rev. Lett. **69** (1992) 2511–2514.

[25] A. Das & J. Mathew, Direct numerical simulation of turbulent spots, Computers & Fluids **30** (2001) 533–541.

[26] Drazin, P.G. *Introduction to Hydrodynamic Stability* (Cambridge, 2002)

[27] Dauchot, O. Daviaud, F. Europhys. Lett. **28** (1994) 225.

[28] Eckhardt, B. Mersmann, A. Transition to turbulence in a shear flow. Phys. Rev. E. **60**, (1999) 509–517.

[29] Eckhardt, B. Schneider T.M, "Edge states in the transition to turbulence in pipe flow", EFMC6 Stockholm, June 26-30, (2006).

[30] Eckmann, J.P. Ruelle, D. Rev. Mod. Phys. **57** (1985) 617-656.

[31] H.W. Emmons, The laminar-turbulent transition in a boundary layer, Part I, J. Aero. Sci. **18** (1951) 490–498.

[32] Finlayson, B.A. *The method of weighted residuals and variational principles, with application in fluid mechanics, heat and mass transfer* (Academic Press, 1972).

[33] Gad-El-Hak M., Blackwelder R.F, Riley J.J On the growth of turbulent regions in laminar boundary layers, J. Fluid Mech. **110** (1981) 73–95.

[34] Glansdorff, P. Prigogine, I. *Structure, Stabilité et Fluctuations* (Masson, 1971), Chap. 11, Sect. 10.

[35] Grossmann, S. The onset of shear flow turbulence. Rev. Mod. Phys. **72** (2000) 603–618.

[36] Hamilton J.M, Kim J., Waleffe F., Regeneration mechanisms of near-wall turbulence structures J. Fluid Mech. **287** (1995) 317–348.

[37] F. Hayot & Y. Pomeau, Turbulent domain stabilization in annular flows, Phys. Rev. E **50**, (1994) 2019–2021.

[38] Hegseth J.J, Turbulent spots in plane Couette flow Physical review E. **54** (5), (1996) 4915–4923

[39] Henningson, D.S. Wave growth and spreading of a turbulent spot in plane Poiseuille flow. Phys. Fluids A- Fluid dynamics **1** (1989) 1876–1882.

[40] Henningson , D. Spalart, P. & Kim, J. Numerical simulations of turbulent spots in plane Poiseuille and boundary-layer flow. Phys. Fluids **30** (1987) 2914–2917.

[41] Henningson D.S. & Kim J. On turbulent spots in plane Poiseuille flow. J. Fluid Mech. **228** (1991) 183–205.

[42] D.S. Henningson, A.V. Johansson & P.H. Alfredsson, Turbulent spots in channel flows, Journal of Engin. Math. **28** (1994) 21–42.

[43] Heist, D.K., T. J. Hanratty and Y. Na Observations of the formation of streamwise vortices by rotation of arch vortices, Physics of Fluids, **12** (2000), 2965–2975.

[44] Higgins, J.R. Completeness and basic properties of sets of special functions, Cambridge University Press, (1977) Cambridge.

[45] Hof, B. Westerweel, J. Schneider T.M, Eckhardt, B. "Finite lifetime of turbulence in shear flows," Nature **443** (2006) 59–62.

[46] Holmes, P. Can dynamical systems approach turbulence? In Whither Turbulence? Turbulence at the Crossroads. Ed. J. L. Lumley, 195–249. Springer (1990).

[47] Turbulence, Coherent Structures, Dynamical Systems and Symmetry. Holmes, P., Lumley, J. L. & Berkooz, G. Cambridge University Press (1996).

[48] Jimenez J, Pinelli A. The autonomous cycle of near-wall turbulence. J Fluid Mech **389** (1999) 335.

[49] Jimenez J., Moin P. The minimal flow unit in near-wall turbulence. J. Fluid Mech. **225** (1991) 213–240.

[50] Kim J, Moin P, Moser R.D. Turbulence statistics in fully developed channel flow at low Reynolds number. J Fluid Mech. **177** (1987) 133.

[51] Kitoh, O. Nakabyashi, K. Nishimura, F. Experimental study on mean velocity and turbulence characteristics of plane Couette flow: low-Reynolds-number effects and large longitudinal vortical structure. J. Fluid Mech. **539** (2005) 199–227.

[52] Klebanoff, P.S., Tidstrom, K.D. Sargent, L.M. The three-dimensional nature of boundary layer instability, J. Fluid Mech. **12** (1962) 1–34.

[53] Kleiser, L. & Zang, T.A. Numerical simulation of transition in wall bounded shear flows. Ann. Rev. of Fluid Mech. (1991) **23** 495–537.

[54] Kline S.J, Reynolds W.C, Schraub F.A, Runstadler P.W. The structure of turbulent boundary layers. J. Fluid. Mech. **30** (1967) 741.

[55] Kloosterziel, R.C. On the large-time asymptotics of the diffusion equation on infinite domains. J. Eng. Math. **24**,3, (1990) 213–236.

[56] Komminaho, J. Lundbladh, A. Johansson, A.V. Very large structures in plane turbulent Couette flow. J. Fluid Mech. **320** (1996) 259–285.

[57] Lee, M. J. & Kim, J. The structure of turbulence in a simulated plane Couette flow. Proc. 8th Symposium on Turbulent Shear Flows, Munich (1991), paper 5-3.

[58] F. Li & S.E. Widnall, Wave patterns in plane Poiseuille flow created by concentrated disturbances, J. Fluid Mech. **208** (1989) 639–656.

[59] Liu, Z. C., Adrian, R. J. & Hanratty T.J., High resolution measurement of turbulent structure in a channel with PIV. Exps. Fluids **10**, 301–312.

[60] Locher, F. Manneville, P. C.R. Acad. Sci. Paris, **328** Serie IIb, (2000) 159–164.

[61] Lundbladh A, Johansson A.V. Direct simulation of turbulent spots in plane Couette flow. J. Fluid Mech. **229**, (1991) 499–516.

[62] Makita, H. & Nishizawa, A. Characteristics of internal vortical structures in a merged turbulent spot. Jour. of Turbulence (2001) **2** 1–14.

[63] Manneville, P. Dauchot, O. in *Coherent structures in classical systems*,: The case of plane Couette flow. D. Reguera, L.L. Bonilla, J.M. Rubi, eds. (Springer Verlag, 2001) pp. 58–79.

[64] Manneville, P. Spots and turbulent domains in a model of transitional plane Couette flow. Theor. and Comp. Fluid Dyn. **18**, (2004) 169–181.

[65] Manneville, P. "Liapounov exponents for the Kuramoto-Sivashinsky model", in Macroscopic modelling of turbulent flows and fluid mixtures, Springer Lectre Notes in Physics **230** (1985) 319–326.

[66] Manneville, P. in *Cellular Structures in Instabilities*, J.E. Wesfreid, S. Zaleski, eds. Lect. Notes in Physics **210** (1983) 137–155.

[67] Manneville, P. "Modeling the direct transition to turbulence" at the IUTAM SYMPOSIUM *Non-Uniqueness of Solutions to the Navier-Stokes Equations and their Connection with Laminar-Turbulent Transition*, Bristol 2004 (Kluwer, in (73)).

[68] P. Manneville, *Instabilities, Chaos and turbulence*, Imperial College Press, 2004.

[69] Mathew, J. & Das, A. Direct numerical simulations of spots. Current science **79** (2000) 816–820.

[70] Moehlis, J. Faisst, H. Eckhardt, B. A low-dimensional model for turbulent shear flows. New Journal of Physics **6** (2004) 56.

[71] Moehlis, J., Smith, T. R., Holmes, P. & Faisst, H. Models for turbulent plane Couette flow using the proper orthogonal decomposition. Phys. Fluids **14**, (2002) 2493–2507.

[72] Morse P.M. & Feshbach H. Methods of theoretical physics, McGraw-Hill, (1953) New York.

[73] Mullin, T. Kerswell, R.eds. IUTAM Symposium on Laminar-turbulent Transition and Finite Amplitude Solutions (Springer, 2005).

[74] Orszag S.A. Accurate solution of the Orr-Sommerfeld stability equation, J. Fluid Mech. **50** (1971) 689–703.

[75] Papavassiliou, D.V. Hanratty, T.J. Interpretation of large-scale structures observed in a turbulent plane Couette flow. Int. J. of Heat and Fluid flow. **18** (1) (1997) 55–69.

[76] Panton R.L, Editor. Self-sustaining mechanisms of wall turbulence. Boston: Computational Mechanics Publications, (1997).

[77] Panton R.L, Overview of the self-sustaining mechanisms of wall turbulence. Progress in Aerospace Sciences **37** (2001) 341–383.

[78] Peixinho, J. and Mullin, T. Decay of turbulence in pipe flow. Phys. Rev. Lett. **96**, (2006) 094501.

[79] Perry, A.E. Lim, T.T. Teh, E.W. A visual study of turbulent spots. J. Fluid Mech. **104** (1981) 387–405.

[80] A. Prigent, G. Grégoire, H. Chaté, O. Dauchot & W. van Saarloos, Large-scale finite-wavelength modulation within turbulent shear flows, Phys. Rev. Lett. **89** (2002) 014501.

[81] Pomeau Y. Front motion, metastability and subcritical bifurcations in hydrodynamics. Physica D **23** (1986) 3–11.

[82] Pomeau, Y. C.R. Acad. sc. Paris **300** serie II (1985) 239–241.

[83] Rempfer, D Low-dimensional modeling and numerical simulation of transition in simple shear flows. Ann. Rev. Fluid. Mechanics, **35**, (2003) 229–265.

[84] Romanov, V.A. Anal. Ego. Prilo. **7**, (1973) 62–73.

[85] Sankaran R. Sokolov, M. Antonia, R.A. Susbtructures in a turbulent spot J. Fluid Mech. **197** (1988) 389–414.

[86] Sankaran, R. Antonia, R.A. Bisset, D.K. Sokolov, M. Flow patterns and organization within a turbulent spot. Phys. Fluids A **3** 6 (1991) 1560–1571.

[87] Satijn M.P, van Buren M.G, Clercx H.J.H, van Heijst G.J.F Vortex models based on similarity solutions of the two-dimensional diffusion equation. Phys Fluids (2004) **16** 3997–4011.

[88] Schmid, P. Henningson, D.S. *Stability and transition in shear flows* (Springer, 2001).

[89] Schmiegel A. and Eckhardt B. Fractal Stability Border in Plane Couette Flow. Phys. Rev. Lett. **79** (1997). 5250–5253.

[90] Schoppa W. and Hussain F., Coherent structure generation in near-wall turbulence. J. Fluid Mech. **453** (2002) 57–108.

[91] Schumacher J. and Eckhardt B. Evolution of turbulent spots in a parallel shear flow Physical Review E **63** (2001) 4.

[92] Schröder A. and Kompenhans J. Investigation of a turbulent spot using multi-plane stereo particle image velocimetry. Experiments in Fluids **36** (2004) 82–90.

[93] Siggia, E.D, Zippelius, A. Pattern Selection in Rayleigh-Bénard Convection near Threshold. Phys. Rev. Lett. **47** (1981) 835–838.

[94] Singer, B.A. Characteristics of a young turbulent spot. Phys. Fluids **8** 2 (1996) 509–521.

[95] Smith T.R., Moehlis J., Holmes P., Low-dimensional models for turbulent plane Couette flow in a minimal flow unit. J. Fluid. Mech. **538**, (2005) 71–110.

[96] Smits, A. J. & Delo, C. Self-sustaining mechanisms of wall turbulence, In Coherent Structures in Complex Systems. Editors Reguera, D. Bonilla, L.L. Rubi, J.M. (2001) Springer.

[97] Swift, J. Hohenberg, P.C. Hydrodynamic fluctuations at the convective instability. Phys. Rev. A **15** (1977) 319–328.

[98] Tillmark, N. Alfredsson, P.H. Experiments on transition in plane Couette flow. J. Fluid Mech. **235** (1992) 89–102.

[99] Tillmark, N. On the spreading mechanisms of a turbulent spot in plane Couette flow. Europhysics letters **32** (1995) 481–485.

[100] Trefethen L.N, Trefethen A.E, Reddy S.C, Driscoll T.A. Hydrodynamic stability without eigenvalues. Science **261** (1993) 578.

[101] Tsukahara, T. Kawamura, H. Shingai, K. DNS of turbulent Couette flow with emphasis on the large-scale structure in the core region. J. of Turbulence **7** (19) (2006) 1–16.

[102] Waleffe F, Kim J. How streamwise rolls and streaks selfsustain in a shear flow: part 2, AIAA 98-2997, (1998) *http://www.math.wisc.edu/ waleffe*

[103] Waleffe F. On a self-sustaining process in shear flows. Phys Fluids (1997) **9** 883–900.

[104] White F.M. *Viscous Fluid Flow* McGrawHill, New York (1974).

[105] Van Saarloos. Front propagation into unstable states, Physics Reports, **386** (2003) 29-222. *http://www.lorentz.leidenuniv.nl/ saarloos/*.

Appendix A

The symmetries of the model

When a system is invariant under the action of a group of symmetries which are spatial (e.g. reflections, translations, rotations), we may derive many consequences on the evolution of particular initial conditions. For the plane Couette flow, there are 3 symmetries. The first one is a reflection about the spanwise axis z. The second one is a reflection about the streamwise axis x and the last one is a central symmetry about the point $x = z = 0$. The translation is non important. The basic profile is $U(y) = U_{\mathrm{b}}y$ and we have the equations:

$$\partial_t u + u\partial_x u + v\partial_y u + w\partial_z u = \tag{A.1}$$

$$-\partial_x P - U\partial_x u - v\partial_y U + \frac{1}{R}\Delta u. \tag{A.2}$$

$$\partial_t v + u\partial_x v + v\partial_y v + w\partial_z v = \tag{A.3}$$

$$-\partial_y P - U\partial_x v + \frac{1}{R}\Delta v. \tag{A.4}$$

$$\partial_t w + u\partial_x w + v\partial_y w + w\partial_z w = \tag{A.5}$$

$$-\partial_z P - U\partial_x w + \frac{1}{R}\Delta w. \tag{A.6}$$

$$\partial_x u + \partial_y v + \partial_z w = 0. \tag{A.7}$$

Those equations are invariant under the following transformations:

$$\begin{aligned}
\mathcal{TZ}: &\quad (x, y, z) \to (x, y, -z) \\
&\quad \text{and } w \to -w, (u, v, p) \to (+u, +v, +p). \\
\mathcal{TX}: &\quad (x, y, z) \to (-x, -y, z) \\
&\quad \text{and } (u, v) \to (-u, -v), (w, p) \to (+w, +p).
\end{aligned}$$

and

$$\mathcal{TR} = \mathcal{TX} \circ \mathcal{TZ}.$$

Each transformation corresponds to a physical symmetry: $\mathcal{TX}$ is a reflection about the spanwise axis z, $\mathcal{TZ}$ is a reflection about the spanwise axis x and $\mathcal{TR}$ is a central symmetry about the point $x = z = 0$.

Since we have those expansions for the velocity components:

$$u = U_{\mathrm{b}} y + BU_0(1-y^2) + U_1 Cy(1-y^2),$$

$$v = V_1 A(1-y^2)^2,$$

$$w = BW_0(1-y^2) + W_1 Cy(1-y^2)$$

and those relation between the velocities and the fields:

$$U_0 = -\partial_z \Psi_0, \qquad W_0 = \partial_x \Psi_0$$

$$U_1 = \partial_x \Phi_1 - \partial_z \Psi_1, \quad W_1 = \partial_z \Phi_1 + \partial_x \Psi_1, \quad \beta V_1 = \Delta_2 \Phi_1$$

the three transformations can be written:

$$\begin{aligned}
\mathcal{TZ} : (x,z) \to (x,-z) \text{ and } &: \\
\Psi_0 \to -\Psi_0, & \\
\Psi_1 \to -\Psi_1\ , \quad \Phi_1 \to \Phi_1, & \\
U_0 \to U_0\ , \quad W_0 \to -W_0, & \\
U_1 \to U_1\ , \quad W_1 \to -W_1, \quad V_1 \to V_1, & \\
\mathcal{TX} : (x,z) \to (-x,z) \text{ and } &: \\
\Psi_0 \to -\Psi_0, & \\
\Psi_1 \to \Psi_1\ , \quad \Phi_1 \to -\Phi_1, & \\
U_0 \to -U_0\ , \quad W_0 \to W_0, & \\
U_1 \to U_1\ , \quad W_1 \to -W_1, \quad V_1 \to -V_1, & \\
\mathcal{TR} = \mathcal{TX} \circ \mathcal{TZ} : (x,z) \to (-x,-z) \text{ and } &: \\
\Psi_0 \to \Psi_0, & \\
\Psi_1 \to -\Psi_1\ , \quad \Phi_1 \to -\Phi_1, & \\
U_0 \to -U_0\ , \quad W_0 \to -W_0, & \\
U_1 \to U_1\ , \quad W_1 \to W_1, \quad V_1 \to -V_1, &
\end{aligned}$$